UNITED STATES DEPARTMENT OF AGRICULTURE

Agricultural Research Service

National Sedimentation Laboratory
Channel and Watershed Processes Research Unit
Oxford, Mississippi

Flow and bedform dynamics of a bimodal sand-gravel mixture

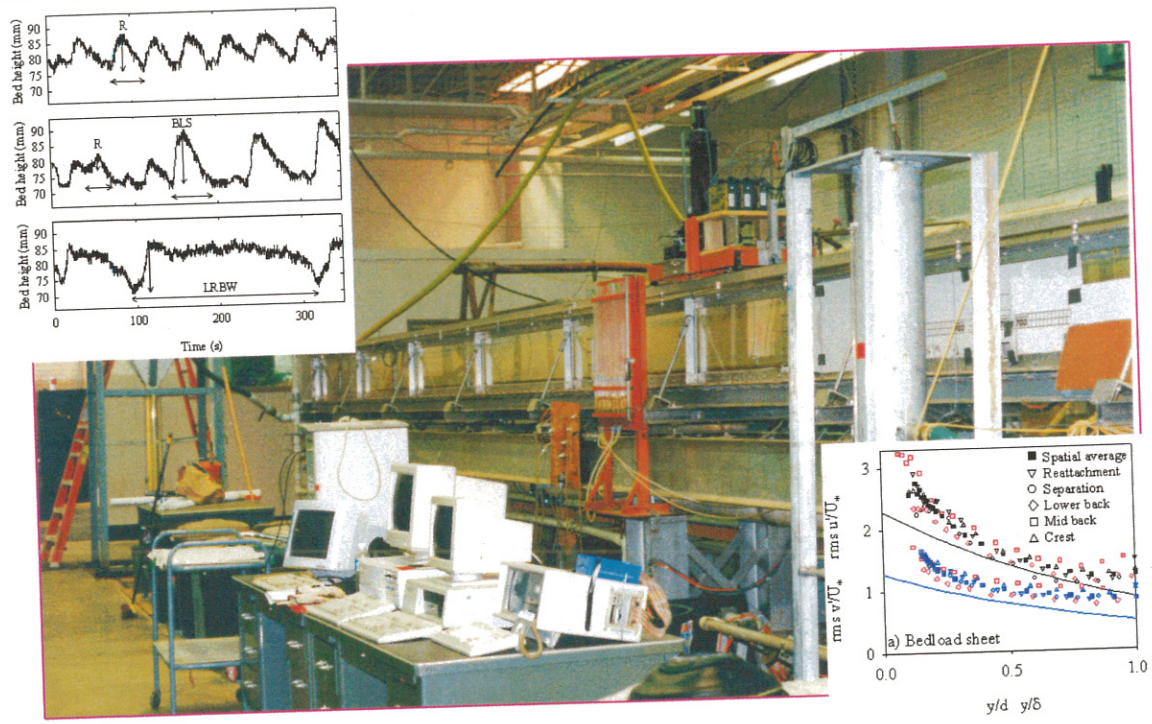

by Joanne K. Horton, Sean J. Bennett, James L. Best
& Roger A. Kuhnle

Research Report No. 32

September 2002

Acknowledgements

This report represents the completed Ph.D. thesis of Joanne K. Horton, submitted to the school of Earth Sciences, University of Leeds. Here it is reproduced verbatim.

The completion of this study was made possible by the award of NERC Case Grant GT04/97/131/FS. The help and support of academics, friends and family has enabled me to complete nearly four years of challenging, but enjoyable, research, culminating in the production of this thesis. Unfortunately it is not possible to mention all those who have assisted me here.

My laboratory flume experiments would not have been possible without the advice and actions of John Cox and Paul Seay at the National Sedimentation Laboratory, Oxford, Mississippi. Indeed, I am very grateful to all those at the Sedlab who added some light relief from the experimental regime! In particular I would like to thank Anna Curini, Andrea Curini, Daniel Wren, Vince Campbell and Paul Comper.

The analysis of my data at the University of Leeds was greatly assisted by discussions with various people within the School of Earth Science, especially Jurgen Neuberg, Nick Teanby and Michael Bourne. Very welcome interruption from my bedforms was provided by all in the Seddie group, in particular Clare Buckee, Mark Franklin, Clare Davies and Rufus Brunt. I would also like to thank David Deakin, Jane Deakin, Shanta Seereeram, David Moreton, Jenny Underwood, Stefan Fritz, Sue Adair, Tom Manson and many others for various distractions.

Special thanks go to my supervisors Sean Bennett, Jim Best and Roger Kuhnle for their ideas, encouragement and constructive comments on my work. My family have provided the greatest source of support and motivation, for which I am extremely grateful.

Contents

List of plates

u_R^2	Reference velocity at one bedform height above the crest
θ_i	Mobility parameter of size class i
θ_{cr}	Critical mobility parameter
ξ_i	Correction factor of class size i
B	Bimodality parameter
c	Bedform migration rate; speed of sound
C	Intercept of the velocity distribution
C_D	Drag coefficient
c_m	Concentration of each grain size fraction by volume
d	Flow depth
D_c	Modal grain size of coarse mode
D_f	Modal grain size of fine modal
D_x	Representative grain size, where X % of grains in the mixture are equal or finer in diameter e.g. D_{16}, D_{50} and D_{84}.
f	Darcy-Weisbach friction factor
f'	Grain roughness
f''	Form roughness
F_1	Sediment fraction in primary mode
F_2	Sediment fraction in secondary mode
F_c	Sediment fraction in coarse mode
f_D	Doppler shift
f_d	Frequency of turbulence structures produced by dunes
F_f	Sediment fraction in fine mode
f_i	Frequency of incident light
Fr	Froude number
f_s	Frequency of scattered light; Strouhal law frequency
f_v	Frequency of vortex shedding
f_w	Frequency of wake flapping
g	Acceleration due to gravity
h	Bedform height
H	Threshold value
k_s	Equivalent sand roughness
l	Mixing length; bedform length
n	Number of observations

List of Acronyms

SR	Sand ribbon
R	Ripple
BLS	Bedload sheet
LRBW	Low-relief bed wave
LDA	Laser Doppler anemometry
ADV	Acoustic Doppler velocimetry
Q1	Quadrant one
Q1%	Percentage occurrence of quadrant one events
Q2	Quadrant two
Q2%	Percentage occurrence of quadrant two events
Q3	Quadrant three
Q3%	Percentage occurrence of quadrant three events
Q4	Quadrant four
Q4%	Percentage occurrence of quadrant four events
SA	Spatial average
1	Series 1 ($d = 0.18$ m)
2	Series 2 ($d = 0.14$ m)

Table 1.1: *Factors controlling sediment transport, morphology and hydraulics within a fluvial channel.*

Components of the fluvial system	Controlling factors
1) Catchment (Influences other components of the fluvial system, but vary over temporal and spatial scales greater than those considered in the present study)	Climate Base level Geology Vegetation Land use Basin physiography Human intervention
2) Sediment transport	Grain size distribution Grain hiding and protrusion (Fractional) transport rates Transport mechanism: bedload and suspension Grain sorting: longitudinal and vertical
3) Hydraulic	Discharge Slope Depth Flow resistance Turbulence characteristics
4) Bed morphology	Development and migration of bedforms Superimposition and coexistence of difference bedforms Development of barforms (length scales with channel width) Channel form

High instantaneous near-bed forces, due to the occurrence of turbulent flow structures, can cause the initiation of sediment transport over a deformable boundary (Drake *et al.*, 1988; Best, 1992, 1993). The movement of sediment over a mobile boundary enables grains to interact, and bed pertubations to be developed (Williams and Kemp, 1971; Southard and Dingler, 1971; Raudkivi and Witte, 1990; Best, 1992; Mazumder, 2000), which feed back to modify the spatial distribution of boundary shear stress (force exerted on the bed per unit bed area) and in turn sediment transport. Defects in the sediment bed a few grain diameters high may also give rise to flow separation and the shedding of turbulent eddies (Leeder, 1980; Bennett and Best, 1996), which drive sediment erosion and deposition, therefore influencing the morphology and spacing of features propagated downstream (McLean *et al.*, 1994; Werner and Kocurek, 1999). Bedforms scale either with flow depth or are smaller forms, whereas barforms scale with channel width. The development of bedforms enables the channel to adjust vertically (i.e. form roughness), which in conjunction with grain roughness and the quality and calibre of sediment in transport (bedload and suspended load) modifies the turbulent flow (Millar, 1999; Carbonneau and Bergeron, 2000). Spatio-temporal variations in sediment transport rates result from the migration of bedforms, even when equilibrium flow conditions prevail (Iseya and Ikeda, 1987; Kuhnle and Southard, 1988).

Until fairly recently, research concerning bedforms has focused on sand sized sediment, although detailed studies have been conducted on gravel (Brayshaw, 1984; Dinehart, 1989, 1999; Buffin-Bélanger and Roy, 1998; Carling, 1999; Lawless and Robert, 2001) and mixed sand-gravel sediment (Chiew, 1991; Wilcock,

Figure 1.2: *A bimodal sediment distribution from the West Solent, UK, with characteristic peaks in the sand and gravel size ranges. From Williams (1990).*

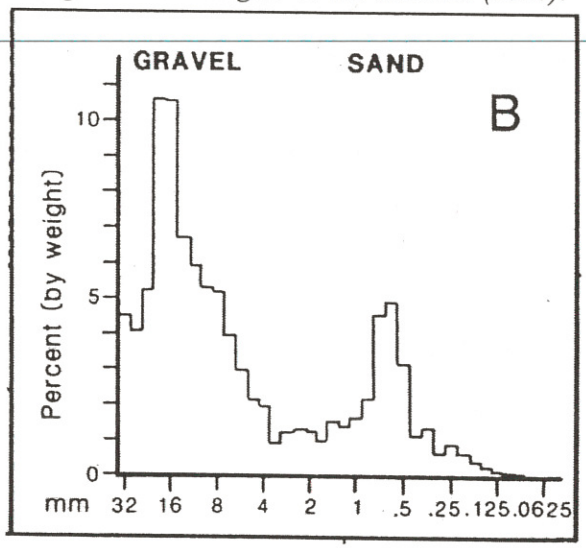

The infiltration of fines in bimodal sediments has been studied with reference to both the surface and subsurface (Carling and Reader, 1982; Diplas and Parker, 1992a), while research concerning sediment entrainment and sorting focuses on the bed surface (Iseya and Ikeda, 1987; Drake *et al.*, 1988; Kuhnle and Southard, 1988; Whiting *et al.*, 1988; Wilcock and Southard, 1988; Dietrich *et al.*, 1989; Ferguson *et al.*, 1989; Wathen *et al.*, 1995; Sambrook Smith and Ferguson, 1996; Livesey, 1998), although bedform migration can cause vertical grain size segregation (Bennett and Bridge, 1995; Khadkikar, 1999).

Due to the duel peaks in the grain size distribution of a bimodal mixture, the commonly used classification for an unimodal sediment, the mean grain size (D_{50}; 50 % of clasts are an equal or finer in diameter), is essentially meaningless since that particular grain size may be present only in minimal quantities (i.e. it falls in between the two modes; Kuhnle, 1996). Furthermore, if the sediment is strongly bimodal, the D_{50} value may shift between modes for sediment samples with only small variations in grain size distribution. Fredlund *et al.* (2000) present equations which describe the grain size distribution of unimodal and bimodal soils, aiding their identification and categorisation. However, it is useful to be able to assign a characteristic value to a sediment mixture, and therefore attempts have been made to define the degree of bimodality (Table 1.2), which can significantly influence the mechanics of sediment transport (Kuhnle, 1993a). In order to define bimodality it is important to consider: 1) the separation of the two modes, 2) the fraction of sediment contained in the modal grain sizes, 3) the relative magnitude of the modes (considering just the sediment fraction contained in the modal grain sizes) and 4) the total amount of sediment in each mode. The equation presented by Wilcock (1993, Table 1.2) does not account for the latter two factors, while the formula of Sambrook Smith *et al.* (1997, Table 1.2) omits consideration of the total quantity of sediment in each mode in order to simplify calculation of the bimodality index. Consequently, there is a possibility of a sediment mixture being wrongly classified, and therefore it is also important to visually inspect any grain size

sediment up to 0.7 mm in diameter (Costello and Southard, 1980; Leeder, 1980), since larger grains protrude above the viscous sub-layer and destroy the hydraulically smooth flow conditions required for ripple formation. The development of ripples from an initially flat bed occurs progressively (Southard and Dingler, 1971; Williams and Kemp, 1971), rather than spontaneously (Bagnold, 1956). The initiation of ripples may occur through the accumulation of mobile sediment by: 1) fast upstream particles sheltering downstream grains, leading to grouping (e.g. kinematic waves; Costello and Southard, 1980), 2) intermittent turbulent coherent flow structures eroding excess sediment for the flow capacity causing deposition (Williams and Kemp, 1971; Grass, 1983; Drake *et al.*, 1988; Best, 1992), and 3) the presence of non-uniform sediment. Best (1992) indicates that the movement of relatively high velocity fluid towards the bed occurs by multiple intermittent 'sweep' events, which are capable of eroding a larger area of the bed than a single sweep event. Furthermore, the sweep impacts result in the deposition of flow parallel ridges which focus subsequent sweep events, and associated sediment erosion, in-between the ridges. Once a defect attains a threshold height (2-3 grain diameters in sand; Best, 1992), flow separation and associated reattachment can drive the initiation of further defects and the growth and migration of the existing bedforms (Williams and Kemp, 1971, 1972; Gyr and Schmid, 1989). Liu (1957) suggested that ripples develop due to an instability at the sediment-fluid interface, and not by irregularities in the sediment bed or coherent turbulent structures. However, the observed amplification and downstream propagation of ripples cannot be accounted for by the instability mechanism (Gyr and Müller, 1996).

Figure 1.3: *Plot of bedform height against wavelength for ripples and dunes, which are separated by a gap at a wavelength of approximately 0.8 m. From Ashley (1990).*

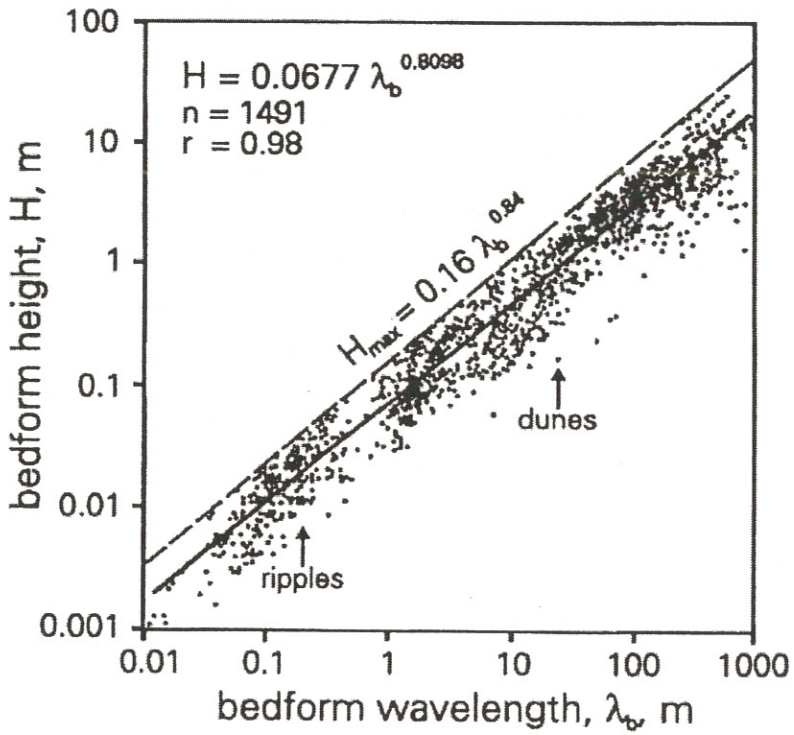

Figure 1.4: *Schematic model of changing flow and turbulence structure across the ripple-dune transition.*

a) Rippled bed, equilibrium flow
b) Rippled bed, non-equilibrium flow (increasing transport stage). Formation of a larger than average bedform ('rogue' ripple).
c) Dune bed, equilibrium flow

τ / τ_o : Approximate ratio of the time-averaged Reynolds stress (force exerted by the fluid) near reattachment to the spatially-averaged boundary Reynolds stress over the entire bedform
Q_2: Quadrant 2 (ejection) events – slow, upwards moving fluid structures
Q_4: Quadrant 4 (sweep) events – fast, downwards moving fluid structures
d: Flow depth
h: Bedform height

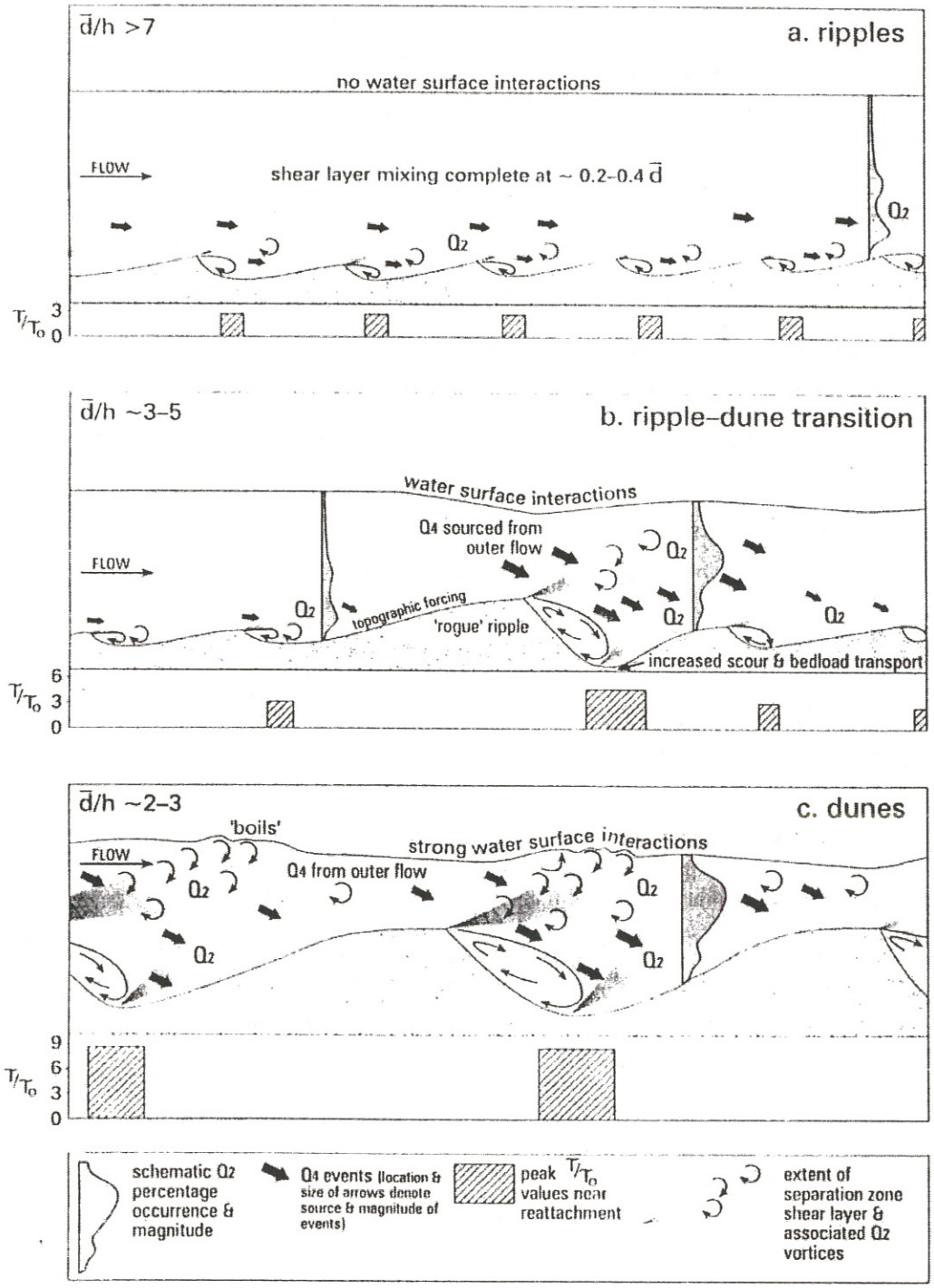

Ferguson, 1989; Kirchner *et al.*, 1990; Dinehart, 1992a, b; Kuhnle, 1993a, b; Wilcock, 1998). However, Bennett and Bridge (1995a) note that comparison with other studies is hindered by incomplete morphological and hydraulic data. Due to past technical difficulties of recirculating gravel sized sediment in a laboratory flume, there is currently a limited knowledge concerning the morphology and textural characteristics of bedforms generated in sand-gravel mixtures and their associated turbulent flow structure. Furthermore, direct observations and measurements of bedload motion in coarse-grained sediments are problematic, and therefore the dynamics of small-scale bedforms remains unclear. A range of flow-transverse bedforms have been previously identified in mixed sized sediment mixtures (Table 1.3). Longitudinal bedforms have also been observed in sand-gravel mixtures (i.e. sand ribbons; McLean, 1981; Nezu and Nakagawa, 1993; Livesey, 1995; Tsujimoto and Kitamura, 1996), which give rise to lateral variations in boundary roughness.

Table 1.3: *Flow transverse bedforms developed in sand-gravel mixtures. θ represents the dimensionless bed shear stress.*

Bedform	Height (mm)	Length (mm)	Migration rate (mm/s)	θ	Texture	References
Ripples	3-40	30-800	4-34	0.09	Sand fractions	1
Particle clusters	D_{95}	100-1200	Move by breaking up.	0.009	Coarse stoss, fine wake	2
Bedload sheets	4-13	70-1200	1-27	0.04-0.12	Coarse trough, fine stoss coarsens towards crest.	3
Low-relief bed waves	8-17	1700-4850	0.3-14	0.04-0.24	Coarse trough, fine stoss coarsens towards crest.	4
Dunes	100-100000	600-100000	30	0.1-0.3	Fine stoss coarsens towards crest. Coarse trough when sediment transport low.	5
Antidunes	10-1000	50-19000	Direction variable. Rate influenced by steepness.	0.2-2.5	Coarest clasts on or near the crest, few on the lee.	6
Transverse ribs	1-2 clast diameters	50-1250 (width) 200-2500 (wave-length)	Direction variable.	0.2-2.5	Coarse clasts, with fine infill and backfill.	7

1 Yalin (1992); Wilcock and McArdell (1993).

2 Dal Cin (1968); Brayshaw (1984); Naden and Brayshaw, 1987; Hassan and Reid, 1990; de Jong (1991); Reid and Hassan (1992).

3 Ikeda and Iseya (1988); Whiting *et al.* (1988); Dietrich *et al.* (1989); Bennett and Bridge (1995a, b).

4 Bennett and Bridge (1995a); Livesey *et al.* (1998).

5 Hubbell *et al.* (1987); Kuhnle and Southard (1988); Carling (1999); Dinehart (1999).

6 Kennedy (1963); Shaw and Kellerhals (1977); Whittaker and Jaeggi (1982); Mehrotra (1983); Yagishita and Taira (1994); Alexander and Fielding (1997).

7 Koster (1978); McDonald and Day (1978); Rust and Gostin (1981); Allen (1983); Bluck (1987).

1.3.2.1 Pebble clusters

Increases in sediment calibre cause a corresponding expansion in the role of grain roughness and protrusion upon the flow. Cluster bedforms typically form around an exceptionally large obstacle clast (Plate 1.1; Dal Cin, 1968; Laronne and Carson, 1976; Brayshaw, 1984; Buffin-Bélanger and Roy, 1998). The other constituent particles are arranged so that the long axis of the pebble cluster is parallel to the flow, with relatively coarse grains in front of the main clast (stoss deposit), and finer sediment being deposited behind

obstacle grain, the size of the lift and drag forces it experiences will depend upon the obstacle and mobile particle's relative position and size (Table 1.4 and Figure 1.5). Measurement of the forces acting on bed particles has been hindered by technical problems and the complex 3-dimensional shape of the clusters.

Table 1.4: *Variations of the lift and drag forces. From Brayshaw et al. (1983).*

	Lift force	**Drag force**
In the wake of an obstructing particle (much reduced lift and drag forces than if exposed singly in the freestream)	Varies in direct proportion to particle separation. The distance over which an obstacle grain provides protection depends on size relations. At greater separations lift force still rises in response to an exaggerated imbalance in pressure due to exposure of upper surface to accelerated flow while base remains in low velocity of the obstacle's lee.	Varies in direct proportion to particle separation. The relative size of the obstacle and mobile grains determines the direction of drag in the immediate lee of the obstacle. Inverse relationship between the ratio of movable to obstacle grain size and the downstream extent of the obstacle's sphere of influence over bed particles in its train.
Stoss side of the cluster	Increases gradually when particle separation is small (below about 0.3 times the obstacle diameter) and reduced, arising from acceleration of flow around the flanks. Particles of like size, closely spaced, act as a single entity. Low pressure develops across the flow separation plane that encloses the diminishing gap between the particles, producing extra lift on the leeside of the leading particle, reducing its stability.	Uniform regardless of particle separation.

This mutual interference of adjacent particles has received little attention, and yet it is vital when considering incipient motion, which is delayed by the presence of clusters (Reid *et al.*, 1984; Hoey, 1992). In addition, clusters limit the availability of bed sediment for transportation. The complex and variable pattern of cluster bedforms partially accounts for the wide range in critical shear stresses for particles of similar size and shape (Brayshaw *et al.*, 1983). Pebble clusters are therefore a major component of sedimentary sorting, encouraging deposition of a wide range of particle sizes. Brayshaw (1984) observes that obstacle clasts reflect the largest grain size exhibited by the bed (D_{95}). Fine sediment, similar to that found in the sub-surface layer, is associated with the wake region (D_8 to D_{46}), while the stoss area is characterised by coarser grains (D_{74} to D_{94}). The surficial nature of clusters can be seen in cut sections, with the wake deposits observed to fine downwards. In natural clusters the stoss side deposit has a higher relief compared with the wake regio

After the deposition of the obstacle clast at a relatively high flow level, downstream accumulation of fines begins (Dal Cin, 1968; Brayshaw, 1984). Only finer sediment is influenced by recirculating flow in the lee side, and therefore transported into the wake area, since the larger particles have too great a momentum. Minor scour may appear at the upstream edge of the obstacle clast, but deposition here only occurs at lower flow velocities since grains are carried around the main clast by local flow acceleration at higher flow speeds. Therefore a temporal difference between the accumulation of wake and stoss deposits exists, and the geometry of the cluster is influenced by the size of the obstacle clast. Higher velocities may actually increase the stability of the bedform, with stoss deposits being more firmly pushed against the main clast, and wake sediment accumulations being contained in the low pressure flow separation region. Mutual particle interference and interlocking cause the critical entrainment threshold of the clasts to be greater when they are part of a cluster than when they exist in isolation (Reid *et al.*, 1984). Teissyre (1977) contends that cluster development requires the same hydrodynamic conditions as imbrication i.e. turbulent, rapid flow conditions. Brayshaw (1984) suggests that clusters develop during the recession limb of a flood in which bedload movement occurred, and are therefore not equilibrium bedforms. Subsequent remobilisation of the constituent sediment occurs suddenly by flows which are competent to dislodge the obstacle clast (i.e. rising stage of a flood), leading to variations in the bedload transport rate. However, de Jong (1991) concluded from fieldwork observations that clusters are a relatively immobile component of the bed, and therefore are not as significant as previously thought in delaying sediment entrainment. Furthermore, the entrainment of sediment from a cluster does not require the main clast to be removed, facilitating the rebuilding of clusters. Typically stoss deposits are released in preference to grains which accumulate in the lee region (Brayshaw *et al.*, 1983; de Jong, 1991). de Jong (1991) observed clusters to be destroyed radially from the obstacle clast, with sediment being entrained laterally and occasional upstream. The arrangement of the grains in the cluster influences which particles are prone to entrainment (de Jong, 1991; James, 1993). In order to explain the selective entrainment of cluster particles, de Jong (1991) invokes the idea of local instantaneous flow conditions, not necessarily the flood flows envisaged by Brayshaw (1984).

Large individual particles can induce two main flow vortex systems (Figure 1.6; Acarlar and Smith, 1987a), whilst the occurrence of clusters is associated with the development of complex three-dimensional flow structures (Figure 1.7; Kirkbride, 1993; Robert *et al.*, 1996; Lawless and Robert, 2001). Six regions with characteristic vertical flow conditions have been observed over clusters: 1) flow acceleration on the stoss, 2) recirculation in the wake, 3) vortex shedding from the crest of the obstacle clast and shear layer, 4) flow reattachment, 5) upwelling downstream of reattachment and 6) flow recovery (Buffin-Bélanger and Roy, 1998; Lawless and Robert, 2001). Highly dynamic boundaries exist between these distinct flow regions,

***Figure 1.7**: Flow regions associated with the presence of a pebble cluster on the turbulent flow field. From Buffin-Bélanger and Roy (1998).*

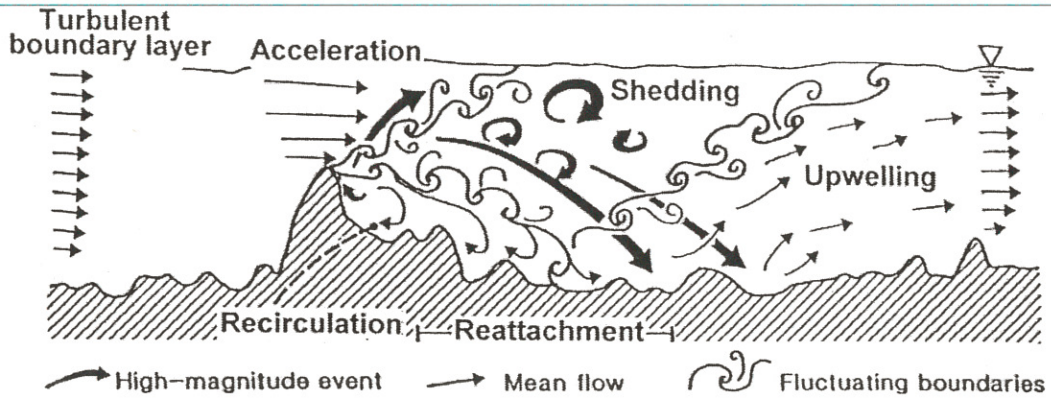

1.3.2.2 Low-relief bedforms

Bedload sheets, first defined by Whiting *et al.* (1988; Figure 1.8), represent small amplitude (only a few coarse grain diameters in height) waves of sediment. The height of bedload sheets scales with grain size (Seminara *et al.*, 1996) rather than flow depth as is the case for dunes (Allen, 1984). The wavelength of bedload sheets is more variable than that of dunes, due to the relatively small zone of flow separation/deceleration (Bennett and Bridge, 1995). The length to height ratio of low-relief bedforms is greater than 60, and flow separation is not expected for values exceeding 14 (Dyer, 1986; Kostaschuk and Church, 1993). However, Whiting *et al.* (1988) did observe indications of local flow separation associated with bedload sheets. The mechanism responsible for sheet spacing is unclear, although Whiting *et al.* (1988) propose that size selective transport, elevated bed shear stress and sediment supply may play an important role.

***Figure 1.8:** Schematic diagram of a bedload sheet observed by Whiting et al. (1988) in Duck Creek, Wyoming. Lengths varied between 0.2-2 m, with heights of 2-20 mm. Flow direction is indicated by the arrow, which represents a distance of 50 mm.*

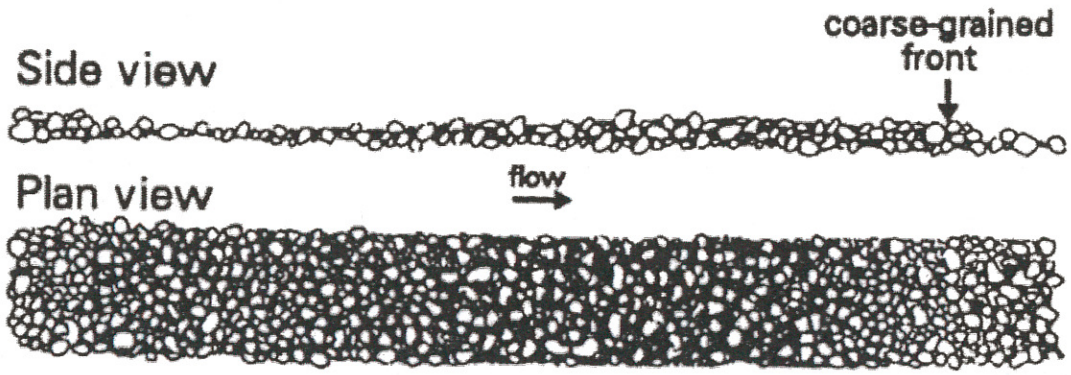

In addition to bedload sheets, asymmetric low-relief bed waves have been documented by Bennett and Bridge (1995a) and Livesey *et al.* (1998). The height of low-relief bed waves (10-17 mm) is dependent on flow depth, although it is similar to that of the bedload sheets (up to 12 mm; Bennett and Bridge, 1995).

Figure 1.9: *Temporal variations in total and fractional transport rates due to grain size sorting over the surface of migration bedforms, a) Iseya and Ikeda (1987), and b) Whiting et al. (1988).*

a)

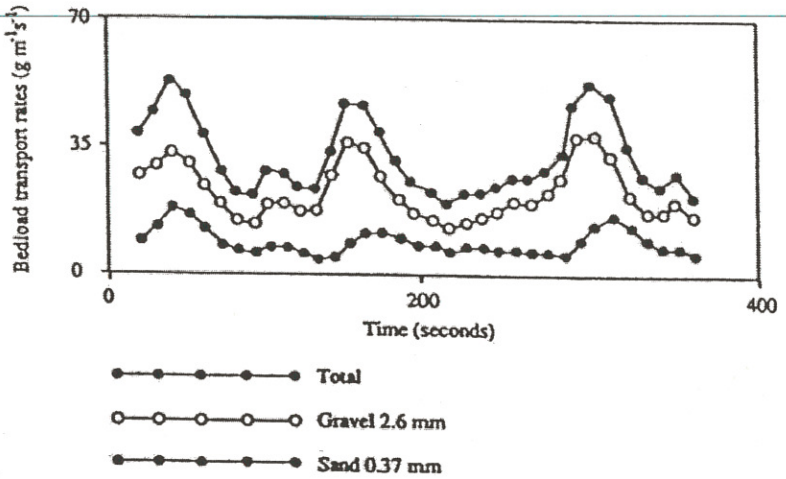

b)

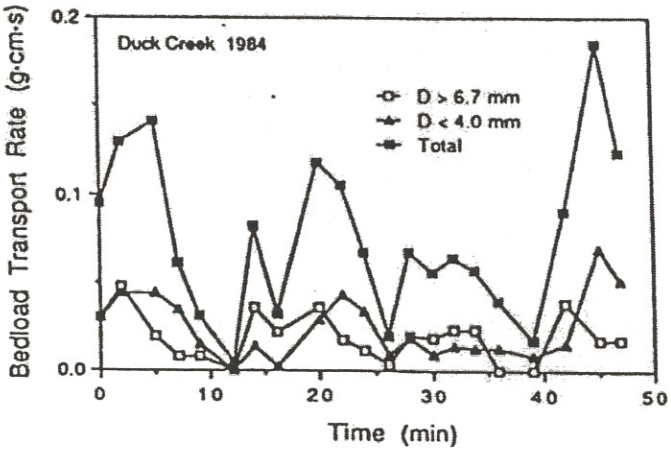

A heterogeneous sediment mixture is essential for development of bedload sheets and low-relief bed waves (Parker, 1991b; Seminara *et al.*, 1996; Tsujimoto, 1999), as exemplified by the flume experiments of Dietrich *et al.* (1989) where bedload sheets were only apparent with the addition of sand to fine gravel (Figure 1.10b). Furthermore the ratio of the different grain size fractions is important in the formation of these bedforms (Table 1.5; Iseya and Ikeda, 1987; Ikeda and Iseya, 1988). Dunes may form in preference to bedload sheets where sand dominates the sediment mixture (Kuhnle, 1996). Conversely, if there is a dearth of sand, finer size fractions will only be released once the gravel is in transport and bedload sheets will not form. It is critical to increase our understanding of the effect of bedforms on local surface sediment segregation, and the availability of different grain size fractions. Where bimodal sediments prevail it is uncertain whether or not the bedload is bimodal at all stresses, and if the mean grain size gradually increases, or abruptly switches from one mode to the other (Wathen *et al.*, 1995).

grain sizes (1.83 and 0.6 mm respectively), which may be responsible for the contrasting observations. Klassen (1992) also noted that the dune crests were composed of finer, better sorted sediment compared with the trough, influencing fractional transport rates. Snishchenko *et al.* (1989) recorded reduced heights and lengths for dunes developed in non-uniform bedload compared with those developed in uniform sediment. Moreover, Kuhnle (1993a) observed the height of bedforms to fall as the proportion of gravel in the sediment mixture increased, and Lanzoni (2000) notes that the height of bars is dampened in bimodal sediments compared with bars generated in uniform sediment. If the separation between the modes is large, the two grain size populations behave independently i.e. isolated and starved bedforms form in the finer sediment and migrated over a coarse armour layer (Wilcock, 1992).

Bennett and Bridge (1995a) observed crude planar stratification and imbrication of the largest grains within bedload sheets. Thin planar laminae (less than 5 mm thick) are composed of alternating coarse and fine layers resulting from the migration of the bedload sheet trough and crest respectively (Livesey, 1995). Dune deposits are characterised by highly evolved cross-stratification, which is not associated with bedload sheets since well-developed lee slopes at the angle-of-repose are only associated with the largest bedload sheets, and any depositional patterns maybe disrupted by the large clasts. However, poorly developed, low-angle foresets (< 20°) can occur due to the migration of bedload sheets which are superimposed on the back of low-relief bed waves and influence the supply of sediment to the crest of the bed wave (Costello and Southard, 1980; Whiting *et al.*, 1988; Raudkivi and Witte, 1990; Ditchfield and Best, 1992; Livesey, 1995).

Whiting *et al.* (1988) have proposed the 'catch and mobilise' theory regarding the formation and migration of bedload sheets. They believe that bedload sheets form due to the interactions of coarse and fine sediment during transport. Fine sediment infills the interstices of immobile coarse clasts causing the bed to be smoothed and the loss of momentum due to the collective wakes of the large particles to be decreased. Therefore any elevated, coarse grains will be subject to an increased drag force. Furthermore, infilling by fines diminishes the pivoting angles of the coarser sediment (Komar and Li, 1986). Consequently, the coarser clasts are remobilised as a result of the fine sediment infilling their interstices. However, the smoothing of the coarse grains will decrease the generation of vortices and eddy shedding, and cause the magnitude and frequency of turbulent events capable of entrainment to diminish. Furthermore, if the coarse grains are immobile, the pivoting angles will remain unchanged, but the deposition of finer material with cause the larger clasts to be smothered, further reducing their mobility. In order to explain the wave like nature of the bedload sheets, it is suggested by Whiting *et al.* (1988) that either the infilling with fine sediment is patchy, or that the coarser sediment is deposited as a cluster by particle interaction, forming a barrier to the movement of the finer material. However, the 'catch and mobilise' theory has not been backed up with quantitative data to date, and is not supported by the findings of Wilcock and McArdell (1993) and

entrainment and bed shear stress perturbations (Whiting *et al.*, 1988; Bennett and Bridge, 1995; Seminara *et al.*, 1996; Tsujimoto, 1999).

There still remains a dearth of data regarding the morphology, dynamics, bed surface sorting patterns, formation, stability, flow conditions and sediment transport of bedforms developed in bimodal sediment. Such information is vital when employing models to predict sediment transport, sorting, bedform development and stratigraphy.

1.4 Bedform stability fields

Bedforms are often classified by a mean sediment size and some function of the flow strength (e.g. stream power, shear stress and velocity), although other factors affect bedform development (e.g. flow depth, Southard and Boguchwal, 1990). Most work into the stability fields of bedforms has been undertaken in controlled laboratory flume experiments with equilibrium flow conditions, often using uniform, well-sorted sediment (Leeder, 1982; Allen, 1982; Southard and Boguchwal, 1990). Even in these simplified cases areas of overlap occur, due to different experimental arrangements and the presence of transitional bedforms. The great advantage of bedform stability diagrams (Figure 1.11) it that they can be used for both forward and reverse modelling. For example, if the flow and sediment characteristics are known the bed configuration can be predicted, and conversely the past flow conditions can be estimated from the dimensions of preserved bedforms. However, when applying bedform classifications it should be remembered that in natural streams both sediment and flow characteristics vary spatially and temporally, and there is often a lagged response and hysteresis effects. Therefore, the bedforms may not be in equilibrium with the prevailing flow conditions (Richards, 1982). Furthermore, since little data has been compiled from mixed sized sediment mixtures, sorting effects are also often not considered. In addition, the mean grain size may not be truly representative of a poorly sorted or multimodal sediment, potentially causing bedforms to be incorrectly plotted on stability diagrams. The need to construct a bedform phase diagram which accounts for more complex grain size distributions (e.g. Chiew, 1991; Figure 1.11a) is highlighted by the fact that some bedforms are not observed in uniform sediment mixtures e.g. bedload sheets (Dietrich *et al.*, 1989). Currently, the bedforms present for a given sand-gravel mixture and flow strength cannot be reliably predicted. The extrapolation of bedform phase diagrams to include greater grain sizes (Best, 1996; Figure 1.11b) is hindered by a lack of experimental data employing high flows over coarse sediment. Chiew (1991) observed that increasing the sorting of the sediment mixture caused ripple formation to occur at higher stream powers (Figure 1.11a). The increased number of less mobile coarse grains in more poorly sorted sediment mixtures inhibit flow separation over bed defects. The coarser clasts aid vertical mixing that counteracts variations in static pressure over bed defects, causing flow separation, defect amplification and ripple formation to be hindered (Leeder, 1980).

1.5 Aims and structure of thesis

Laboratory flume experiments have been conducted in order to investigate the morphology, sediment transport and associated turbulent flow structure of bedforms developed in a bimodal sand-gravel mix. Various measurements were taken under equilibrium flow conditions, over a range of shear stresses and flow depths, in order to accurately define the hydraulic and sedimentological characteristics, and highlight any correlations between variables and spatio-temporal trends. The data collected included velocity and turbulence time series (laser doppler Anemometer, LDA), water and bed surface profiles, samples of the surface texture, and total and fractional sediment transport rates. Further details of the experimental arrangement and procedure are considered in Chapter 2. The resulting data set is analysed and presented in three main sub-sets based on the type of measurement (e.g. (a) morphology and surface texture, (b) mean flow structure, and (c) turbulent flow structure), as illustrated in Figure 1.12. Measurements of sediment transport are considered at various points throughout the thesis. As highlighted by Figure 1.12, the sub-sets of data cannot be studied in isolation due to the dominant existence of feedbacks and interrelationships, which are vital in helping understanding how bedforms develop, evolve and migrate.

The analysis of the data collected enables the following hypotheses to be tested.

- Can different bedform populations be distinguished by their morphology?
- Do variations in flow discharge and depth influence bedform morphology, texture, total and fractional sediment transport rates, and mean and turbulent flow structure?
- Does large-scale flow separation occur over bedload sheets and low-relief bed waves?
- Does the turbulent flow structure, and total and fractional sediment transport rates, respond to changes in the bed roughness?
- Are bedload sheets and low-relief bed waves formed due to bedform amalgamations, spatial variations in shear stress, selective entrainment and interactions between particles?
- Do bedload sheets and low-relief bed waves exhibit a different morphology and associated turbulent flow structure to that of dunes?

Chapter 2 : Experimental apparatus and procedure

2.1 Equilibrium flow and experimental program

2.1.1 Equilibrium conditions and the test section

All measurements were taken once the flume had attained uniform flow conditions. The equilibrium status was characterised by constant and parallel water and bed surface slope over time (only locally true where bedforms are present), no erosion or deposition of sediment, and consistent bedform configuration over time in the test section (Williams, 1967). The equilibrium stage was therefore identified from successive water and bed surface profiles and observations of bedform geometry. The test section was free from entrance and exit effects, extending 2.2 m from 10 m downstream of the headbox to 1.35 m upstream of the sediment trap. All experiments were run for at least eight hours before any measurements were recorded to ensure uniform flow conditions. The frequency and time period over which observations are made depends mainly on the bedform configuration (Guy *et al.*, 1966).

2.1.2 Experimental procedure

Figure 2.1 illustrates the basic procedure employed during an experimental run.

2.1.3 Mobile bed experiments

Fourteen experimental runs were conducted employing a mobile sediment bed. Eight of these experiments were characterised by a water depth of 0.17-0.18 m (*Series 1*), while the remaining six runs exhibited a flow depth of 0.14-0.15 m (*Series 2*).

2.1.4 Fixed bed experiments

A further two experimental runs were executed over an immobile sediment bed, formed during a previous mobile sediment bed experiment (i.e. Runs F and J). The bed configuration was preserved along the whole length of the flume by carefully applying epoxy resin (Araldite resin GY6010, hardener HY955). To prevent the resin sticking to the flume, aluminium foil was inserted between the sidewalls and the sediment using a thin metal strip, causing only minor distortion to the sediment bed. Once the resin had been applied and set, the foil could then be torn to the bed level, and the small gap left by its insertion filled with plasticine.

2.2 Laboratory flume facility

The experimental runs were executed in an adjustable slope recirculating laboratory flume, with a channel 15.2 m long, 0.356 m wide and 0.457 m deep (Figure 2.2, Plate 2.1). A steel frame supported the flume, and the walls and base of the channel were constructed from perspex, enabling the water and sediment (which were recirculated separately) to be observed directly during the experiments. The experimental facility was located in the USDA-ARS National Sedimentation Laboratory in Oxford, Mississippi, USA.

Plate 2.1: *Experimental facility.*

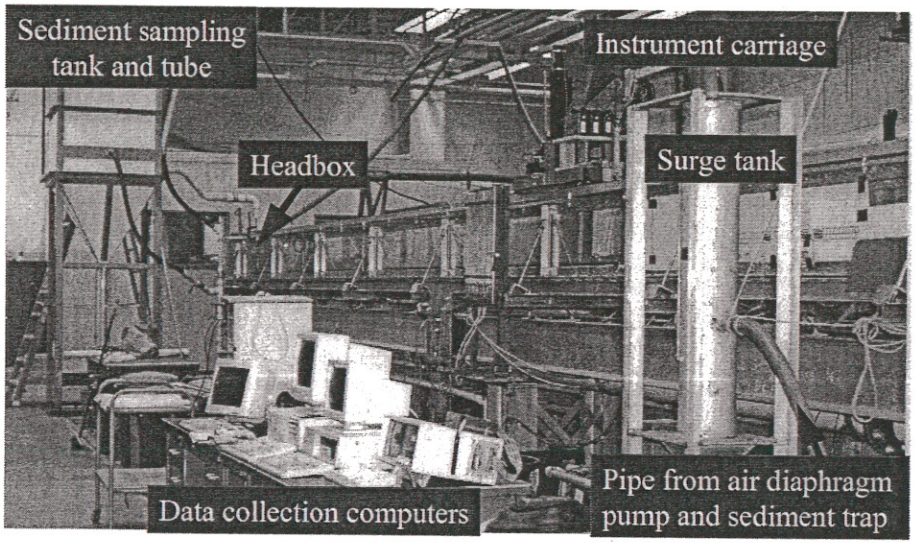

Figure 2.2: *Schematic diagram of the laboratory flume employed. 1) overflow section, 2) accumulation tube, 3) sediment sampling, 4) sediment and water recirculation, 5) headbox, 6) water supply, 7) Instrument carriage, 8) sediment retaining wall, 9) sediment trap, 10) tail box, 11) propeller pump, 12) diaphragm pump, 13) surge tank, 14) water recirculation, 15) recirculation of water and sediment, 16) Venturi meter, 17) manometer and standpipes.*

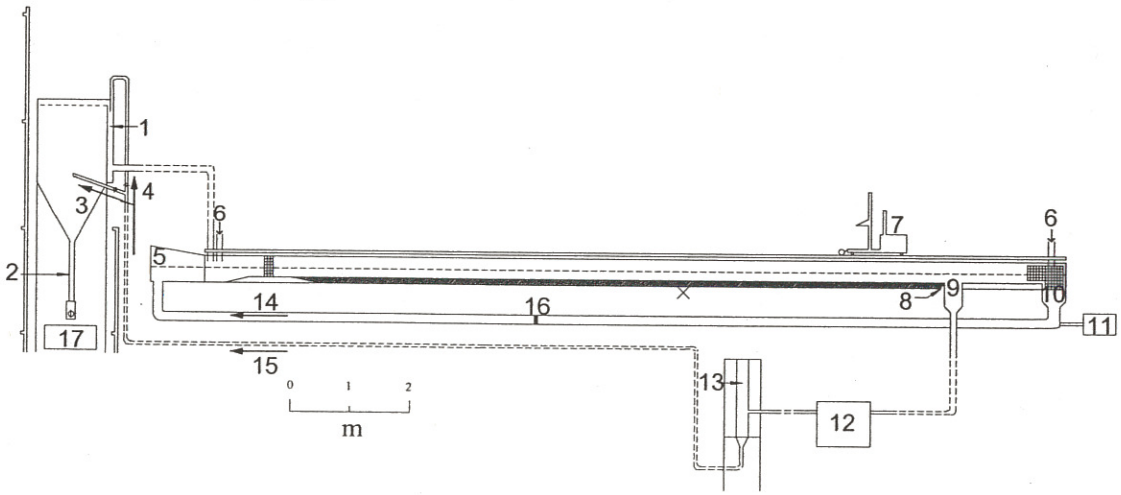

flume contained no sediment allowing the diaphagm pump to be idle. The water discharge measurement equipment was checked over a range of flow strengths and demonstrated close agreement as illustrated in Figure 2.4.

Figure 2.3: *Manometer.*

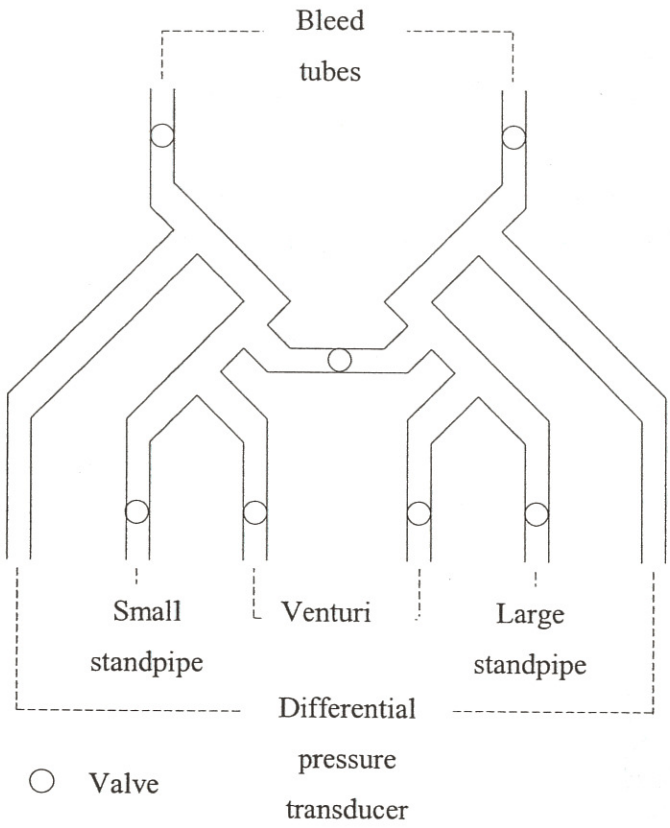

Figure 2.4: Calibration of the Venturi meter and differential pressure transducer.

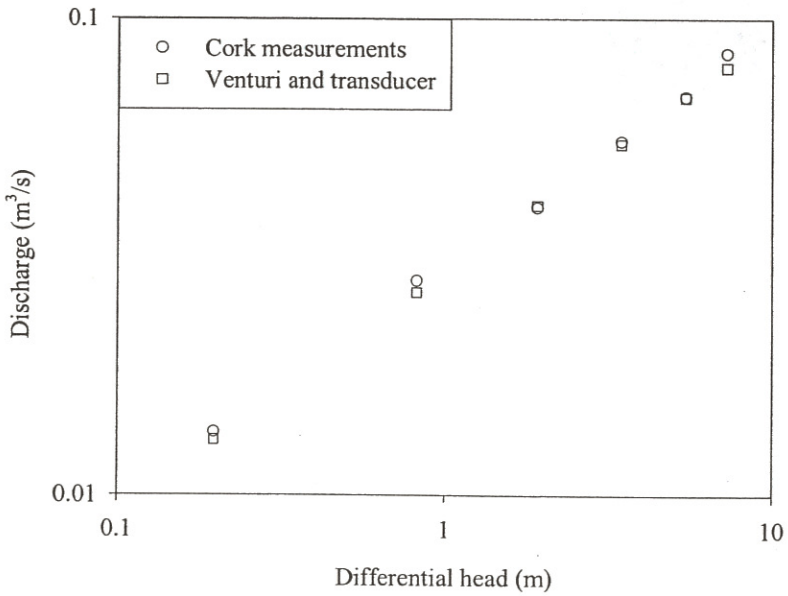

Figure 2.5: *Calibration of the air diaphragm pump (R^2 = 0.99).*

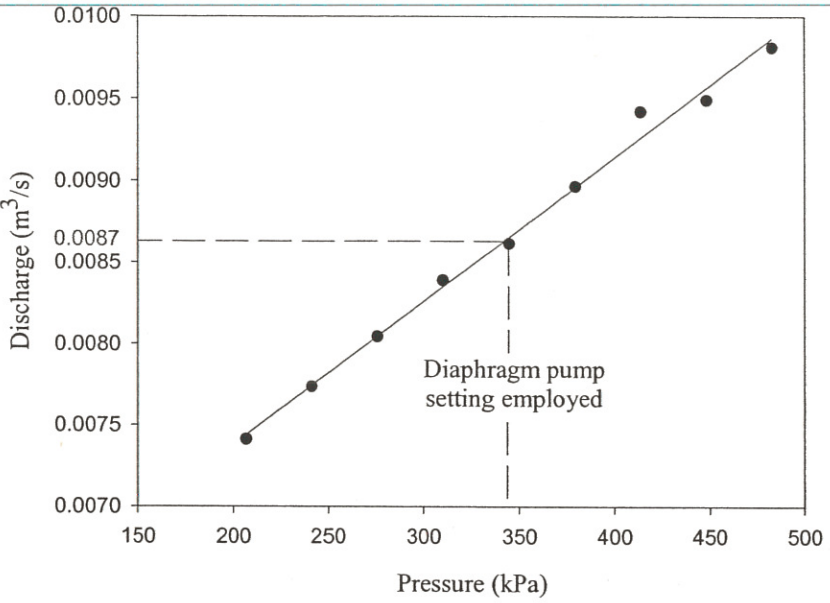

The water was not discharged from the weir back into the flume, and consequently water was continually added to the system. The water level in the flume varied, which may have slightly altered the performance of the air diaphragm pump. Changes in roughness in the recirculation system (e.g. sediment in transport, air bubbles, blockages and leaks) and variations in the discharge for each stroke of the pump, could cause the actual discharge of the air diaphragm pump to diverge slightly from the discharges predicted here.

2.3 Sediment mixture, recirculating and sampling

2.3.1 Bulk sediment mixture

In order to evaluate the grain size distribution of the bulk sediment mixture samples greater than 10 kg in weight were obtained (representative sample size equal or greater than 7.5 kg; Church *et al.*, 1987). Ten samples were taken before any runs had commenced. A further three samples were collected between runs C and K, in conjunction with clay-piston samples and photographs of the undisturbed sediment bed. Two final samples were obtained between runs F and J. As is illustrated in Table 2.1, good agreement was found between the samples. The experimental bimodal mixture has a peak in the sand (0.5 mm) and gravel (5.6 mm) sediment sizes, with grain sizes ranging from 0.177 mm to 32 mm (Figure 2.6).

thoroughly mixed together. The procedure was repeated twice for every mixing cell. Before commencing an experimental run the bed was then screed flat before water was added to the system.

2.3.2 Bedload recirculation and sampling

A sediment trap, 0.26 m long and extending across the full flume width, was located 1.2 m upstream from the flume tailbox (Plate 2.3). Complete cross-sectional coverage is necessary for accurate determination of fractional sediment transport rates (Wilcock, 1992). All of the transported sediment, with the exception of some of the suspended fines at high discharges, fell down into the sediment trap. On the upstream side of the trap was located a small retaining wall which limited the extent of the sediment slip face. The top of the wall was approximately level with the deepest bedform troughs. The upper part of the sediment trap had vertical walls, which at the bottom became inclined in order to connect to the narrower piping. An air powered diaphragm pump transported the sediment, and some water, through a 0.51 m diameter pipe. A surge tank was installed on the pipeline to smooth out the rapid pulsing movement generated by the air diaphragm pump. The pipeline fed the sediment and water mixture vertically down into the flume channel, just downstream of the headbox, via the overflow section of the accumulation tank.

Plate 2.3: *Bedload sediment trap. Flow is from bottom to top. The flume is 0.356 m wide.*

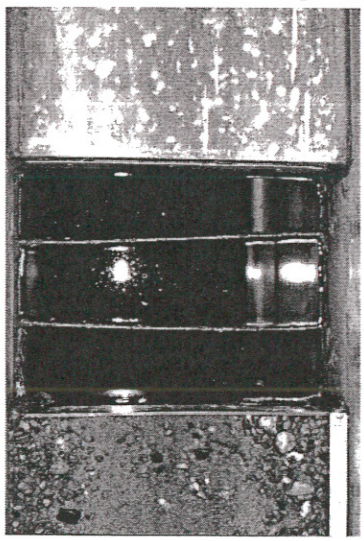

Downstream of the sediment trap the flume base was raised to the level of the mobile sediment bed. Any sediment which overpassed the trap tended to settle and migrate along this section which extended to the tailbox. The trapping efficiency of the sediment trap is determined by how much of the total sediment transport is captured, and in mixed sized sediments it also relates to the proportion of each grain size of the transported sediment collected. The efficiency of a sediment trap varies with velocity, depth, particle size, bedload magnitude, trap dimensions and bed configuration (Hubbell, 1964).

Plate 2.4: *Collection of a bedload sample from the accumulation tube.*

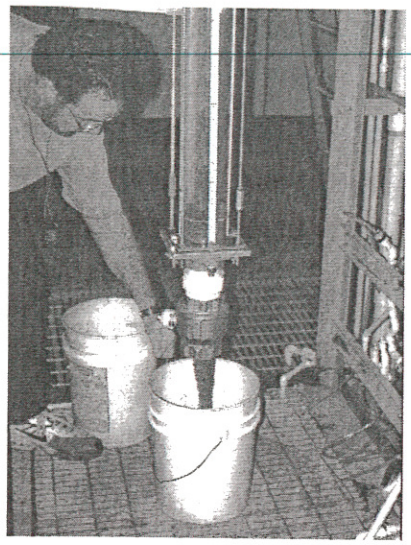

The accumulation tube was calibrated (Equation 2.1, Figure 2.7) in order that the retained sediment could be substituted by an equivalent mass of bulk sediment mix. Calibration was achieved by collecting sediment when running both pumps, and thereby causing the bed sediment to be transported, and also by tipping the bulk sediment mixture down the sediment trap with only the air diaphragm pump in operation. Both methods provided very similar results. Once a calibration sediment sample had been collected, part of the deposit was removed, dried and weighed, and the vertical adjustment of the sample in the tube recorded. Calibration was performed on six separate sediment samples. The length of time the sample is left in the tube, the specific region of a bedform being sampled and whether or not the tube is tapped, can cause the results to differ from that predicted by Equation 2.1.

$$\text{Weight of sediment (kg)} = 13.56 \times \text{height of deposit (m)} + 1.327 \qquad (2.1)$$

Bedload samples were removed from the accumulation tube, dried, sieved and weighed. Grain size analysis was performed at 1/4 ϕ intervals, where $\phi = -\log_2 D$ (mm), using sieves and associated shakers. Errors in the measurement of the size distribution can arise from grains passing diagonally through the square sieve openings, and by analysing samples which are too small to be representative. A larger sample is required as grain size increases. Where the largest clast represents 0.5 percent by weight of the total sample, this corresponds to a representative sample size of 7.5 kg for the bulk mixture used in the present experiments (Church *et al.*, 1987). All the bedload samples were typically significantly greater in weight than 7.5 kg with the exception of runs A, B and I (0.638, 2.583 and 7.030 kg respectively). However, these runs were characterised by the lowest water and sediment discharges, and the associated bedload was deficient in the coarser particles, which require a larger sample size to be adequately represented.

The bedload sample collection period varied from 60 to 1500 s depending on the sediment transport rate. Ideally a whole number of bedforms were collected. During experimental runs characterised by high rates of sediment transport, more than one bedload sample was taken (Table 2.2).

Table 2.2: *Bedload samples*

Run	Collection period (s)
A	1200
B	1200
C	840
D	580
E1	347
E2	373
F	295
G1	213
G2	190
H1	177
H2	145
H3	405
I	1500
J	561
K	522
L1	260
L2	416
M1	81
M2	133
M3	196
N1	80
N2	70
N3	60

2.3.3 Suspended sediment sampling

The suspended sediment load was sampled by a tube (0.01 m diameter) which protruded to the middle of the return pipe, and was situated just upstream of the propeller pump. At this point any particles which overpassed the sediment trap were assumed to be uniformly suspended throughout the return pipe due to the turbulence generated by the pump. The sample tube was first purged before six 20 s samples of water and sediment (about 3 litres each) were siphoned off into tarred buckets during an experimental run. Water was added to the flume in order to replace that removed. The sample buckets and contents were then weighed,

Figure 2.8 illustrates how the distance between the ultrasonic probe head and the surface to be measured is recorded. The distance, d, is calculated by multiplying the speed of sound in water, c, by half the time it takes for the ultrasonic pulse to be transmitted, reflected and returned, t (Equation 2.2).

$$d = \frac{tc}{2} \tag{2.2}$$

In order to correctly correlate pulses and echoes, the transmission of each pulse must be separated by a time interval greater than t. The system is controlled and timed by the data collection computer. It is vital for c to be constantly monitored as it is influenced by the temperature of the transmitting fluid. Consequently, the NCPA probes include a circuit for measuring water temperature and adjusting the distance calculation accordingly. The Contaq probe system accounts for variations in c by simultaneously using two probes, one of which measures a known, fixed distance. The latter probe is therefore used to calibrate the data collected by the main measurement probe. Data was transferred to another computer for storage and processing.

Figure 2.8: *Distance measurement with ultrasonic probes.*

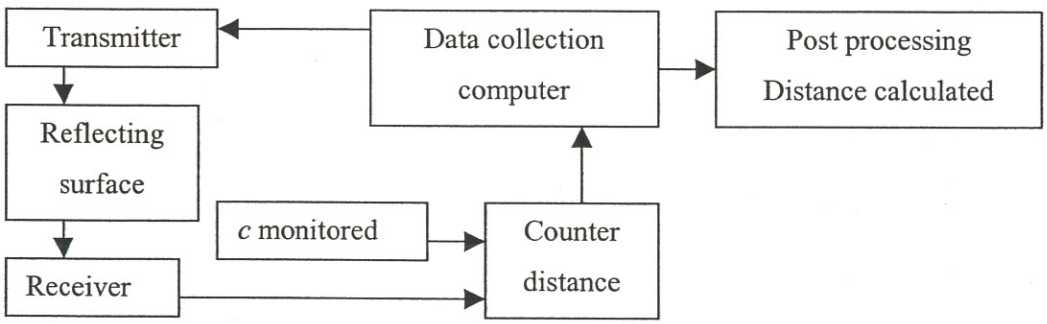

The accuracy of the NCPA ultrasonic probes appeared to be unaffected by the presence of suspended sediment (0.00009-0.018 kg/s), and when the water was turbid (Best and Ashworth, 1994). Erratic signals were filtered (Appendix I), and resulted from abrupt changes in the bed morphology. For example a moving coarse particle may result in multiple reflections due to the height variations within the measuring area. Alternatively a static large clast in the measuring zone may obscure the actual changes in the sediment bed height. The probe head surface was regularly checked for dirt and air bubbles which can cause measurement errors. It was also ensured that the temperature probe was immersed in the flume, and that all connections were correct.

Data from the Contaq probe also required filtering (Appendix I) as it produced occasional erroneous values due to the choppy nature of the water surface, resulting from the recirculation of the water and sediment by the two pumps. The erratic signals may therefore result from the reflection of the ultrasonic pulse from

In the fixed bed experiments a point gauge was also used to determine the bed height in the test section at 5 mm (± 0.5 mm) intervals. Since the sediment formed a solid surface, the bed height measurement error resulted only from reading the venier scale (± 0.1 mm).

2.4.4 Velocity and turbulence measurements –laser Doppler anemometry (LDA)

Laser Doppler anemometry (LDA) is one of a number of methods for determining fluid flow velocity (Buchhave and George, 1979), and offers numerous advantages as listed in Table 2.5.

Table 2.5: *Advantages and disadvantages of LDA. From Nezu and Nakagawa (1993), Biron et al. (1995) and Adrian (1996).*

Advantages	Disadvantages
• Non-intrusive. • Absolute measurement – no calibration required. • Does not depend on the thermophysical properties of the fluid. • Measures up to 3 velocity components. • Reversed flow can be detected. • Very accurate. • Can measure high frequency velocity fluctuations. • Can measure velocities from less than 10 μm s^{-1} to 1 km s^{-1}. • Can be used successfully in various types of flow e.g. supersonic, turbulent, capillary blood flow etc. • Excellent spatial resolution due to small measuring volume.	• Cannot be used in opaque flows. Data collection rates reduced in the presence of high levels of suspended sediment. • Difficult to measure close to bed, especially with more than one velocity component. • Unevenly spaced data. • Actually measure the speed of the seeding particles rather than the fluid. • Expensive.

Laser light has the following characteristics – monochromatic, coherent, linearly polarised, low divergence, and a Gaussian intensity distribution. The key features of the LDA measurement system are illustrated in Figure 2.9 and Table 2.6.

parallel to the flume base, accounting for the slope of the flume, and the vertical axis was perpendicular to this. The probe could be aligned to an accuracy of ± 0.5 mm in both horizontal and vertical directions.

Table 2.7: *Specifications of the LDA system employed.*

Feature	Specification	
	Green	**Blue**
Wavelength (nm)	514.5	488
Focal length (mm)	400	400
Beam diameter (mm)	1	1
Fringe spacing (um)	5.422	5.143
Number of fringes	48	48
Measurement volume (mm^3)	0.379	0.325
Dx (mm)	0.262	0.249
Dy (mm)	0.262	0.249
Dz (mm)	5.523	5.238
Signal gain (dB)	35	
Coincidence time (ms)	0.17	

In the mobile bed experiments, one vertical profile was taken in the test section, at the channel centre. Depending on the magnitude of the bedforms, each profile point was sampled for either 5 or 10 minutes. Records of the bed height were taken concurrently with an ultrasonic probe, a known distance downstream of the measuring volume, in order to eliminate any flow disturbance due to the immersed ultrasonic probe (Plate 2.5). The vertical elevation of the profile points were measured relative to the bottom of the ultrasonic probe. Measurements near the sediment bed and the water surface recorded only the downstream velocity component since the beams which assess the vertical velocity component are either intercepted by the sediment bed, or are not fully immersed in the water since they converge at an angle in the vertical plane. Starting as close as possible to the bed, the first ten profile points were collected at 1 mm intervals, the next five at 2 mm intervals, the subsequent two at 5 mm intervals and the remaining points at 10 mm intervals until the water surface is reached. During the series 1 experiments, approximately thirty points were taken to complete the velocity profile, whereas about twenty-seven were obtained for the runs in series 2.

Table 2.8: *Sources of noise in the LDA signal. From Livesey (1995), Adrian (1996) and Dantec (1996, 1998, 2000).*

- Photodetection shot noise (generated by the detector itself, limiting the SNR). Incoherent signals can result when a range of particle sizes are present.
- Secondary electronic noise, thermal noise from preamplifier circuit.
- Higher order laser modes (optical noise).
- Light scattered from outside the measurement volume, dirt, scratched windows, ambient light, multiple particles etc.
- Unwanted reflections e.g. windows, lenses and mirrors.
- Misaligned beams.

2.4.5 Camera and video

A 50 mm camera was mounted on the instrument carriage, and employed to take photographs of the test section from above at the end of each experimental run, requiring the water to be drained slowly from the flume first. Care was needed in order to minimise any disturbance to the sediment bed. A scale and a reference for the location in the flume were included in every photograph. During the experimental runs photographs and video recordings of the bedforms present were taken.

2.4.6 Temperature

The temperature of the water in the flume was measured regularly with a thermometer to ± 0.1 °C. The average temperature of the experimental runs varied from 22-28 °C.

2.5 Comparison of recirculating and sediment feed flumes and field observations

In the present experiments, both water and sediment are constantly recirculated within the flume system. Alternatively, sediment can be fed in at the upstream end of the flume, and the downstream sediment discharge removed from the system. Uniform sediments behave in the same manner for both recirculating and sediment feed flumes, but this is not the case for mixed sized or density mixtures as explained below (Parker and Wilcock, 1993). In order to achieve equilibrium, the quantity and grain size distribution of the sediment entering and leaving the system must be identical.

In a recirculating system only those grains which are entrained in the flume are present in the upstream sediment input. Differences in grain mobility therefore result in partial transport (transport rates for coarser fractions are less than those of the finer fractions), which can exist in a steady state in a recirculating system since the input of less mobile size fractions is reduced compared with their occurrence in the bulk sediment mixture (Wilcock and McArdell, 1993). The texture of the bed under steady state conditions is determined by the imposed hydraulic conditions (discharge, slope and depth), fractional grain mobility and the distribution of the bulk sediment mixture.

Chapter 3 : Morphological and textural characteristics of bedforms generated in a bimodal sand-gravel mixture

3.1 Introduction

Only relatively recently have low-relief bedforms in sand-gravel bimodal sediments been recognised (Kuhnle, 1986; Kuhnle and Southard, 1988; Whiting *et al.*, 1988; Dietrich *et al.*, 1989; Wilcock, 1992; Bennett and Bridge, 1995a; Livesey, 1995). Several factors have led to the identification of low-relief bedforms: more detailed observations, improved monitoring techniques and work conducted into the entrainment and bedload transport of different size fractions which compose heterogeneous sediments (Hammond *et al.*, 1984; Komar and Li, 1986; Drake *et al.*, 1988; Ikeda and Iseya, 1988; Ashworth and Ferguson, 1989; Dinehart, 1989; Ferguson *et al.*, 1989; Kirchner *et al.*, 1990; Kuhnle, 1993a; Wilcock, 1998). However, our quantitative knowledge of the morphological and textural characteristics of low-relief bedforms remains limited due to past technical difficulties of recirculating gravel sized sediment in a laboratory flume, incomplete data sets, the vast range of potential sediment mixtures, and the difficulty of classifying both bedforms and mixed-size sediment mixtures.

This chapter details the distinctive morphological, textural and dynamic characteristics of bedform populations identified by cluster analysis over a range of discharges in a bimodal sand-gravel mixture. In addition the method of bedform development and migration, and the resulting impact on sediment transport is examined.

3.2 Data analysis

3.2.1 Hydraulic conditions

The mean flow depth in the test section, d, was determined by subtracting the mean values of the filtered ultrasonic records of bed and water surface elevation at a point. The depth integrated velocity, U, was calculated from the velocity profile. Water surface slope, S, was obtained by subtracting the dynamic water surface elevations from the static heights and applying a least-squares linear regression. An average value calculated was calculated for each experiment by repeating the procedure several times. The slope was used to determine the spatially averaged boundary bed shear stress, τ_0, from

$$\tau_0 = \rho g d S \tag{3.1}$$

where, ρ is fluid density, and g is gravitational acceleration. This value was corrected using the method detailed by Williams (1970) and shown in Equation 3.2, where d is water depth and w is flume width.

dependent on the sampling technique, and C is a proportionality constant unique for each sample. The conversion factor was determined by comparing volumetric and clay piston samples of the bulk sediment mixture (Diplas and Fripp, 1992).

3.3 Results

3.3.1 Hydraulic conditions

The mean equilibrium hydraulic conditions are detailed in Table 3.1.

Table 3.1: *Mean equilibrium hydraulic conditions. d is flow depth (± 3 %), U is the depth averaged velocity, Q is mean flow discharge (± 4 %), S is water surface slope (± 12 %), Fr is the Froude number ($Fr = U/\sqrt{gd}$), τ_{R0} is the bed shear stress obtained from projections of Reynolds stress measurements, θ is the mean dimensionless bed shear stress and f is the Darcy-Weisbach friction coefficient ($f = 8gds/U^2$). SR, R, BLS and LRBW represent sand ribbon, ripple, bedload sheet and low-relief bed wave respectively.*

Run	d (m)	U (m/s)	Q (m^3/s)	S ($\times 10^{-3}$)	Fr	τ_{R0} (Pa)	θ	f
			Series 1 (d = 0.18 m)					
A (SR)	0.172	0.51	0.026	1.87	0.39	1.73	0.195	0.053
B (R)	0.172	0.58	0.032	1.96	0.45	2.63	0.285	0.063
C (BLS)	0.181	0.68	0.038	2.20	0.51	3.36	0.378	0.058
D (BLS)	0.173	0.74	0.039	2.27	0.57	3.62	0.393	0.053
E (BLS)	0.176	0.82	0.045	2.65	0.62	4.01	0.344	0.048
F (LRBW)	0.178	0.87	0.047	3.09	0.66	3.43	0.291	0.036
G (LRBW)	0.176	0.88	0.049	3.51	0.67	5.99	0.441	0.062
H (LRBW)	0.177	0.95	0.052	4.33	0.72	6.51	0.457	0.058
			Series 2 (d = 0.14 m)					
I (R)	0.138	0.59	0.025	2.32	0.51	4.05	0.464	0.093
J (BLS)	0.141	0.70	0.029	2.51	0.60	3.37	0.366	0.055
K (BLS)	0.150	0.71	0.031	2.88	0.59	3.46	0.345	0.055
L (LRBW)	0.142	0.79	0.034	3.59	0.67	4.12	0.327	0.053
M(LRBW)	0.139	0.90	0.040	4.89	0.77	6.11	0.194	0.060
N (LRBW)	0.141	1.04	0.047	6.08	0.88	7.92	0.176	0.059

3.3.2 Bedform classification, morphology and dynamics

Figures 3.1 and 3.2 highlight the height and period of the bedforms recognised in the bed records. The shape of the bedforms in the ultrasonic profiles depends on the size of the form relative to the sediment transport rate and local bed roughness, its orientation, the occurrence of any superimposed features and how long it has existed.

Cluster analysis is a multivariate technique which identifies groupings within data sets when the number of groups and group membership are not known. However, there is no underlying theoretical model. In order

Figure 3.2: *Simultaneous bed records taken a known distance apart. Examples of each bedform type are taken over a range of discharges. Flow is from right to left. R, BLS and LRBW represent ripples (Run B), bedload sheets (Run K) and low-relief bed waves (Run H). Where only ripples were present, migration rates could be calculated from the position of the crest when the bed record was 'stunted' by the presence of a coarse clast in the measuring volume.*

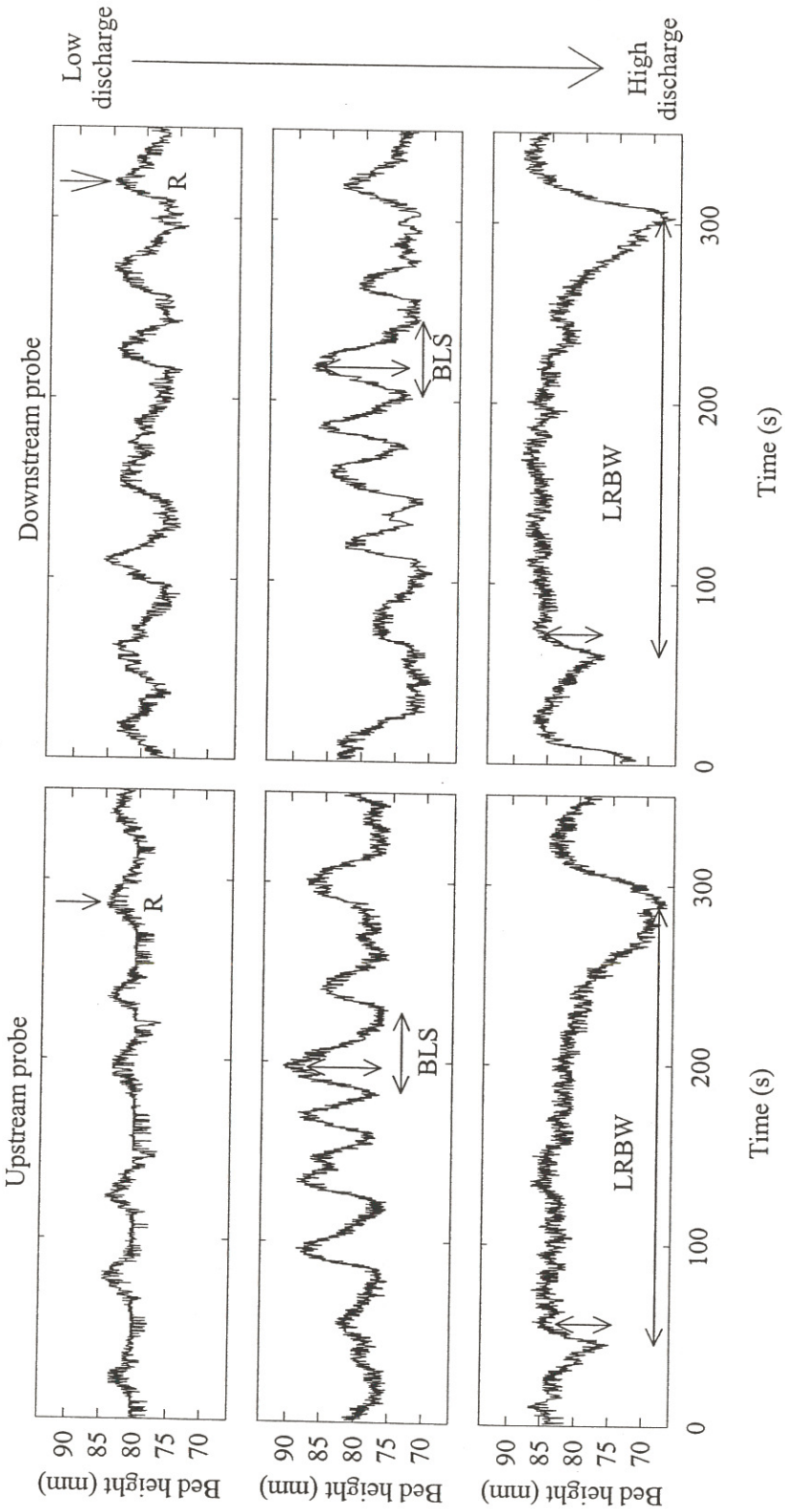

K-means clustering uses the first *k* (the number of clusters specified by the user) data points as initial estimates for the cluster centres. Every bedform is then assigned to the closest cluster centre, which are then recalculated. An iterative procedure allows the final cluster centres to be determined. The distance of a point from the cluster centre can help indicate outliers. Cluster centres can also be specified based on earlier analysis. Therefore the measurements of bedform migration rate and length can be assigned to the predetermined populations if the associated bedform height and period are also known.

K-means analysis was repeated for different numbers of cluster centres. The hierarchical method was used on a subset of the data (40 individual bedforms each time). Graphical and statistical output enabled the number of bedform populations for each run to be determined and compared (Figure 3.4). The cluster analysis technique identified three distinct bedform populations based on bedform height and period measurements (Table 3.2). Due to inherent variability, bedform populations rather than individuals are discussed here (Roden, 1998).

Figure 3.4: *Example plot of bedform period against height for run M illustrating cluster membership. The logarithm of bedform period and height is taken and scaled from 0 to 1. BLS and LRBW represent bedload sheets and low-relief bed waves respectively.*

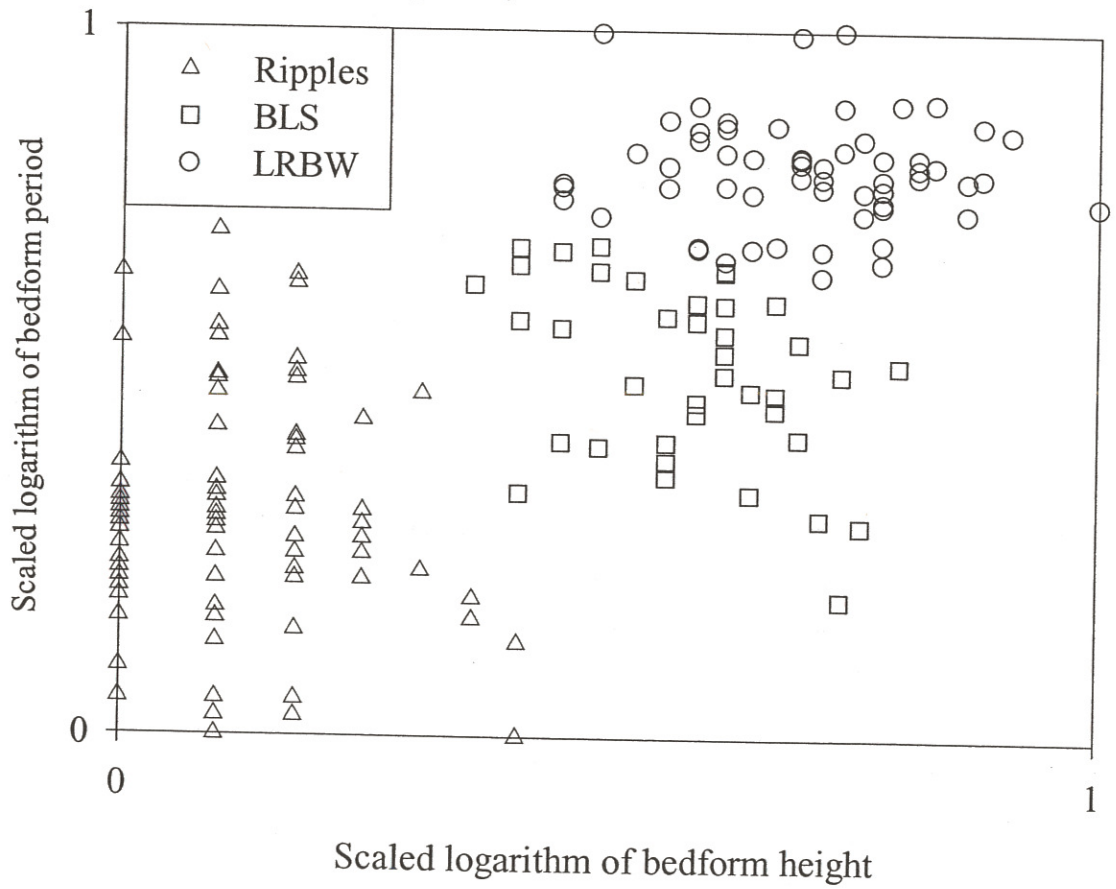

The second bedform population identified by cluster analysis develops with further increases in bed shear stress. These bed features are characterised by heights of 7-12 mm, lengths of 71-1061 mm, periods of 30-69 s and migration rates of 8-27 mm/s. Between the individual forms it is common to find an area of gravel lag since the flow is not capable of moving all the grain size fractions available in the bed. These bedforms share many similarities with previous observations of bedload sheets (Table 3.3 and Figures 3.1 and 3.2), and are less regularly spaced and taller than ripples, which can be superimposed on the stoss of the bedload sheets. Bedload sheets are present in all experimental runs with the exception of A, B, and I.

At the highest flow discharges employed, the largest bedforms developed, the height and migration rate of which was dependent on flow depth. Where flow depth was 180 mm, these bedforms exhibited heights of 13-15 mm and migration rates of 9-14 mm/s. This changed to 8-10 mm and 11-25 mm/s respectively when flow depth was reduced to 140 mm. However, the length (2.3-4.8 m) and period (116-256 s) were not affected by the change in the depth of flow. These bedforms (termed here low-relief bed waves) were differentiated by their much greater length, crestal platform and gentle stoss side, on which both bedload sheets and ripples were superimposed (Figures 3.1 and 3.2 and Table 3.3). The trough appeared fairly flat, and is dominated by a gravel armour which can be mobile (i.e. at the highest bed shear stress employed the flow was capable of moving all grain size fractions). Low-relief bed waves were observed in runs F, G, H, L, M and N.

The total water discharge during runs C/D, F/G and J/K are similar, and the morphological characteristics of the bedforms generated are comparable (Table 3.4) illustrating the repeatability of the results presented here. However, Werner and Kocurek (1999) caution that bedform spacing in laboratory flumes may vary depending on the size of the test section, and may also differ from that found in the field.

3.3.3 Bedform texture and bedload transport

Due to their low-relief, bedforms were most noticeable from their characteristic concentrations of fine and coarse bed material. As discharge increased, the mean grain size of the bedload and crestal surface tended to become greater, whilst the standard deviation and skewness fell (Table 3.5). At the lowest transport rates, the finer and coarser fractions are under-represented in the bedload when compared with their occurrence in the bulk sediment mix (either immobile or partially mobile, Wilcock and Southard, 1989). The finer sediment sizes may be underrepresented in the bedload due to suspension and hiding effects (Wilcock and McArdell, 1993), whereas coarser particles typically require a greater shear stress for entrainment. When all the exposed clasts of a given size interval are entrained and transported at least some of the time, that grain size can be considered fully mobile. Near incipient motion the central grain size fractions are most mobile. However, as shear stress increases the difference in mobility between grain size fractions is reduced, and in the case of run N equal mobility is nearly attained. Runs C/D and F/G experienced similar total water discharge, and the grain size distribution of the bedload is also comparable (Table 3.5) indicating the reproducibility of the results.

The mean, standard deviation and skewness of the grain size distributions for the trough and stoss regions are fairly stable for the ranges of discharges investigated here (Table 3.5). Divergent values may result from the presence of superimposed bedforms on the stoss, and coarse, immobile particles protruding through the thin bedform.

Figure 3.5: *Representative grain size distributions for a ripple (a, run I), bedload sheet (b and c, run K and C) and low-relief bed wave (d and e, run M and N) bed configurations. Note the difference percentage scales used.*

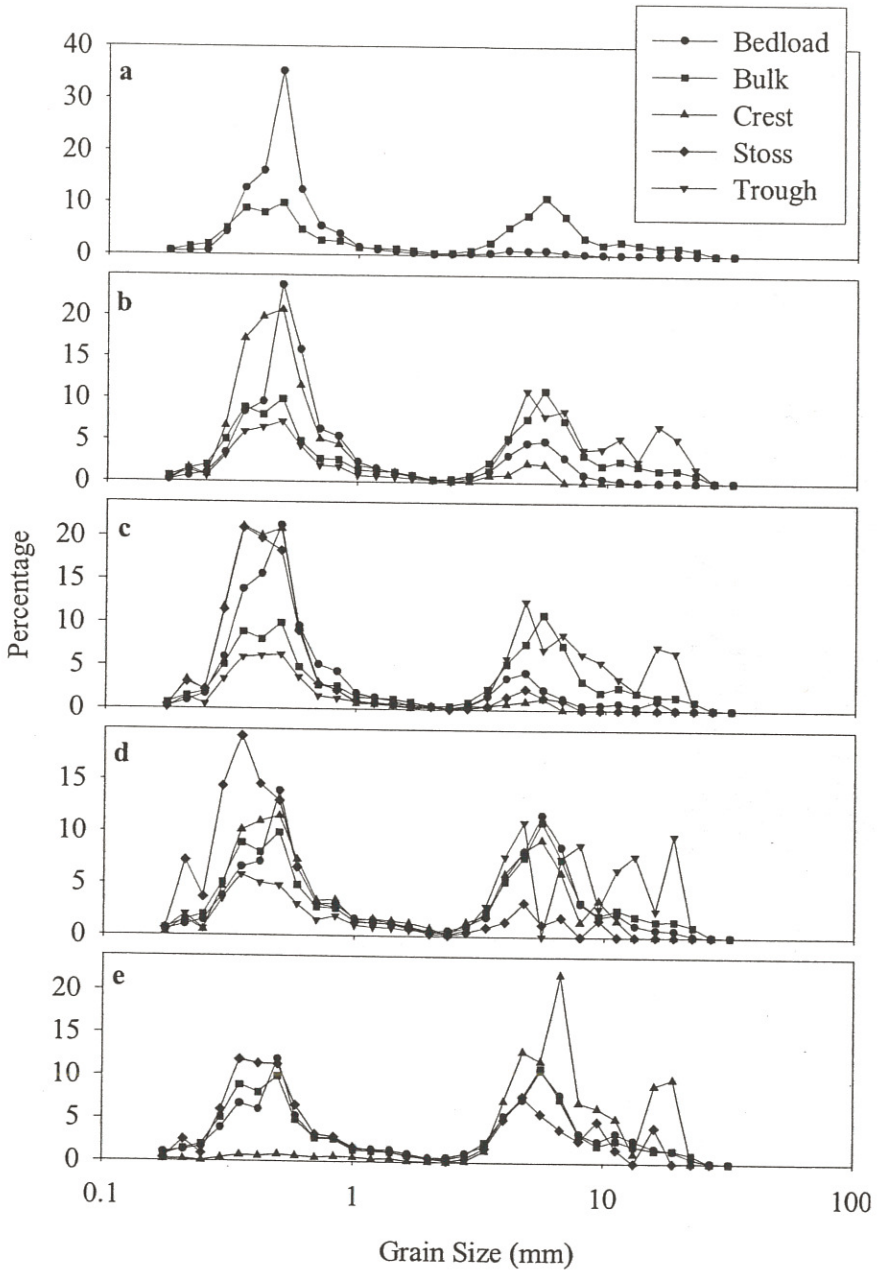

An armoured surface is characteristically coarser and better sorted than the underlying bed sediment/bulk mixture, with a thickness of one grain diameter (Gomez, 1983). A variety of interchangeable terms have been used to describe this surface feature (Proffitt and Sutherland, 1983; Komar, 1987b; Parker, 1991a; Richards, 1991; Kuhnle, 1992; Reid *et al.*, 1992). Gomez (1984) suggests that a stable/static armour represents a segregated surface which is inactive under the prevailing flow conditions, whereas an unstable/mobile armour experiences periodic movement. Gravel can be segregated on the bed surface by three mechanisms: concentration of particles at the base of the active layer, winnowing of fines and deposition of coarse particles (Gomez, 1984). An armour layer limits the availability of sediment for

Plate 3.2: *Bedload sheet run K. Flow is from top to bottom. Channel width is 0.356 m.*

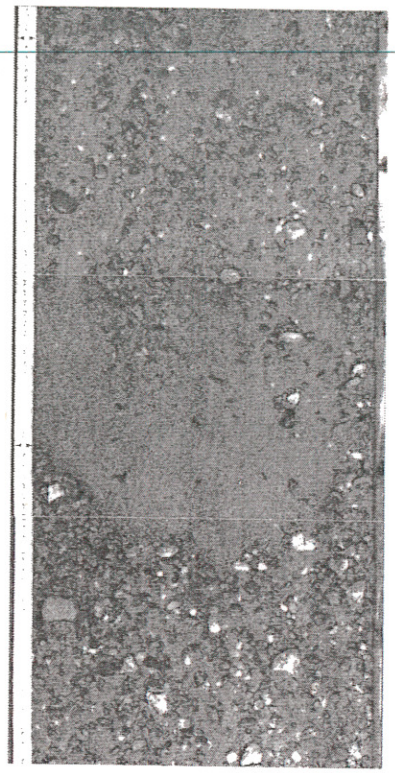

In the case of low-relief bed waves, the grain size distributions of the crest, bedload and bulk mixture are comparable (Figure 3.5d). However, the very coarsest size fractions of the bulk mix are under-represented or absent in the bedload and crest. In this case, the bedload, crest and bulk mix contain no particles greater than 26.9, 13.2 and 32 mm respectively. These coarsest particles characterise the trough and represent a static armour (Plate 3.3). Sediment samples from the bedform stoss confirmed visual observations that it was predominantly composed of sand, with small quantities of overpassing pea gravel (Plate 3.3).

In run N (low-relief bed waves), all size fractions were represented in the bedload, which exhibits a grain size distribution akin to the bulk sediment mix (Figure 3.5e). Evidently this flow was capable of moving all the sediment available in the bed (up to 32 mm). Therefore the crest, which is characterised by an overpredominance of the coarsest grains, represents a mobile armour layer. Bennett and Bridge (1995a) speculated that when the bed material is fully mobile (Wilcock and McArdell, 1993), the grain size contrast between bedform crests and troughs is eliminated, or even reversed. The grain size distribution of the stoss was similar to that of the bedload and bulk mixture, although marginally finer.

The observations from Figure 3.5 confirm that as discharge increases, and different characteristic bed configurations dominate, the bedload and crestal region coarsen. Furthermore the dynamics of the coarse armour layer change as flow strength increases and the large clasts become mobile.

Figure 3.6: *Textural variations over a low-relief bed wave, run G, series 1. Flow is from right to left. C, T and S represent samples of the crest, trough and stoss respectively. Average values for the trough and crest are used in the grain size distribution curve.*

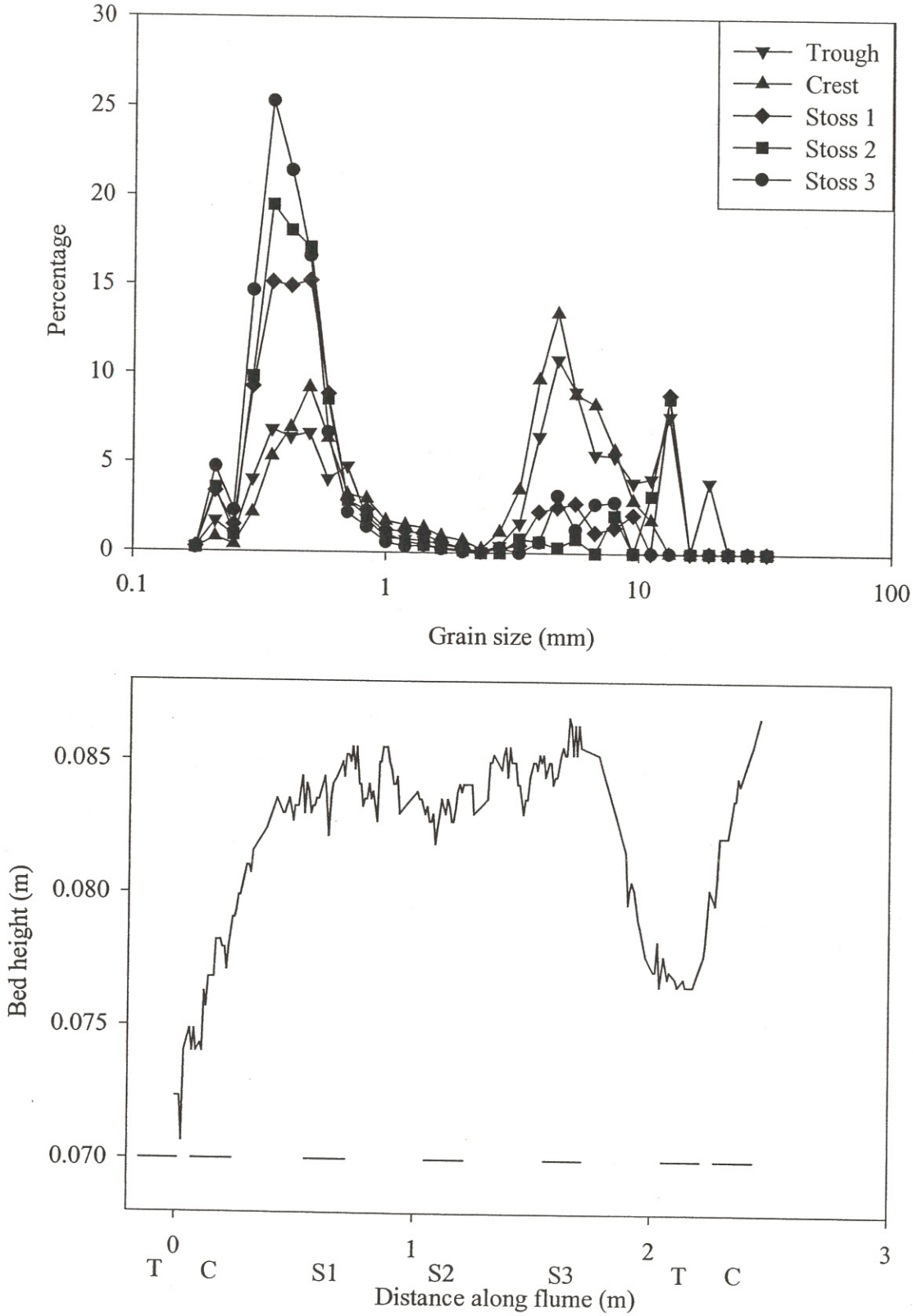

Table 3.7: *Summary of the sedimentological characteristics of the present experiments and previous work on bedforms in bimodal sediment mixtures. θ is the dimensionless bed shear stress and q_b is the total bedload transport rate.*

Source	Bedform	Bulk sediment		θ	q_b	Texture D_{50} (mm)			
		D_{50} (mm)	$\sqrt{D_{84}/D_{16}}$		(kg/ms)	Bed Load	Crest	Stoss	Trough
Present study									
	Ripples	1.819	4.3	0.09	0.006-0.014	0.603	-	-	-
	BLS	1.819	4.3	0.10-0.12	0.036-0.101	0.929	0.609	1.481	3.292
	LRBW (1)	1.819	4.3	0.14-0.21	0.241-0.253	1.365	3.332	0.755	3.377
	LRBW (2)	1.819	4.3	0.14-0.24	0.157-0.591	1.725	4.315	2.429	3.777
Baas (1993)									
	Ripples	0.238		0.14-0.52					
Bennett and Bridge (1995a)									
	BLS	1.9-2.0	1.7-1.9	0.04-0.10	0.010-0.043	2.33	1.5-3.1	Mixed	2.3-5.4
	LR bars	1.9-2.0	1.7-1.9	0.04-0.10	0.010-0.043	2.33	-	-	-
Kuhnle (1986)									
	BLS	2.8	2.6	0.12-0.16	0.034-0.098	-	1-4	-	4-16
	Dunes	2.8	2.6	0.16	0.9	-	-	Fine	Coarse
Whiting *et al.* (1988)									
	BLS (DC)	4.6	2.6	0.07-0.11	0.038	-	6.1	-	4.1
	BLS (MC)	4.6	2.6	-	-	-	-	-	-
Dietrich *et al.* (1989)									
	BLS	3.7	2.2	0.08-0.09	0.010-0.029	-	4.7	2.7	3.7
Wilcock (1992)									
	BLS (MC50)	2.6	1.7	0.07-0.10	0.018-0.063	-	Coarse	Well mixed or fine	
	2D dunes (MC50)	2.6	1.7	0.12-0.14	0.131-0.223	-	-	-	-
Livesey (1995)									
	BLS	1.07	1.57	0.086-0.145	0.068-0.129	1.2	Fine	Mixed	Coarse
	LR bedforms	1.07	1.57	0.086-0.145	0.068-0.129	1.2	1.0	1.1	1.4

was typically a much smaller percentage of the downstream velocity component, although the depth averaged velocities generated in the experimental runs were considerably larger. Secondary circulation generated due to a low width/depth ratio can also cause variations in the spanwise distribution of bed shear stress. In order to allow comparison between data sets any sidewall effect must be accounted for (Equation 3.2; Williams, 1970).

Figure 3.9: *Secondary flow circulation (m s^{-1}) with a flow depth of a) 0.18 m and b) 0.14 m. No sediment was present in the flume. Flow is into the diagram, with the area from the left sidewall looking downstream to the centre of flume shown.*

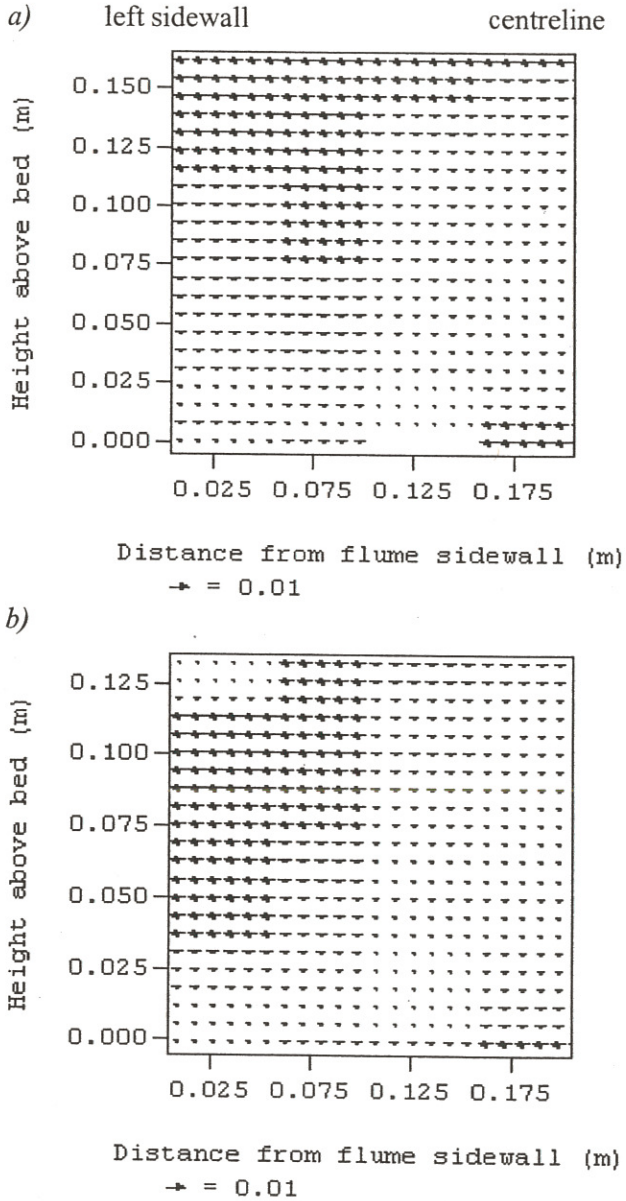

Figure 3.10 highlights the fact that both the length and period of ripples and bedload sheets are similar. These two features are therefore morphologically distinguished by their height, which is greater for the bedload sheets. Low-relief bed waves are longer than the other two bedform populations identified, and their height is dependent on the flow depth, which under the present flow conditions is either similar or greater

waves. The migration rate of all bedform populations is directly related to the spatially averaged bedload transport rate (Figure 3.11), which is expected as suspended sediment transport is minimal. All bedforms seem to have a greater migration rate under shallower flow conditions at the highest discharges (i.e. run M and N).

Figure 3.11: *Bedload transport as a function of bedform migration rate. Each point represents an average value for a particular bedform and run. BLS and LRBW represent bedload sheets and low-relief bed waves respectively.*

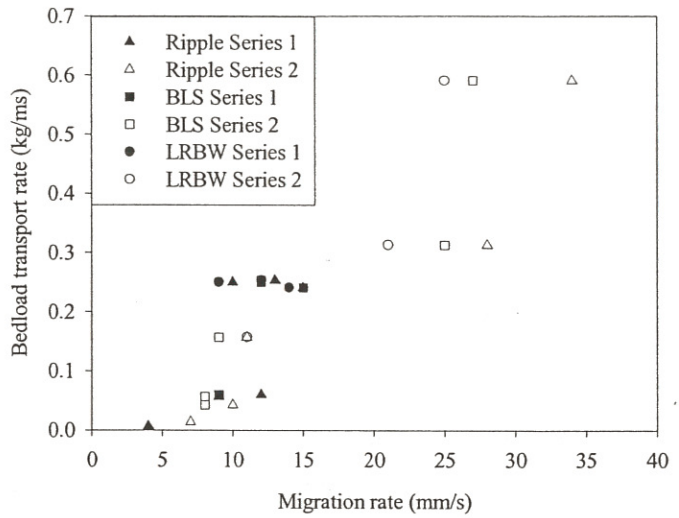

Gabel (1993) noted four ways in which bedforms transform morphologically. Examples of amalgamation and destruction from the present experiments are shown in Figure 3.12. For each case there are two simultaneous bed height records, taken a known distance apart (typically 0.2 m), enabling specific bed features to be correlated. Firstly, bedforms can be destroyed by simply dying out i.e. diminution (Figure 3.12a). Bedforms can also combine together (Figure 3.12b). This often occurs when a bedform travels up the stoss of a slower moving downstream feature and the two amalgamate so that only one lee side is present. Conversely, a bedform can split into two separate features. Finally, a bedform can simply develop from a previously flat area of the bed. However, evidence for these last two morphological transformations was not observed in the present experiments. Carling *et al.* (2000a) proposes a fifth classification to describe bedforms which are regenerated on the stoss side of larger features. However, this is associated with changes in flow stage and is therefore not applicable to the bedforms generated in the present experiments under uniform flow conditions.

Figure 3.13: *Variations in bedform height, length, period and migration rate with discharge. BLS and LRBW represent bedload sheets and low-relief bed waves respectively.*

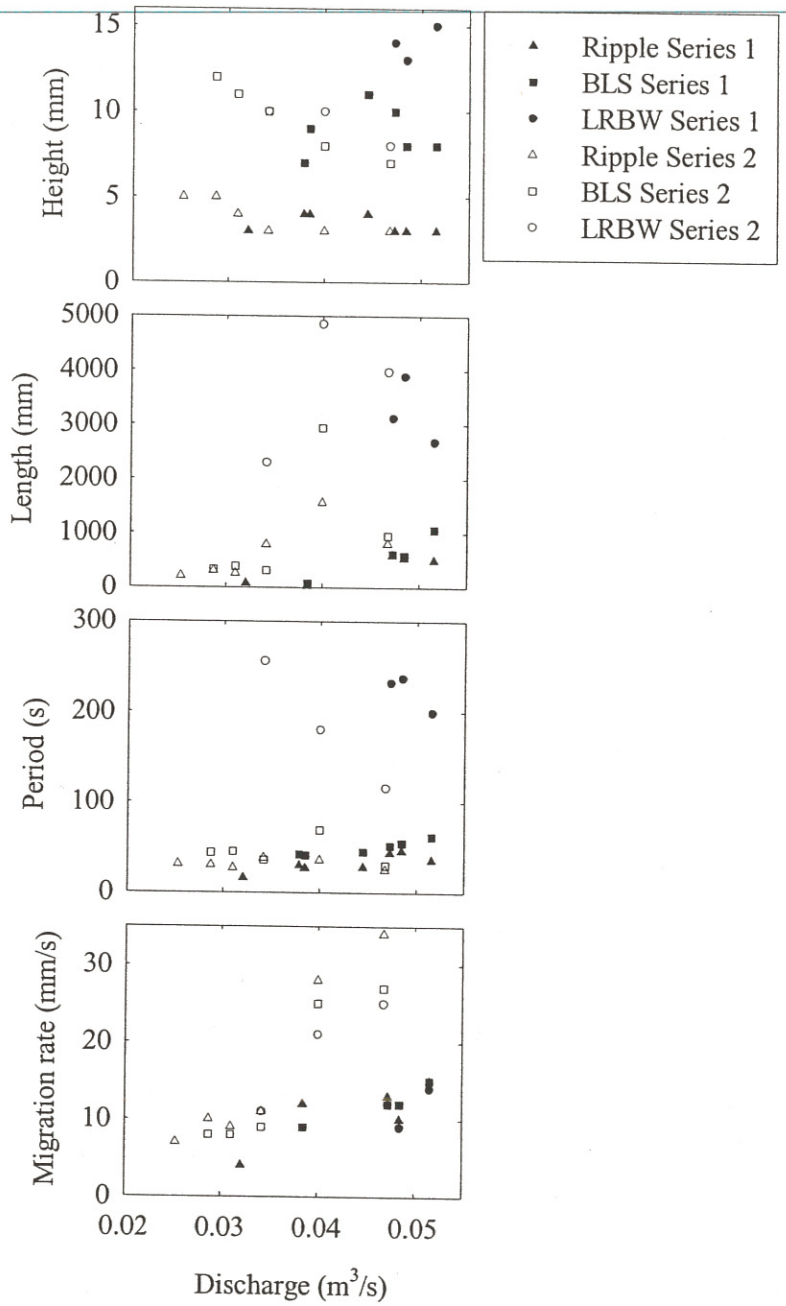

As discharge increases the mean grain size of the bedload and crestal region increases (Figure 3.14). This effect is enhanced under shallower flow conditions (Series 2), where bed shear stresses are greater for a given discharge (Table 3.1). Rapid coarsening of the crest is linked to the development of low-relief bed waves, which first occur at a lower discharge under the shallower flow conditions. The texture of the trough seems to remain fairly similar under a wide range of conditions, whereas the stoss region exhibits no obvious trend.

buried beneath the coarser clasts can only be exposed to the flow once the larger grains have been entrained (Kuhnle and Southard, 1988). The stoss side of the low-relief bed waves were observed to fine in the present experiments in the upstream direction, which explains why Kuhnle and Southard (1988) measured the maximum transport rate being further delayed for decreasing sand size fractions. In the case of bedload sheets and low-relief bed waves, the approach of the bedform crest also caused the water surface to dip (Bennett and Bridge, 1995a; low-relief bars). Consequently, bedload sheet and low-relief bed wave migration cause periodic variation in bed shear stress and bedload transport rate (Figure 3.15) of up to ten orders of magnitude (Whiting *et al.*, 1988). Where bedload sheets are superimposed on low-relief bed waves, secondary fluctuations in bedload flux can be observed (Gomez *et al.*, 1989; Bennett and Bridge, 1995a; Livesey *et al.*, 1998).

Figure 3.15: *Variations in bedload transport rate. Records of the bed and water surface height are shown alongside in order to give an impression of the bed morphology and water surface slope during bedload transport sampling. Although the measurements of bedload transport overlap temporally with the other records, they are not simultaneous. The water and bed surface measurements were taken concurrently. However the water surface measurement probe was located 0.145 m upstream of the bed height measurement probe.*

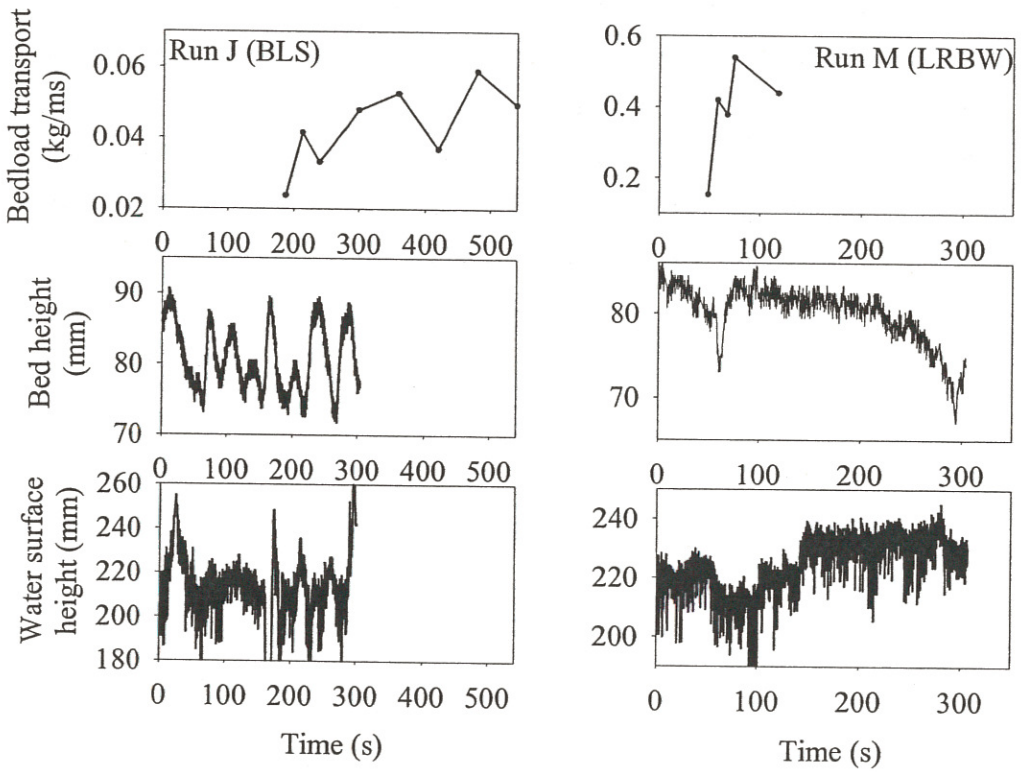

In the case of bedload sheets and low-relief bed waves, the crest and bedload exhibited a similar grain size distribution, indicating that any mobile sediment is transported within the migrating bedform. Grain size samples from the surface of ripples could not be collected due to their small size relative to the area sampled using the clay piston technique. However, visual observations and the grain size distribution of the bedload indicate that ripples were composed mainly of sand. The average bedload sediment transport rate, q_{bf}, for

Figure 3.16: *Comparison of bedload and bedform transport rate. BLS and LRBW represent bedload sheets and low-relief bed waves respectively.*

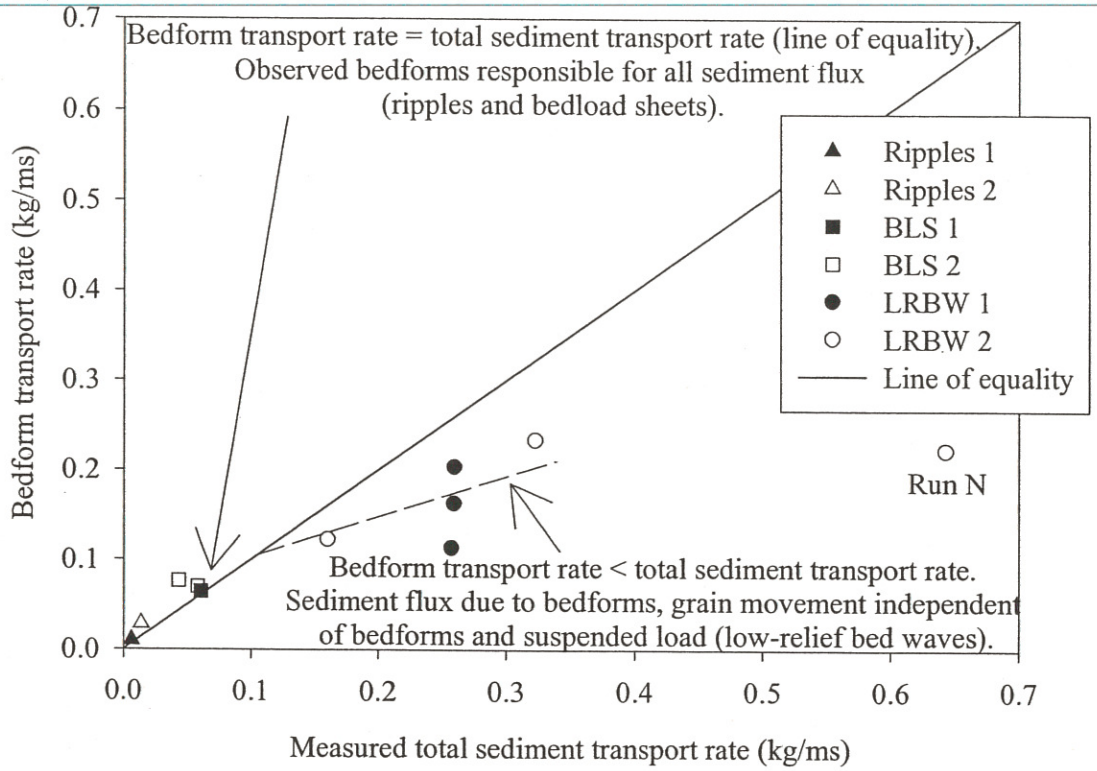

3.4.4 Conceptual model for sediment transport in bimodal mixtures

In bimodal mixtures, the relatively fine grain sizes are entrained first, forming isolated longitudinal stripes of finer material (Iseya and Ikeda, 1987; Ferguson *et al.*, 1989; Parker, 1991b; Nezu and Nakagawa, 1993; Tsujimoto and Kitamura, 1996; Tsujimoto, 1999). As these sandy patches grow in volume and migrate over a static armour consisting of the coarse size fractions, they eventually develop into ripples (Allen, 1968; Southard and Dingler, 1971; Williams and Kemp, 1971; Leeder, 1980; Ikeda and Iseya, 1988; Baas, 1999). With further increases in mean bed shear stress, larger clasts are entrained from the surrounding coarse armour layer. Although ripples have been shown to be absent in uniform sediment mixtures containing a grain size greater than 0.7 mm (Leeder, 1980), the present experiments in a bimodal sediment mixture generated ripples with clasts greater than 0.7 mm in diameter (Figure 3.5). The occurrence of larger grains within the ripple forms is explained by the overpassing of coarser particles. Isolated gravel clasts were observed to be entrained at roughness transitions (e.g. the boundary of the fine grained stoss and the coarse armour layer) and proceed quickly along the sandy stoss of the bedforms, this being promoted by a low friction angle and high relative protrusion.

With increasing flow strength, ripples develop into bedload sheets as the bedload incorporates more coarser clasts, although a static armour remains in the bedform trough. The increased mean size of sediment in

Table 3.8: *The entrainment, transport and deposition of sand and gravel size fractions.*

Action	Sand	Gravel
1 Entrainment (Transitional)	Sand is entrained along the bedform stoss.	Where the interstices of the gravel are filled with sand from the upstream region of the stoss, the loss of momentum due to the collective wakes is decreased. Therefore any elevated, coarse grains will be subjected to an increased drag force (exposure effect of Iseya and Ikeda; 1987). The fine infilling may also diminish the frictional resistance experienced by the coarser sediment (i.e. smoothing). As larger grains are entrained more bed sediment is exposed to the flow (Wilcock and McArdell, 1993). In the trough, gravel clasts were entrained from their stable position by scour and collision (Kuhnle, 1986; Kuhnle and Southard, 1988).
2 Transport (Smooth)	Sand tends to move in long, low waves in order to traverse the gravel armour (Kuhnle, 1986), but can also be suspended. Coarse sand grains move across the bedform in spatially and temporally fluctuating streaks (Wilcock and McArdell, 1993).	Transported gravel is elevated above the sandy stoss whilst in motion. Step lengths are very long, and the clasts move rapidly in isolation (Wilcock and McArdell, 1993). Streaks and patches of coarser sediment can be observed which may represent the trough/crest of superimposed bed features.
3 Deposition (Congested)	Sand avalanches down the lee side of the bedform and is buried by subsequent sand grains. The sand also covers any immobile coarse particles contained in the trough region.	As the gravel grains reach the coarse trough/crest they interact and are either deposited or decelerated. The coarse trough is characterised by greater roughness and lower near-bed flow velocities and higher shear stresses (Kuhnle, 1996). At high discharges large grains can move over the stoss of the next downstream bedform without being deposited in the trough region (Wilcock and McArdell, 1993). It becomes less likely to find a stable rest position with increasing discharge and grain size. This size selective trapping may influence fractional transport rates.

3.4.5 Comparison with dunes

Bedload sheets may be genetically related to two-dimensional dunes which develop in well sorted, coarse sand (Costello and Southard, 1980; Wilcock and Southard, 1989; Raudkivi and Witte, 1990; Ditchfield and Best, 1992; Best, 1996). The average, equilibrium hydraulic conditions associated with each of the three bedform populations identified in the present study were all found to plot as dunes on the bedform phase diagrams presented by Southard and Boguchwal (1990, p. 663, Figure 2N, O and P for ripples, bedload sheets and low-relief bed waves respectively). However, Southard and Boguchwal's (1990) bedform phase plot does not specifically classify bedload sheets and low-relief bed waves. Figure 3.17 illustrates that the present data plots in either the dune, two-dimensional dune or bedload sheet region of Best's (1996) bedform phase diagram depending on the selection of a representative grain size. The height of low-relief bedforms scale with the largest grains in transport, and are reduced compared with those of dunes (Ashley, 1990). Furthermore, dunes are steeper (0.08; Carling, 1999) than the low-relief bedforms observed in this study

3.5 Conclusions

1) With increasing bed shear stress the following traverse to flow bedform populations were observed: ripples (up to 5 mm high and 802 mm long), bedload sheets (up to 12 mm high and 1061 mm long) and low-relief bed waves (up to 10-15 mm high (dependent on flow depth) and 4849 mm long). The latter two bedform types have received little detailed attention in the literature, due to their relatively recent recognition. The bedforms were identified from their morphological dimensions (i.e. height and period) using the multivariate technique of cluster analysis.
2) The extensive data set presented enables variations in bedform morphology and texture to be documented over a wide range of discharges, from near incipient motion to just below supercritical flow conditions. With increasing shear stress the similar grain size distributions of the crest and bedload both coarsen, and the dynamics of the armour layer change. The height of the low-relief bed waves scales with the largest grains in transport. However, the height of the low-relief bed waves is also dependent on flow depth.
3) Fluctuations in both total and fractional bedload transport are related to bedform migration, which is established by the similar nature of the bedload and bedform crest grain size distributions, and the correspondence of bedload and bedform transport rates. However, while the migration of ripples and bedload sheets accommodates all the sediment in transport, this is not the case when low-relief bed waves are present, and additional contributions are made to total sediment transport. Ripples have periods up to 46 s and migrate at up to 34 mm/s. The period of bedload sheets extends to 69 s, and their maximum velocity is 27 mm/s. Low-relief bed waves are characterised by a period of up to 256 s and a maximum celerity of 25 mm/s. The variations in migration rate facilitates bedform superimposition and amalgamation.
4) A conceptual model of sediment transport in a bimodal mixture is presented. Sediment composing the bedforms moves along a dune-like grain path. Exceptions to this are the finer particles which are transported in suspension and the coarsest particles which once entrained can rapidly traverse several bedforms before being deposited. With increases in bed shear stress, these alternative transport mechanisms become more predominant.

Figure 4.1: *Representative examples of the determination of water surface slope over a fixed bed. A linear least-squares regression (significant at 95%) is applied to the measured static water elevations once the equivalent dynamic values have been subtracted for all points greater than 7 m downstream of the headbox.*

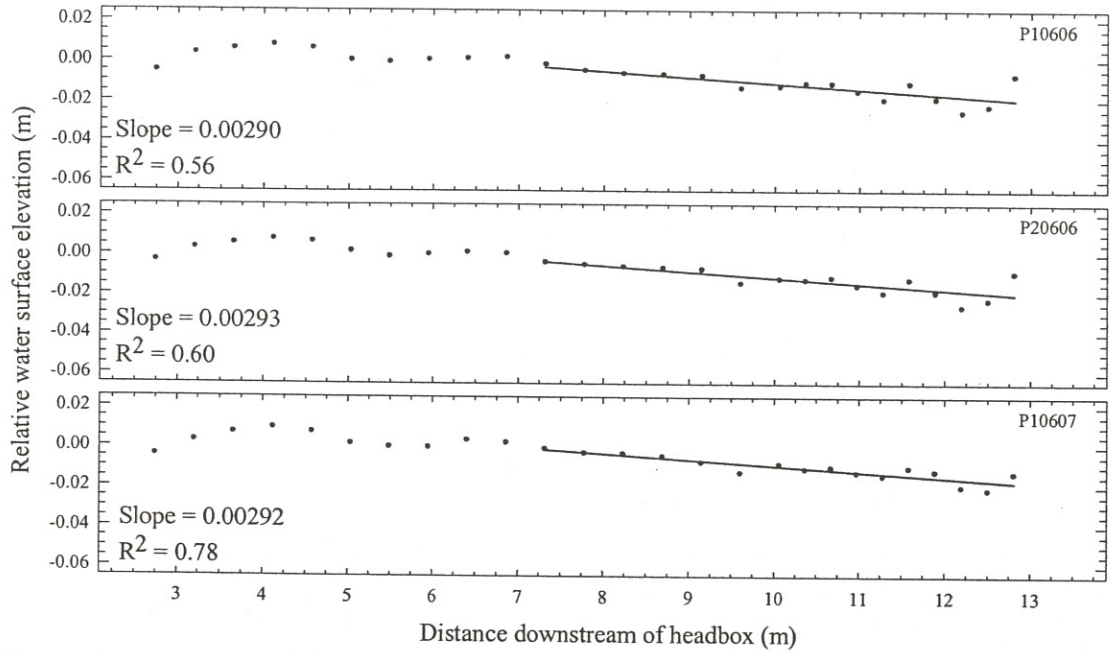

Figure 4.2: *Division of the bed height time series into specific bedform regions. The example is taken from run F where low-relief bed waves are the highest order bedform group present.*

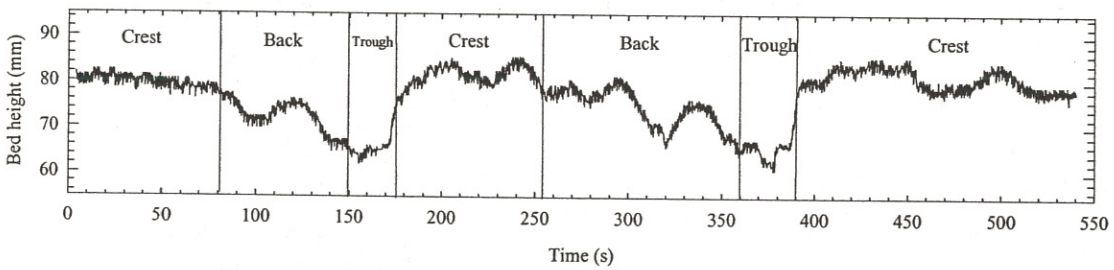

4.2.2

Sediment bed-elevation records

In the mobile bed experiments, the ultrasonic time series of bed elevations at-a-point were filtered to remove spikes, before the time averaged bed height was calculated. A mean bed height was also determined for specific sections of the bed record. In accord with Livesey (1995), the bed height time series was subdivided based on bedform morphology i.e. crest, stoss and trough of the highest order bedform group present, with ripples being the lowest order and low-relief bed waves the highest (Figure 4.2). In the fixed bed cases, the bed height was measured with a point gauge at the location of each velocity profile.

4.2.3 Laser Doppler anemometry (LDA) records – flow velocity profiles

For each at-a-point measurement of flow velocity, various time-averaged parameters were determined, which also represent spatial averages over a number of bedforms in the mobile bed cases. However, in the fixed

Figure 4.3: *Bed elevation map of the test section dominated by bedload sheets. The position of the transect (0.6 m) along which velocity and turbulence measurements were taken is shown by the black line. Flow is from right to left.*

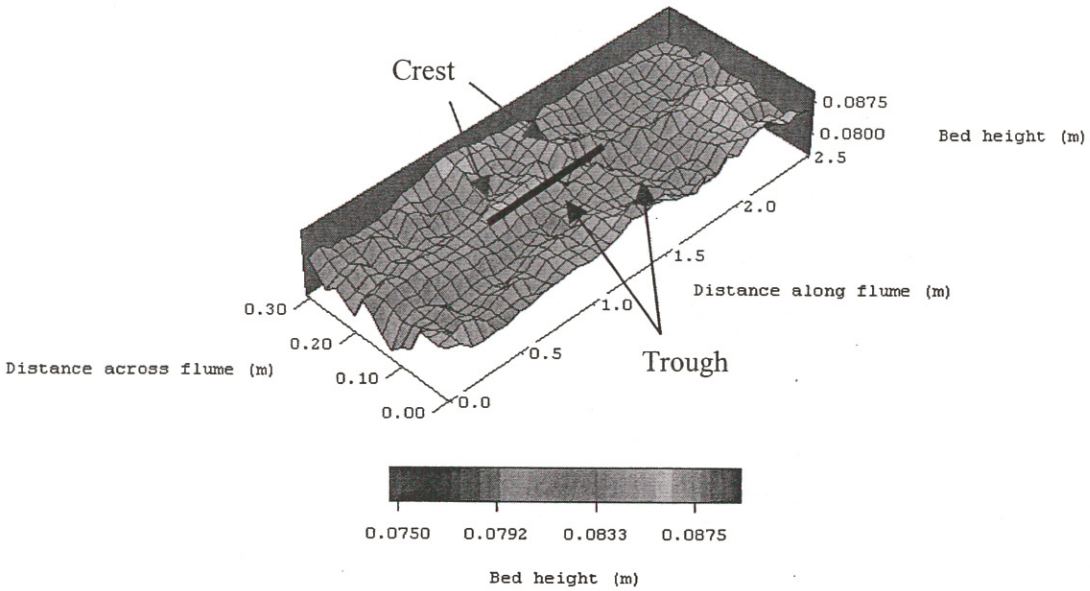

Figure 4.4: *Position of velocity and turbulence measurement points over a bedload sheet. Flow is from right to left. Solid and white symbols represent one and two component measurements respectively.*

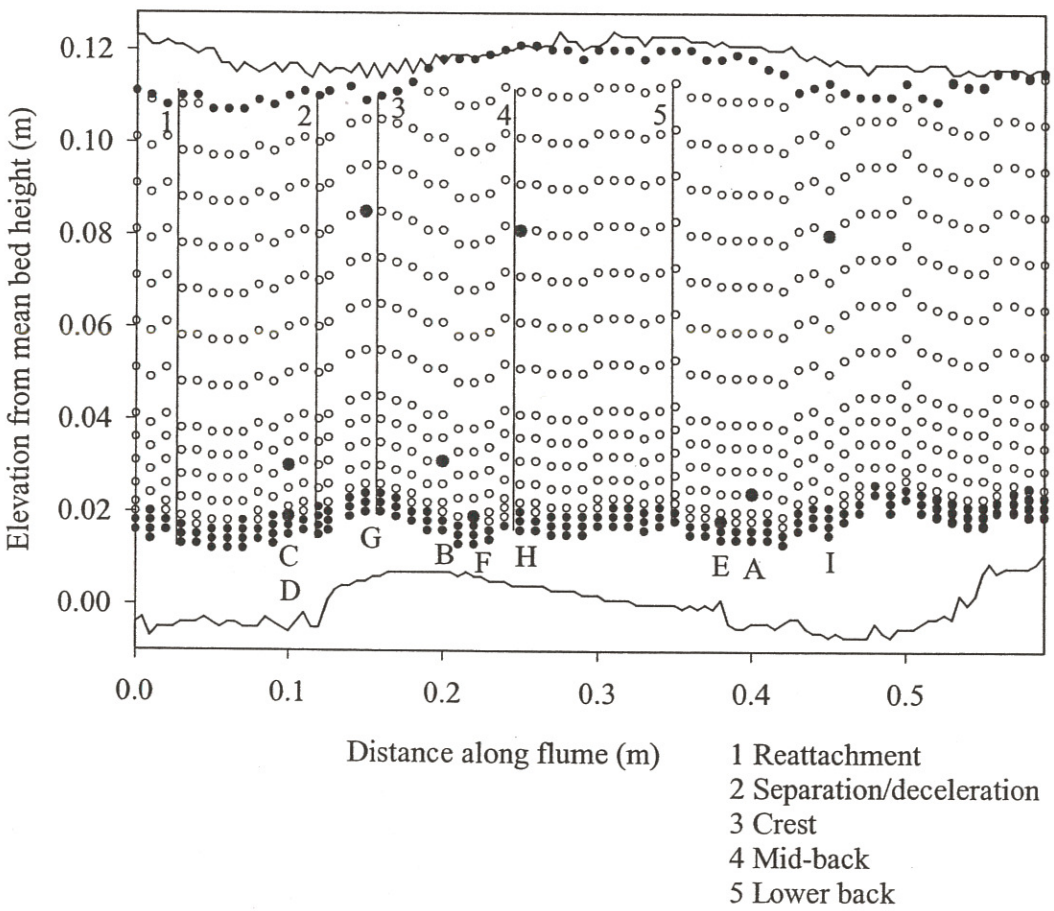

The time-averaged downstream and vertical velocities were determined using Equations 4.1 and 4.2 respectively. The velocity biasing effect was corrected for using the transit-time weighting technique (Equation 4.3; Hosel and Rodi, 1977; McLaughlin and Tiederman, 1973).

$$\overline{u} = \sum_{i=1}^{n} \eta_i u_i \tag{4.1}$$

$$\overline{v} = \sum_{i=1}^{n} \eta_i v_i \tag{4.2}$$

$$\eta = \frac{t_i}{\sum_{i=1}^{n} t_i} \tag{4.3}$$

where $\overline{u}$ and $\overline{v}$ are the time averaged downstream and vertical velocities respectively, n is the number of observations, u_i and v_i are the instantaneous downstream and vertical velocities, η is the transit time weighting and t_i is the transit time of the i'th particle passing the LDA measuring volume. The depth averaged downstream velocity (U), the root-mean-square of the downstream ($rmsu'$) and vertical ($rmsv'$) velocity components are calculated from Equations 4.4, 4.5 and 4.6 respectively.

$$U = \frac{1}{d} \int_0^d \overline{u} \partial y \tag{4.4}$$

$$rmsu' = \left[\sum_{i=1}^{n} \eta_i (u_i - \overline{u})^2 \right]^{0.5} \tag{4.5}$$

$$rmsv' = \left[\sum_{i=1}^{n} \eta_i (v_i - \overline{v})^2 \right]^{0.5} \tag{4.6}$$

where d is mean flow depth and the instantaneous downstream and vertical velocity fluctuations from the mean are represented by $u' = u_i - \overline{u}$ and $v' = v_i - \overline{v}$. The skewness of the downstream and vertical velocity distributions (u_{skew}, v_{skew}) were evaluated using:

$$u_{skew} = \sum_{i=1}^{n} \eta_i \left[\frac{(u_i - \overline{u})}{rmsu'} \right]^3 \tag{4.7}$$

$$v_{skew} = \sum_{i=1}^{n} \eta_i \left[\frac{(v_i - \overline{v})}{rmsv'} \right]^3 \tag{4.8}$$

Reynolds shear stress (τ_R) was calculated by

$$\overline{u'v'} = \sum_{i=1}^{n} \eta_i (u_i - \overline{u})(v_i - \overline{v}) \tag{4.9}$$

$$\tau_R = -\rho \overline{u'v'} \tag{4.10}$$

where ρ is fluid density. In order to estimate the boundary Reynolds shear stress (τ_{R0}), at-a-point Reynolds stresses were plotted against y/d. A least squares regression of the upper linear section of the Reynolds stress

4.18 rather than 4.16, the law-of-the-wall is able to maintain the same form but potentially be applicable throughout the whole flow profile since the flow depth is incorporated (Nezu and Rodi, 1986).

$$\frac{l}{d}=\frac{\kappa y}{d}\left(1-\frac{y}{d}\right)^{0.5} \tag{4.18}$$

In order to obtain the velocity-defect law (Equation 4.20), which describes the outer flow field, the maximum velocity ($\overline{u}_{max}$) at the upper limit of the boundary layer (δ, not necessarily where $y = d$) is introduced into the law-of-the-wall (Equation 4.19). The original law-of-the-wall (Equation 4.13) is then subtracted from the modified version (Equation 4.19) resulting in the velocity-defect law (Equation 4.20).

$$\frac{\overline{u}_{\max}}{U_*}=\frac{1}{\kappa}\ln\left(\frac{\delta}{y_0}\right) \tag{4.19}$$

$$\frac{\overline{u}_{\max}-\overline{u}}{U_*}=\frac{1}{\kappa}\ln\left(\frac{\delta}{y}\right)=-\frac{1}{\kappa}\ln\left(\frac{y}{\delta}\right) \tag{4.20}$$

Coles (1956) proposed a wake coefficient (Π) to correct for the under-prediction of velocity by the law-of-the-wall and velocity-defect law in the outer region of turbulent boundary layers (i.e. $y/d > 0.2$). The wake coefficient is an empirical correction function, which represents the various influences (e.g. secondary circulation and turbulent wakes) on the velocity distribution throughout the flow depth. Equation 4.20 is therefore surpassed by the velocity defect-wake law (Equation 4.21), which was empirically derived for smooth turbulent flows, not for flows which are hydraulically rough or have bedload, suspended sediment or bedforms. The velocity defect-wake law can be used to obtain the velocity at the free surface where measurements are difficult.

$$\frac{\overline{u}_{\max}-\overline{u}}{U_*}=-\frac{1}{\kappa}\ln\left(\frac{y}{\delta}\right)+\frac{2\Pi}{\kappa}\cos^2\left(\frac{\pi}{2}\frac{y}{\delta}\right) \tag{4.21}$$

In the near-surface region, secondary currents can negate the wake effect, and consequently the law-of-the-wall and the velocity-defect law may apply to the whole flow depth (Ferro and Baiamonte, 1994). The ability to assess the validity of the law-of-the-wall and the velocity defect-wake law is dependent on the quality of the data collected. Ideally, a non-intrusive method, with a high temporal and spatial resolution should be employed e.g. LDA used in the present experiments. For example, precise measurement of $\overline{u}$ and y in the wall region ($y/d \leq 0.2$) and accurate determination of U_* are necessary for evaluating κ. Furthermore, the flow should be as close to a uniform condition as possible (i.e. in the test section), and the channel aspect ratio should be as large as is feasible to avoid the influence of secondary flows. Non-uniform flow and secondary currents negatively impact on the shape of vertical profiles of time averaged velocity parameters. Consequently, comparisons between the laws and experimental data are confined to the region below the downstream velocity maximum at $y = \delta$.

Song and Graf (1994) employ a pressure-gradient parameter, β, defined as

$$\beta = \frac{d}{\tau_0} g\rho\left(-S + \frac{\partial d}{\partial x}\right) \tag{4.22}$$

where, S is the bed slope (assumed to be equal to the water surface slope for the present experiments), and $\frac{\partial d}{\partial x}$ is the longitudinal variation in water depth (assumed here to be equal to 0). The pressure-gradient parameter indicates the degree of uniformity of the flow. When β = -1, the flow is uniform, and decelerating and accelerating flows are distinguished by higher and lower values respectively (Table 4.2). In accelerating flows, the velocity maximum is below the water surface, while it coincides with the water surface during decelerating flow conditions. In uniform flow at-a-point vertical velocities are close to zero, with the depth average value equalling zero. The Reynolds number ($Re = Ud\rho/\nu$) of each experimental flow are also listed in Table 4.2, along with estimates of the relative roughness of the runs. Relative roughness was calculated using the average height of the highest bedform population present, and also the equivalent sand roughness, k_s, derived from the law of the wall.

Table 4.2: *The Reynolds number, pressure-gradient parameter and relative roughness for the experimental flows.*

Run	Reynolds number, Re	Presure-gradient, β	Relative roughness (using bedform height)	Relative roughness (using k_s)
Series 1, d = 0.18 m				
A	76947	-1.8	0.011	0.169
B	87509	-1.3	0.017	0.320
C	107965	-1.2	0.039	0.287
D	112298	-1.1	0.052	0.613
E	126596	-1.1	0.063	0.597
F	135842	-1.6	0.079	0.669
G	135860	-1.0	0.074	0.591
H	147500	-1.2	0.085	0.379
Series 2, d = 0.14 m				
I	71421	-0.8	0.036	1.152
J	86579	-1.0	0.085	1.057
K	93421	-1.2	0.073	0.447
L	98404	-1.2	0.070	0.303
M	109737	-1.1	0.072	1.424
N	128632	-1.1	0.057	1.000
Fixed				
F1 (J)	80377	-2.2	0.13	0.588

4.3.2 Mean flow field over a fixed bed

The flow maps presented here (Figure 4.8) are produced by extrapolation between laser measurement points, which formed an extensive grid over the fixed bedforms (Figure 4.4 and 4.6). No measurements were possible very close to the bed (< 10 mm), due to the presence of large clasts which obstructed the laser beams.

ratios of 2 and 2.5 for series 1 and 2 respectively (Nezu *et al.*, 1985). The linear sections of Reynolds shear stress profiles can be projected to the bed in order to determine boundary shear stress and shear velocity (Figure 4.7, Table 4.3), which can then be used to non-dimensionalise flow velocity and turbulence measurements (Lyn, 1993; Nezu and Rodi, 1986). Figure 4.9 illustrates Reynolds shear stress profiles made dimensionless with shear velocity, which demonstrate the close correspondence of the experimental data to the linear decrease in stress away from the bed indicated in Equation 4.11, and verify the use of linear extrapolation of shear stress to the bed.

Figure 4.9: *Examples of Reynolds shear stress profiles normalised by shear velocity against dimensionless flow depth.*

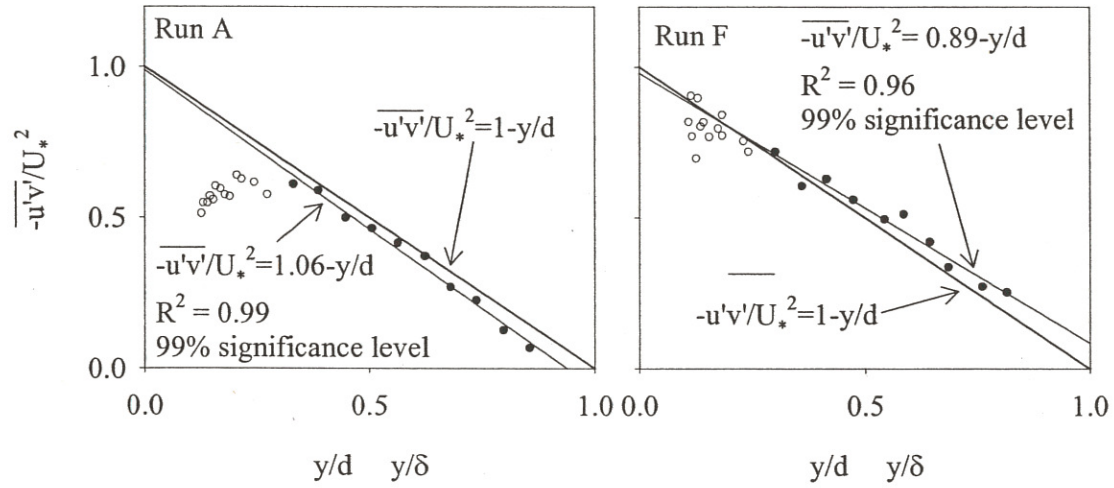

Boundary shear stress and shear velocity is also determined from Equations 4.12 (depth-slope product) and 4.13 (law-of-the-wall). With the exceptions of the fixed bedload sheet, and mobile bed runs A and I (i.e. the lowest discharge mobile run at each flow depth), the boundary shear stress determined by the depth-slope product (Equation 4.12) and Reynolds stress projection (Equation 4.11) were within ± 30 % of each other (Table 4.3). However, the law-of-the-wall (Equation 4.13) gave erroneous results due to the large roughness elements in the region of the flow closest to the bed. The wakes associated with these coarse particles and the bed relief destroy the logarithmic velocity profile inherent in the assumptions of the law-of-the-wall and characteristic of flow over a smooth boundary. The percentage errors for the estimates of boundary shear stress from the law-of-the-wall ranged from ± 17 to ± 171 %, with an average of ± 67 %, while the minimum, maximum and mean percentage errors for shear velocity were ± 8, ± 85, ± 33 % respectively at a 95 % confidence level using the error determination method of Wilkinson (1984). Robert *et al.* (1992) note that the mean percentage errors for their shear velocity estimates are ± 13 %, with the largest errors being ± 61 %. The percentage error for bed shear stress is twice that for shear velocity when derived from the law-of-the-wall, and the accuracy of both depends on the number of measurements employed in the regression (Biron *et al.*, 1998; Wilkinson, 1984). The bed shear stresses derived from Reynolds stress measurements were compared for mobile runs with similar discharges (i.e. C and D, F and G, and J and K), and found to agree

4.3.4 Comparison of vertical profiles of time-averaged downstream velocity with the law-of-the-wall and the velocity defect-wake law

Comparisons of the vertical profiles of time-averaged downstream velocity with the law-of-the-wall were conducted by applying a least squares linear regression between $\overline{u}$ and $\ln y$, where y is the independent variable (Bergeron and Abrahams, 1992; Figure 4.10a). κ and y_0 can then be derived (Equations 4.23 and 4.24) using the slope ($\partial u / \partial \ln(y)$) and intercept ($C$) of the regression, and U_* deduced from the projection of Reynolds stress to the bed (Table 4.3).

$$\kappa = \frac{U_*}{\partial u / \partial \ln(y)} \tag{4.23}$$

$$y_0 = \exp\left(\frac{-C}{\partial u / \partial \ln(y)}\right) \tag{4.24}$$

However, the estimates of y_0 using the law-of-the-wall in the present experiments have a minimum, maximum and mean percentage error of ± 74, ± 817 and ± 252 % at a 95% confidence level. Bennett and Bridge (1995) state a percentage error of ± 100 % for their derivations of y_0, Wilkinson (1984) records an error of ± 77 % while Robert *et al.* (1992) note an average error of ± 35 %.

κ can also be evaluated from the velocity defect-wake law (Equation 4.21), and is equal to the value derived using the law-of-the-wall when the shear velocity estimated from the Reynolds stress projections is employed. Both κ and the Π coefficient are deduced from the velocity defect-wake law (Equations 4.25 and 4.26, and Figure 4.10c) using the slope $\left(\partial\left(\frac{\overline{u}_{\max} - \overline{u}}{U_*}\right) \Big/ \partial \ln\left(\frac{y}{d}\right)\right)$ and intercept (C) of the least squares linear regression of $\frac{\overline{u}_{max} - \overline{u}}{U_*}$ against $\ln\left(\frac{y}{d}\right)$, with $\frac{y}{d}$ as the independent variable.

$$\kappa = -\frac{1}{\partial\left(\frac{\overline{u}_{\max} - \overline{u}}{U_*}\right) \Big/ \partial \ln\left(\frac{y}{d}\right)} \tag{4.25}$$

$$\Pi = \frac{\kappa C}{2} \tag{4.26}$$

Calculated values of κ, y_0 and Π are listed in Table 4.4.

4.3.4.1 The present experimental values of κ, y_0 and k_s over a mobile bed

In the spatially-averaged case, κ values ranged from 0.144 to 0.363 in the wall region ($y/\delta \leq 0.2$), and are much reduced from the clear water value of 0.41. When derived over the whole of the boundary layer the κ

Figure 4.10: *Examples of the application of the law-of-the-wall and velocity defect-wake law using linear least squares regression.*

a) Law-of-the-wall.

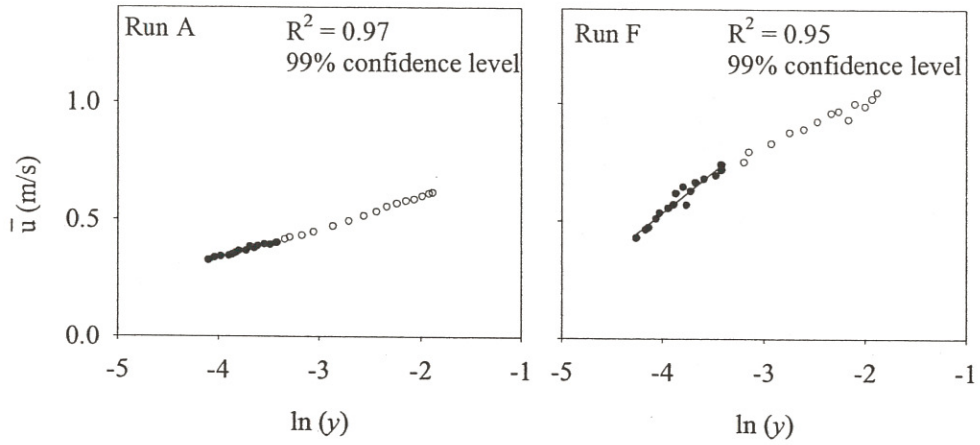

b) Law-of-the-wall shown in dimensionless form.

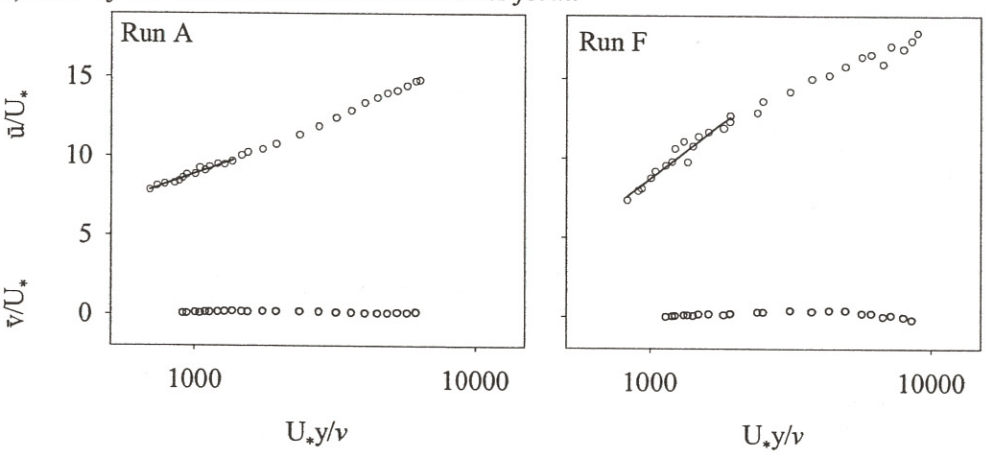

c) Velocity defect-wake law.

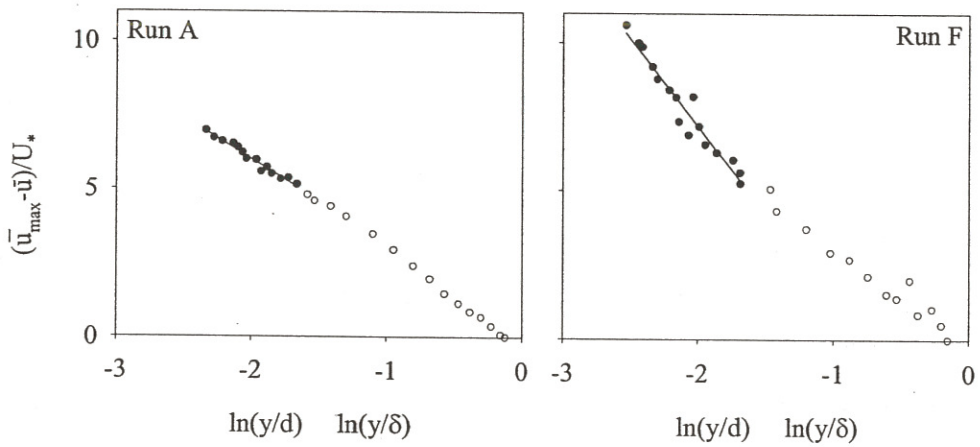

The wake coefficient ranged from –0.423 to 0.096 when derived for $y/\delta \leq 0.2$ with spatially-averaged velocities over a mobile bed. Over the whole of the boundary layer, the derived values extend over a smaller range from –0.095 to 0.016. For specific bedform regions noted in Table 4.4 over a mobile bed, Π values derived from the wall region ($y/\delta \leq 0.2$) and entire boundary layer ($y/\delta > 0.2$) extend from -0.539 to 0.011 and -0.142 to 0.037 respectively. In the fixed bed runs, Π values derived from the wall region and complete boundary layer range from –0.616 to 0.240 and –0.156 to 0.036 respectively.

The velocity defect-wake law fits the experimental data well over the whole flow profile when adjusted values for κ and Π are used, with R^2 values above 0.93 at the 99% significance level (Figure 4.10c). When the law-of-the-wall is applied in the lower 20 % of the flow, R^2 values range from 0.530 to 0.995 (Figure 4.10a). The greater range of R^2 values may be due to the lower number of measurements included in the regression compared with the velocity defect-wake law over the whole flow depth. Furthermore, there is a tendency for greater data scatter near the bed, despite more intensive velocity measurements in this region.

4.4 Discussion

4.4.1 Boundary shear stress determination

Bed shear stress values calculated from Reynolds stress projections and the depth-slope product agreed within 30 %. However, the law-of-the-wall was not successful in predicting accurate boundary shear stresses, except when the discharge was below 0.037 $m^3 s^{-1}$ under the higher flow conditions (Figure 4.11). The shear stresses predicted by the law-of-the-wall show greater deviation from the true values under lower flow conditions, causing the relative roughness to be increased, which is in great contrast to the assumption of a smooth boundary explicit in the derivation of the law-of-the-wall. When the flow was shallower, the boundary shear stress estimated from both Reynolds stress projections and the depth-slope product increased more rapidly with discharge. A similar range of boundary shear stresses (0.42-7.27 Pa) were used in the experiments of Wilcock and McArdell (1993), while Bennett and Bridge (1995) report values below 4 Pa. The depth-slope product predicted similar bed shear stresses for the fixed and mobile bedload sheets, of 2.90 and 2.89 Pa respectively. However, the values obtained from Reynolds stress projections differed substantially, e.g. 1.53 and 3.37 Pa for the fixed and mobile example respectively. Although the estimates of boundary shear stress from the law-of-the-wall concur for the fixed and mobile bedload sheet (15.24 and 16.21 Pa respectively), these predictions are much greater than those derived from the depth-slope product and the projection of Reynolds stresses. The boundary shear stress determined from projections of Reynolds stress to the bed is reduced for the fixed bedload sheet due to lower flow resistance resulting from the absence of bedload (Wiberg and Rubin, 1989) and lower porosity of the fixed bedforms (Mendoza and Zhou, 1992).

Figure 4.12: Spatial variations in time-averaged flow velocities, a) Run J, bedload sheet, b) Run F, low-relief bed wave, c) Fixed 1, bedload sheet and d) Fixed 2, low-relief bed wave. SA represents the spatial average of the time-averaged downstream velocity.

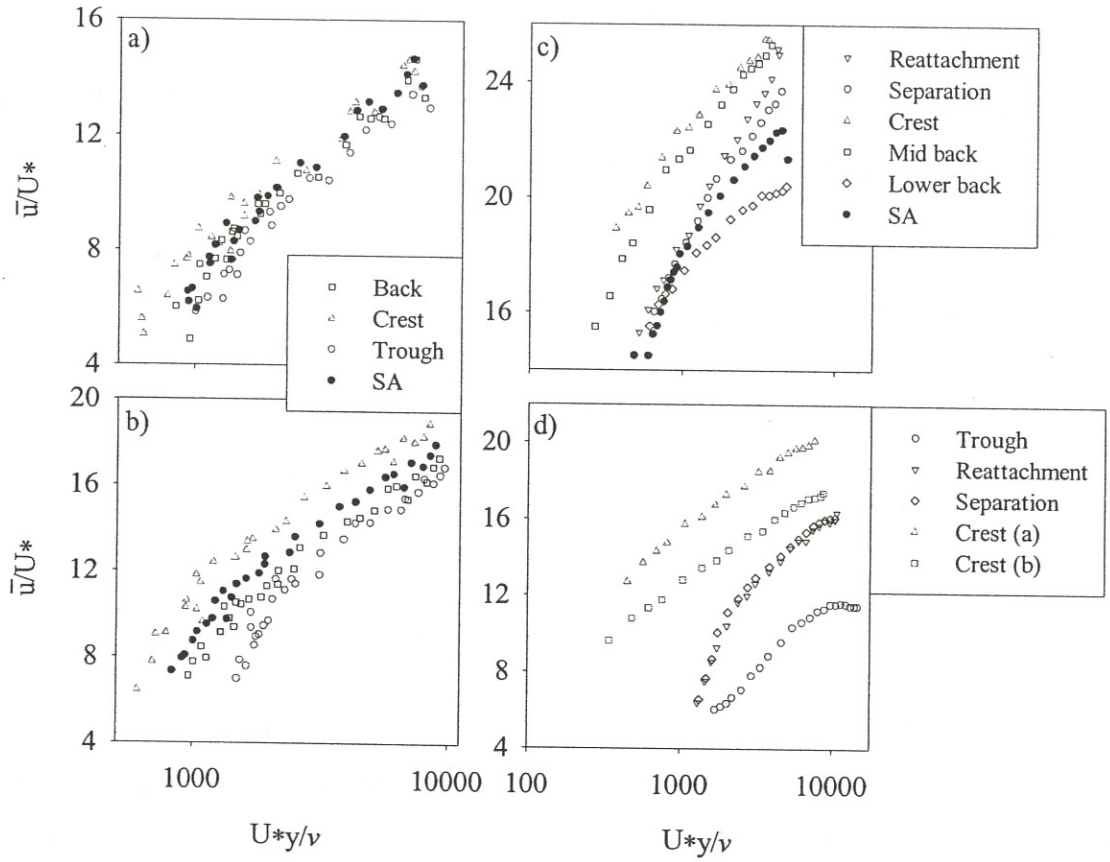

***Table 4.5**: Bed shear stress (Pa) over mobile and fixed bedforms derived from the projection of Reynolds stress to the bed.*

Bedform region/point	Bedload sheets	Low-relief bed waves
	Mobile bed cases	
Back	3.52	3.65
Crest	3.42	3.18
Trough	3.71	3.78
	Fixed bed case	
Reattachment	1.48	5.22
Separation	1.57	5.19
Crest	1.30	3.83-4.79
Mid-back	1.12	
Lower back	1.69	
Trough		7.13

4.4.3 Comparison of the mean flow field over bedforms

The mean flow field over dunes and ripples have previously been mapped (Bennett and Best, 1995, Figure 5 p. 502; Bennett and Best, 1996, Figure 15.2 p. 291), and are compared in Table 4.6 with the present

Figure 4.13: *Comparison of selected profiles of normalised downstream and vertical velocity over bedload sheets, low-relief bed waves and dunes (Bennett and Best (1995)). Box A highlights increases in vertical velocity near the water surface.*

a) Low-relief bed wave (F2, circles) compared with a fixed dune (squares).

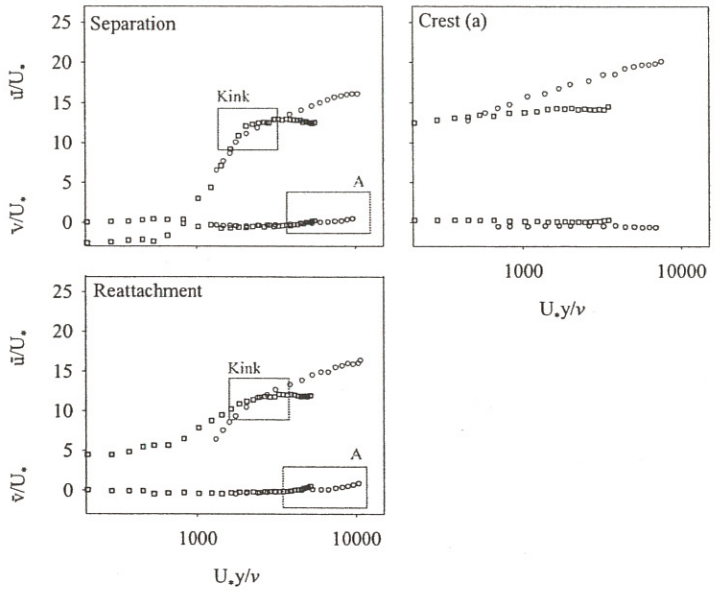

b) Fixed bedload sheet (F1, circles) compared with a fixed dune (squares).

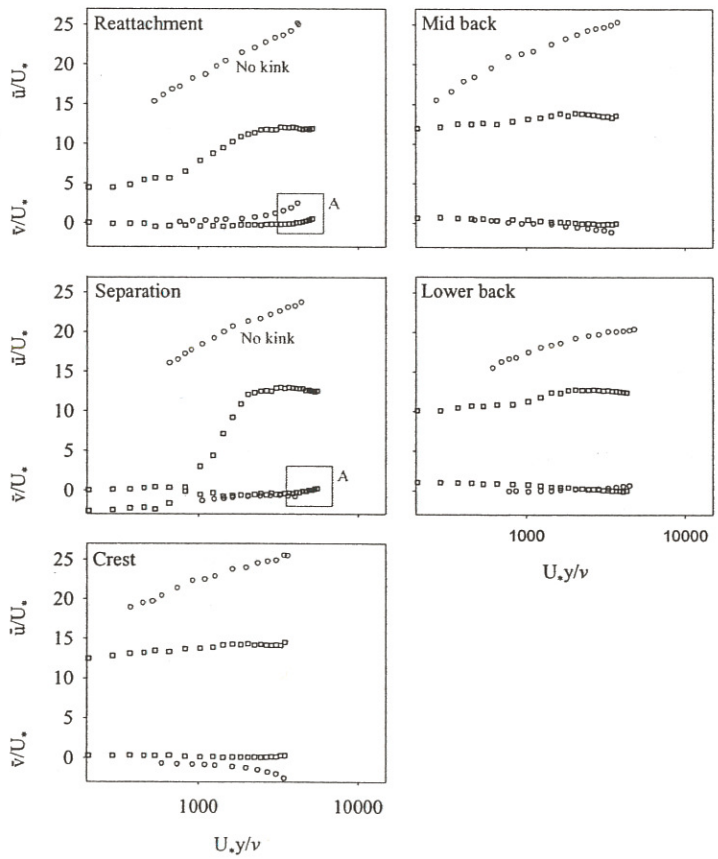

can be attributed to form drag at bankfull conditions. Form drag is a function of bedform height (h), steepness (h/l; where l is bedform length) and bedform shape (β; the fraction of a rectangle, equivalent in height and length to the bedform, which is occupied by the bedform). In the present experiments, the shape factor (β) was determined by tracing and superimposing 20 bedforms of each type, and calculating β for the smallest and largest resulting feature. The shape factor ranged from 0.41-0.80, and average values of 0.51, 0.50, 0.61 and 0.70 were obtained for ripples, bedload sheets, low-relief bed waves for series 1 and low-relief bed waves for series 2 respectively. Roden (1998) demonstrates that the shape factor varies with flow depth and does not adequately describe whether flow separation will occur. The present experimental data has been employed in the following equations (4.30-34), all of which include bedform related parameters, in order to determine the form friction factor (f'') in conjunction with equations 4.27-29. The average dimensions of the highest order bedform group (transverse to flow) of each experimental run are used, with ripples being the lowest order, bedload sheets intermediate, and low-relief bed waves the highest. The equation of van Rijn (1984, 1993) requires the average dimensions of the two highest bedform groups present in a given experimental run.

Vanoni and Hwang (1967)
Ripples and dunes

$$(f'')^{-0.5} = 3.5\log\left(\frac{d}{rh}\right) - 2.3 \qquad (4.30)$$

Engelund (1977)
Dunes

$$f'' = 10\frac{h^2}{dl}\left(r^{-2.5h/d}\right) \qquad (4.31)$$

van Rijn (1984, 1993)
Ripples and dunes

$$\text{Ripples: } k_s'' = 20\gamma_r h\left(\frac{h}{l}\right) \qquad (4.32)$$

$$\text{Dunes: } k_s'' = 1.1\beta h(1-\exp(-25h/l))$$

Karim (1995)
969 flows, sand and gravel rivers and flume data.

$$\frac{f}{f'} = 1.20 + 8.92\left(\frac{h}{d}\right) \qquad (4.33)$$

McLean *et al.* (1999a, b)
Dunes and 2-D bedforms

$$\tau_D = 0.5\rho C_D u_R^2 \frac{h}{l} \qquad (4.34)$$

where, d is flow depth, h is bedform height, l is bedform length, r is the ratio of the lee slope area and the total bedform area (~0.11 for the present experiments), γ_r is the ripple presence factor (1 for ripples alone, 0.7 for superimposed ripples), β is the shape factor, τ_D is form drag, C_D is a drag coefficient (= 0.19) and

bedform length. Lanzoni (2000) notes that the effect of mixture sorting on bedform wavelength is not clear, whereas bedform height is observed to be damped with increasingly strong bimodal mixtures (i.e. indices of bimodality, Section 1.2). The vast majority of the data used to construct the semi-empirical equations listed above is derived from sand sized sediments. The equations of Engelund (1977) and McLean *et al.* (1999a, b) typically produce the lowest estimates of form related friction factor, whilst Vanoni and Hwang (1967) generate the highest. Boxes C and D in Figure 4.14 highlight anomalous values of the Darcy-Weisbach total friction factor due to low and high values of bed shear stress for runs F (series 1) and I (series 2) respectively, which are derived from projections of Reynolds stresses to the bed.

Figure 4.14: *The Darcy-Weisbach friction factor (solid symbols) and estimations of the form related friction factor (white symbols). The anomalous boxed values are discussed in the text.*

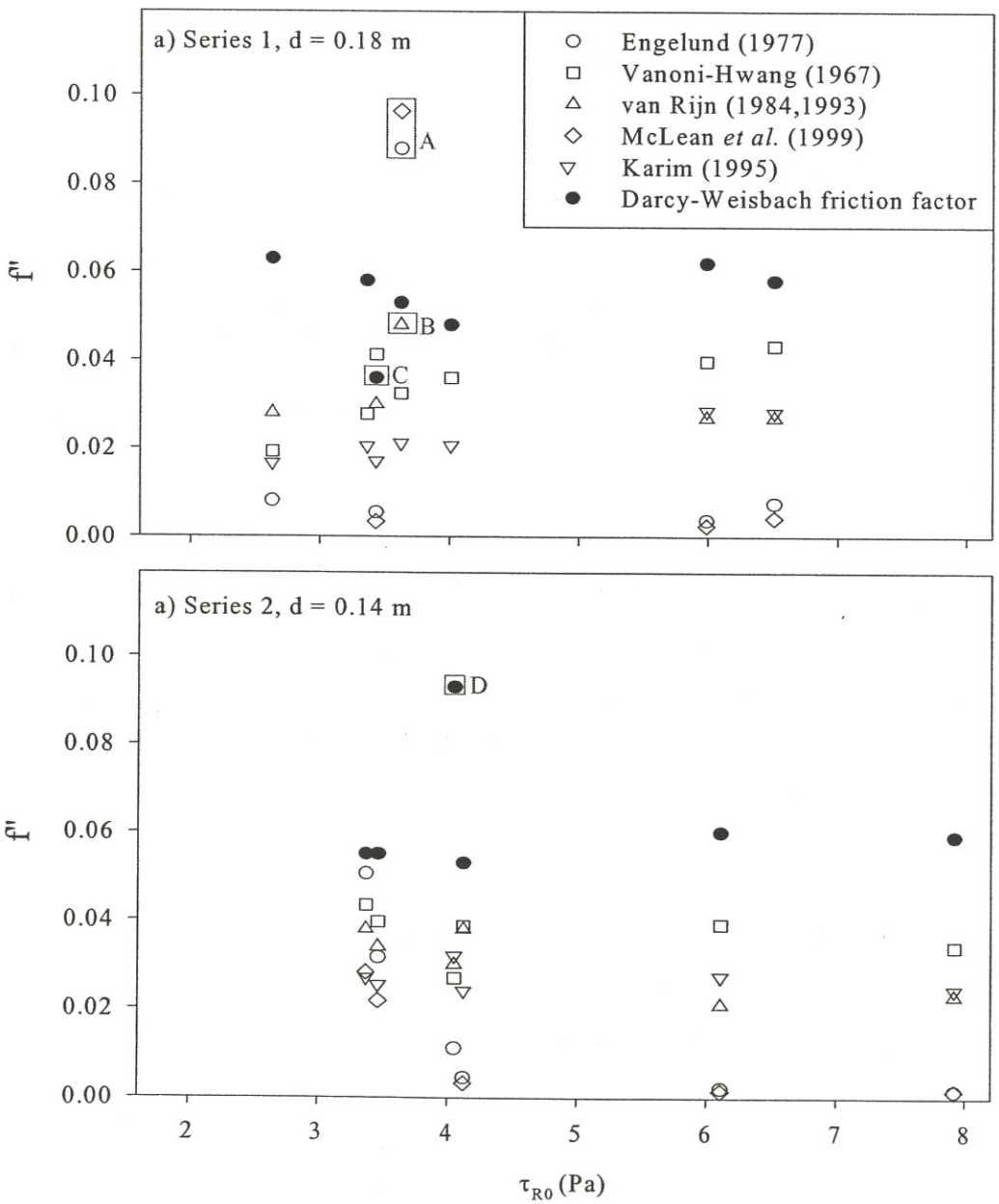

shear stress), although the transition to upper stage plane beds occurs at lower transport rates compared with a sand bed stream. If all the clasts are in motion at some time, the distinction between the material in the bed and the bedload is not critical for calculating roughness (Pitlick, 1992; Whiting and Dietrich, 1990). The model of Wiberg and Smith (1991) indicates that bed roughness is influenced by the degree of sediment sorting, however, this is not confirmed by the analysis of Millar (1999). In his analysis, Millar (1999) considers grain protrusion effects to be a component of form roughness. Conversely, Whiting and Dietrich (1990) and Nikora *et al.* (1998) attribute the effect of prominent clasts to grain roughness. Nikora *et al.* (1998) explain that the effective bed roughness height of a gravel-bed river is characterised by three independent scales e.g. bed elevations are analysed as a three-dimensional random field (i.e. a topographic map of the sediment bed), which varies in the downstream, traverse and vertical directions. No form roughness due to bedforms was observed in the examples studied by Nikora *et al.* (1998). Furthermore, using one characteristic grain size to estimate the effective grain related roughness height provides only a rough alternate to the random field approach, although is much less labour and time intensive. Van Rijn (1993) cautions that roughness predictors do not adequately account for the effects of water temperature, channel pattern and sediment discharge on the resistance to flow provided by the bed. Furthermore, the influence of the grain size distribution on the bed roughness is poorly understood, partly due to the unclear effects of sediment gradation on bedform length (Lanzoni, 2000) and particle protrusion (Millar, 1999), sorting (Wiberg and Smith, 1991) and characteristic size (Sambrook Smith *et al.*, 1997).

4.4.5 Comparison of calculated y_0, k_s, κ, and Π values with previous results

Estimates of zero-velocity roughness height fall within the range deduced in previous work (Table 4.10) despite the large associated errors. The occurrence of errors in the calculations of y_0 and k_s ($k_s = 30.2y_0$) is highlighted by the contrasting values of spatially-averaged k_s shown in Figure 4.15 (Boxes A-C) for similar boundary shear stresses. Values of y_0 and k_s tend to increase at a flow depth of 0.18 m with rising bed shear stress and the growth of bedforms, although this levels off at boundary shear stresses greater than ~ 3.5 Pa (Figure 4.15a). However, no obvious trend of y_0 and k_s with bed shear stress is apparent at a flow depth of 0.14 m. The value of k_s for the fixed bedload sheet (0.070 m) is more similar to the value obtained in run K (0.067 m, exhibits bedload sheets) than run J (0.149 m), which is the equivalent mobile run (Figure 4.15b). However, the bed shear stress of runs J and K are similar (3.37 and 3.46 Pa respectively), but greater than that of the fixed bedload sheet (1.53 Pa) which offers less resistance to the flow due to the absence of bedload. It is therefore not possible to assess the impact of fixing the bed on the spatially-averaged values of y_0 and k_s, especially in light of the substantial percentage errors associated with their determination.

The greatest k_s values calculated in the present study are ten times larger than the coarsest grains found in the bulk sediment mixture. Nezu and Nakagawa (1993) highlight that it is difficult to determine k_s over irregular surfaces, since when applying a logarithmic velocity profile to a rough bed, it is problematic to identify the position of zero velocity, which influences the values of y_0, k_s and U_* (Nezu and Nakagawa, 1993; Smart, 1999).

Values of y_0 and k_s are greatest in the separation region of both the fixed bedload sheet (Figure 4.16) and low-relief bed wave (Figure 4.17), and at a minimum over the crest. Minimum values of y_0 and k_s in the crestal region were confirmed by the results over the mobile bedload sheets and low-relief bed waves (Table 4.4). High values of y_0 were noted by Carling *et al.* (2000b) at the crest and in the lee of sand dunes. They found that the confidence limits for y_0 were especially broad over the crest and stoss due to topographic accelerations and a poorer fit of the law-of-the wall to the velocity profiles. Furthermore, non-logarithmic velocity profiles were associated with the lee of the sand dunes and superimposed features. The latter increases the roughness length along the stoss and crest of the host bedform. Robert *et al.* (1992) observed an increase in roughness height with the transition to greater bed roughness. Indeed, in the present experiments, y_0 and k_s appear to increase immediately downstream of the bedform crest due to flow expansion and a rapid transition to greater surface roughness.

***Figure 4.16**: The distribution of time-averaged y_0 and k_s over a fixed bedload sheet.*

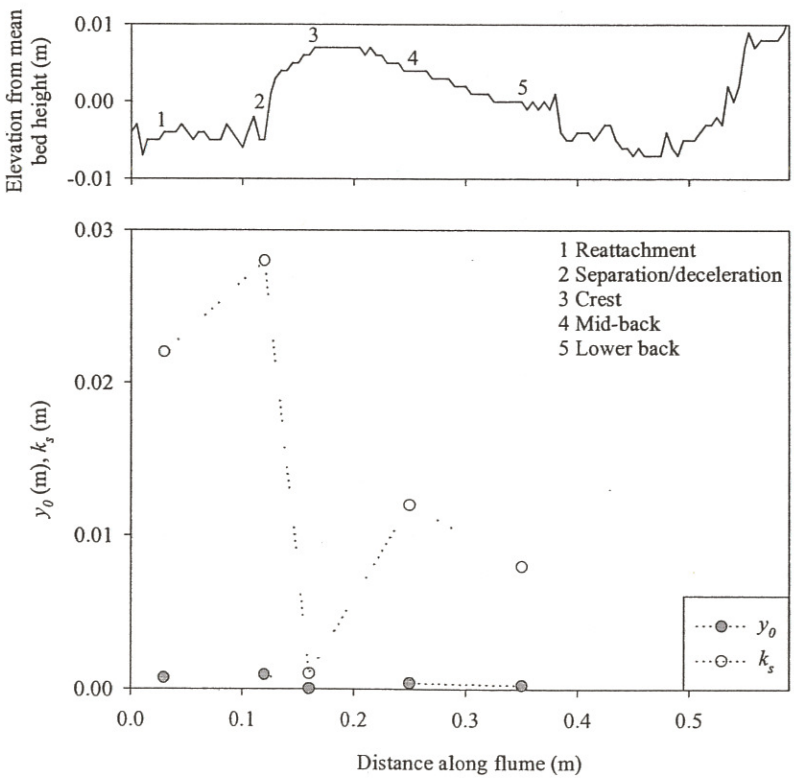

present experimental sediment, the mixture would be expected to be relatively porous compared with a uniform mixture, and therefore reduced κ values would be anticipated. However the porosity will vary over the length of a bedform due to grain sorting and alignment. Furthermore, grain sorting will cause transitions in bed roughness, which Antonia and Luxton (1972) believe causes the law of the wall to be invalid, a reduction in the associated constant of integration, and deviations from a value of 0.41 for κ. Values for κ also tend to be lower when predicted using only the bottom 20% of the flow rather than the whole flow depth in the present experiments, since the sediment boundary has greatest influence in this region of the flow. The range of κ values calculated over the fixed beds is greater than over the mobile beds due to the inclusion of a greater proportion of bed specific values in Figure 4.18, which exhibit greater variation than spatially-averaged results that are more common for the mobile bed condition.

Figure 4.18: *Cumulative frequency of the wake coefficient and von Kármán's constant derived for mobile and fixed bed experimental runs from spatio-temporally-averaged downstream velocity in both the bottom 20 % of the flow depth ($y \leq 0.2d$) and the whole flow depth ($y \leq d$).*

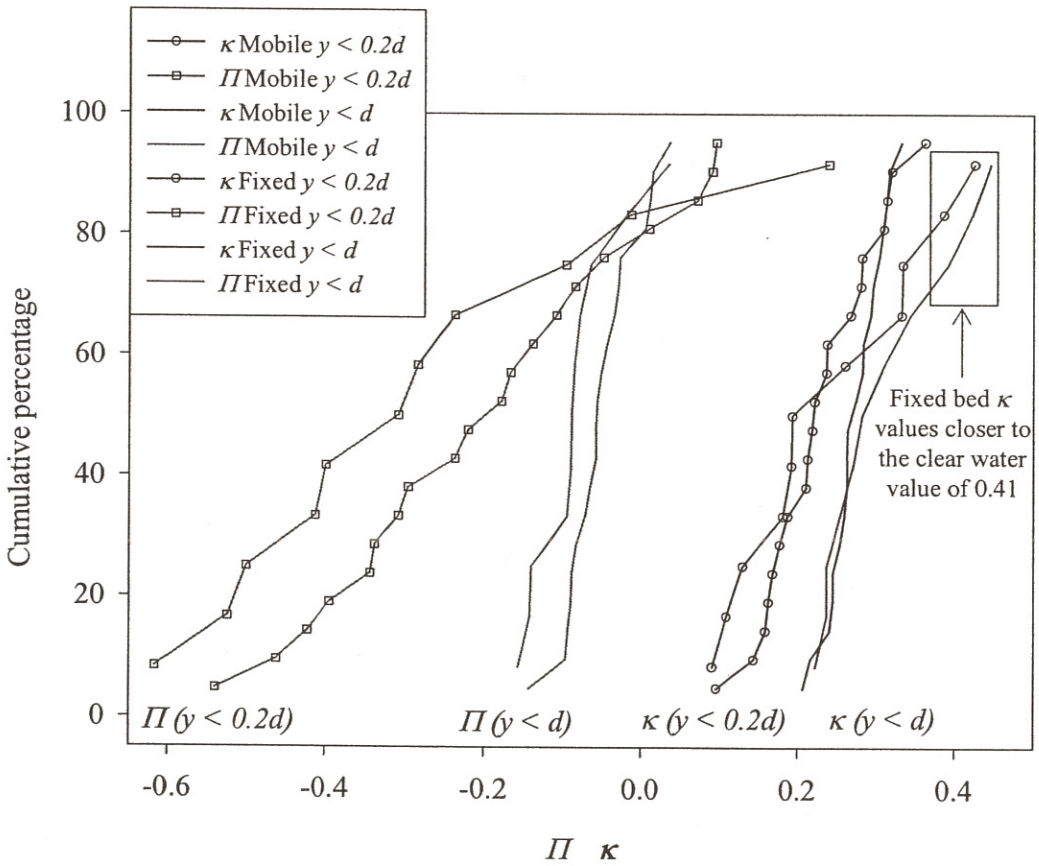

Previous work over a variety of bed conditions (Table 4.11), typically report positive Π values, which are found to increase with greater suspended sediment concentrations over flat beds. However, the present experimental data and that of Bennett *et al.* (1998) predominantly find negative Π values (Figure 4.18). Since Π is an empirical correction function, representing various influences on velocity throughout the flow depth, the negative values reported here may occur for several reasons e.g. sediment transport and a velocity

***Figure 4.19**: Values of κ and Π determined over a range of bed shear stresses.*

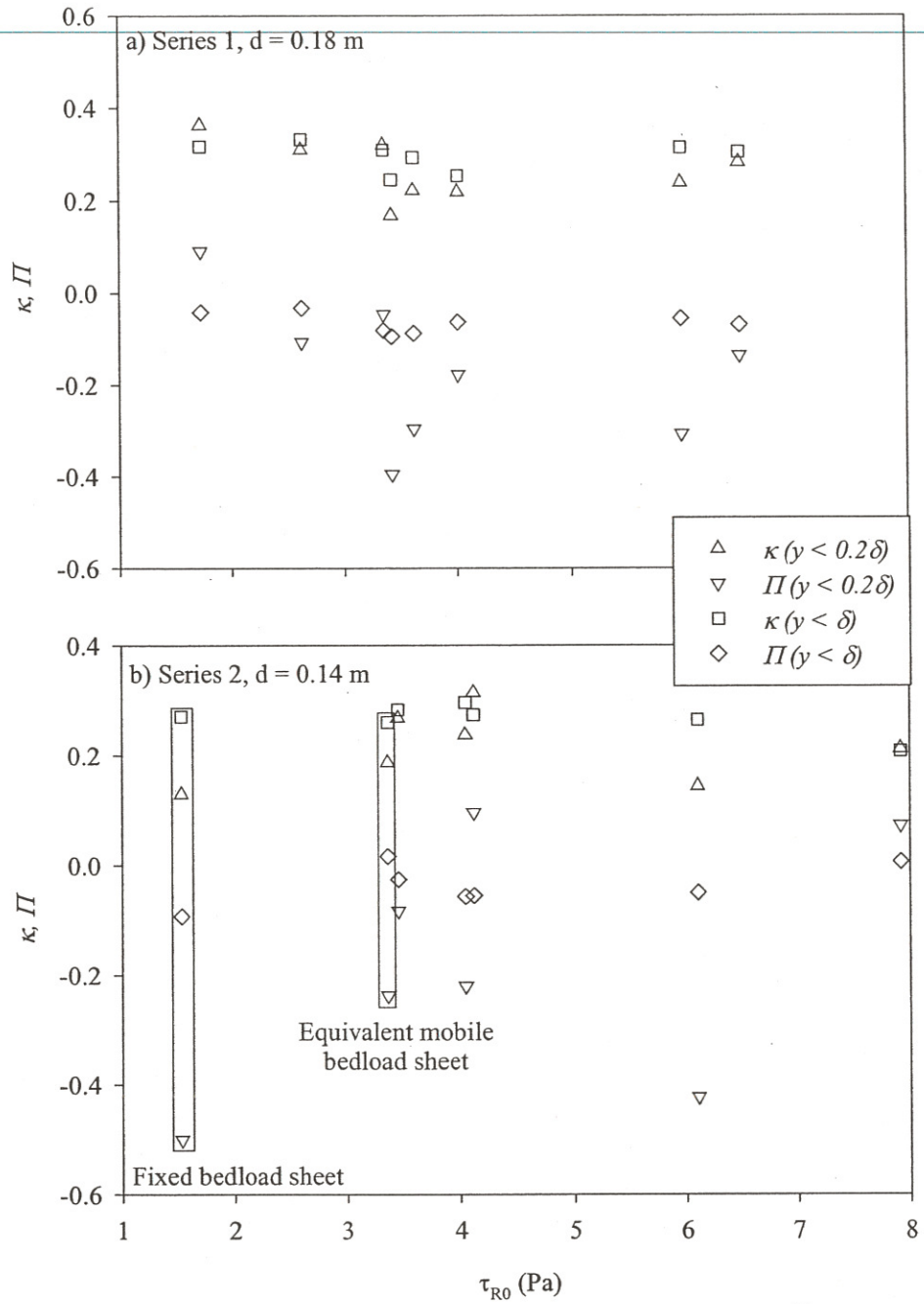

The values of κ and Π tend to rise over the crest of the fixed bedload sheet (Figure 4.20) and low-relief bed wave (Figure 4.21), and diminish immediately downstream with the onset of flow deceleration and expansion. The only exception is the trend of Π calculated over the whole flow depth for the fixed low-relief bed wave, which exhibits slightly raised values downstream of the bedform crest. The slope of the regression used to determine κ and Π $\left(\partial\left(\frac{\overline{u}_{max}-\overline{u}}{U_*}\right)\Big/\partial\ln\left(\frac{y}{d}\right)\right)$ is reduced over the bedform crest compared

Kironoto and Graf (1994) attribute negative wake coefficients to retardation effects, caused by the velocity maxima falling below the water surface, and variations in pressure gradients (i.e. non-uniform flow). When Cardoso *et al.* (1989; aspect ratio ranged from 4.7-7.4) determined wake coefficients over smooth beds using just the velocity profile below the maximum downstream velocity, negative values were obtained. Kironoto and Graf (1994) deduced that $\Pi = 0.88\beta$ when the aspect ratio is 2 (close to the present experimental values). Since all the current experimental values of β are negative, Π values would therefore also be anticipated to be negative.

4.4.6 Comparison of spatially-averaged velocity data with the law-of-the-wall

In order to compare the present spatially-averaged velocity measurements with the law-of-the-wall, the data is plotted in non-dimensional form with $\overline{u}/U_*$ against $\frac{U_* y}{\nu}$ (Figure 4.22, where U_* is derived from the projection of Reynolds stress to the bed), in accord with previous studies e.g. Kirkgöz (1989) and Nezu and Rodi (1986). The same linear trend is exhibited by all the spatially-averaged flow data collected over a mobile bed in the present experiments, with an intercept value of –15.22 (Figure 4.22, regression line 3). However, the linear least squares regression lines of LDA measurements taken by Kirkgöz (1989) over smooth (1) and rough (2) surfaces exhibit greater intercept values (5.5 and –0.8 respectively), and therefore plot above the present mobile bed data, as illustrated in Figure 4.22. The current experimental data plot below Kirkgöz's (1989) empirical equations due to the fact that additional roughness is introduced by the presence of both mobile sediment and bedforms. Kirkgöz's (1989) LDA data was collected in a laboratory flume with similar dimensions to that employed in the present experiments (i.e. 12 m long and 0.3 m wide), in which the 'rough' surfaces consisted of a single layer of fixed aggregate (i.e. the D_{90} of the rough surfaces were 2.36, 5, 10 and 20 mm), and consequently these are most similar to the fixed bed cases considered in the present experiments where bedload is absent. The spatially-averaged flow over the fixed bedload sheet plots between the two curves proposed by Kirkgöz (1989) for smooth and rough beds (Figure 4.22). The fixed bedload sheet data does not concur with Kirkgöz's (1989) experimentally derived curve for rough beds since he did not consider the influence of bedforms, grain sorting and mixture bimodality on the velocity distribution.

Nezu and Rodi (1986) due to the relatively high shear velocities experienced (up to 0.0890 m s^{-1} in the present experiments, 0.0466 m s^{-1} in the study of Nezu and Rodi (1986) and 0.0382 m s^{-1} for Kirkgöz (1989)), despite intensive velocity measurements near the bed. Greater values of shear velocity are also associated with sediment sorting and the development of bedforms, which can distort velocity profiles from a logarithmic shape. The present experimental data does not include values of $\frac{U_* y}{\nu}$ below approximately 500 (Figure 4.22), whereas the linear region conforming to the law-of-the-wall in the work of Nezu and Rodi (1986) and Kirkgöz (1989) falls below this value (Figures 4.23a-c). Divergence from the law-of-the-wall, resulting in a steeper slope, occurs at around $\frac{U_* y}{\nu} \geq 500$ i.e. the range of the present experiments. Since κ is inversely related to the slope, the values of κ derived from the law-of-the-wall in the present experiments are reduced compared with the standard value of 0.41 (Nezu and Nakagawa, 1993).

Figure 4.23: *The application of the law-of-the-wall to velocity profiles.*

a) Experimental data of Nezu and Rodi (1986) and Steffler at al. (1985), $y^+ = U_* y / \nu$.

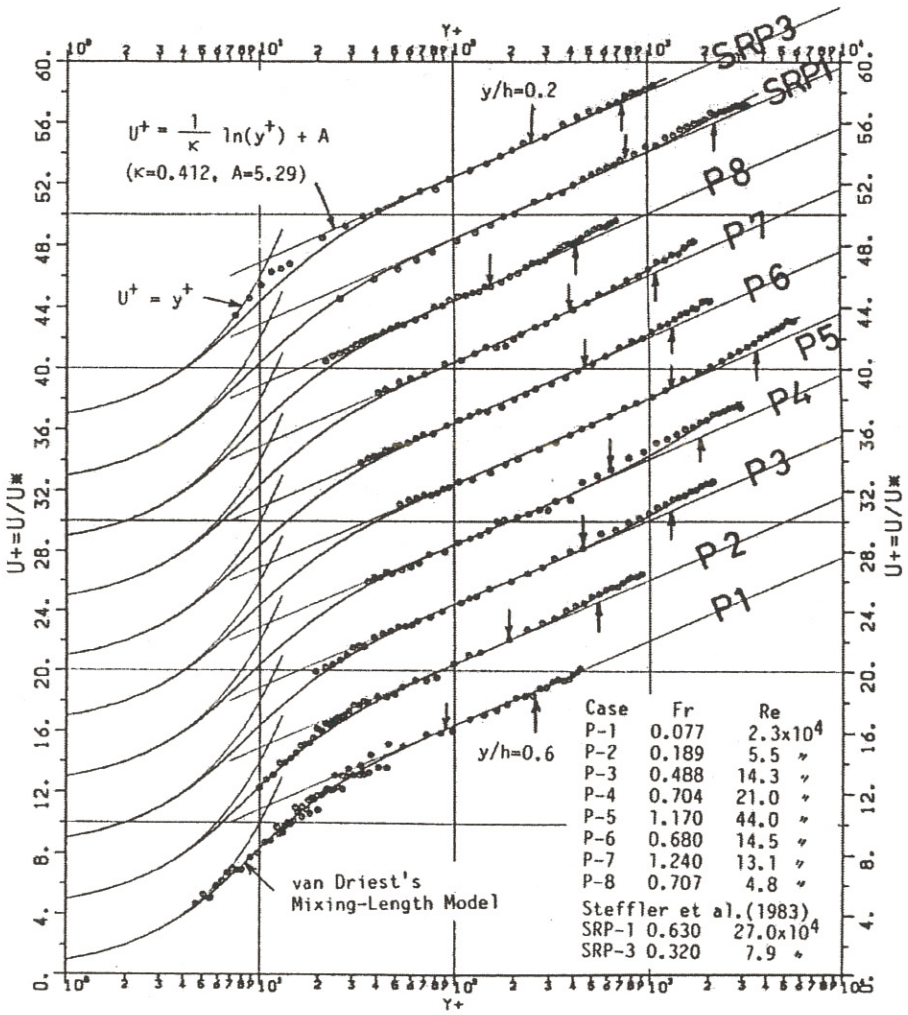

Kirkgöz's (1989) experimental curve for flow over a smooth bed $\left(\frac{\overline{u}}{U_*} = 2.44\ln\left(\frac{U_* y}{\nu}\right) + 5.5\right)$ is in close agreement to that derived empirically by Nezu and Rodi (1986) for flow over a smooth boundary i.e. $\frac{\overline{u}}{U_*} = 2.43\ln\left(\frac{U_* y}{\nu}\right) + 5.29$. Furthermore, visual inspection of the linear least squares regressions in Figure 4.23a and b supports the value of the gradient reported by Kirkgöz (1989) and Nezu and Rodi (1986), which corresponds to the clear water value for κ of 0.41. However, Kirkgöz (1989) assumes that the slope of the linear least squares regression is equivalent for his smooth and rough fixed bed cases, in order for κ to assume a constant value of 0.41. The distribution of measurement points over the rough beds of Kirkgöz (1989) do not appear to follow a linear trend, but instead plot as a curve (Figure 4.23c), shedding doubt on the value for κ employed and the validity of the law-of-the-wall over rough surfaces. Since experimental data diverges from the law-of-the-wall for the values of $\frac{U_* y}{\nu}$ obtained in the present experiments, resulting in erroneous results, the current experimental data will now be compared with the velocity defect-wake law.

4.4.7 Comparison of spatially-averaged velocity data with the velocity defect-wake law

Spatially-averaged profiles of downstream velocity are plotted in Figure 4.24 and 4.25 ($(\overline{u}_{max} - \overline{u})/U_*$ against $\ln(y/d)$), and follow a linear trend over a smooth boundary but demonstrate considerable scatter over rough beds, preventing the derivation of an empirical description of the velocity distribution above a rough surface (Kirkgöz, 1989). In the experiments of Kirkgöz (1989), the data scatter over the rough beds may be due to the generation of wakes from the coarse roughness elements. Nowell and Church (1979) found that the velocity defect law was not valid in the presence of wake interference flow, and concluded that in gravel-bed rivers the velocity distribution did not correspond to the law-of-the-wall.

Spatially-averaged profiles of downstream velocity for the present experiments (Figure 4.25) show little scatter in the top 60 % of the flow depth i.e. $\ln\left(\frac{y}{d}\right) > -1$. Furthermore, the data conforms with Kirkgöz's (1989) empirical curve (Figure 4.25, curve 1) for smooth beds in this region of the flow column, although the linear least squares regression through the present data set (curve 2) is slightly steeper than curve 1. Due to the inverse relationship of κ with slope, the greater gradient agrees with the reduced κ values calculated for the present experimental data (Table 4.4). The value of the intercept of curve 2 (-0.25) indicates the predominately small and negative nature of the estimates of Π in the present experiments (Table 4.4). There is increased data scatter as the bed is approached in accord with experiments of Kirkgöz (1989; Figure 4.24), due to the influence of the boundary conditions, which vary between the present experimental runs e.g. grain

Figure 4.25: *The velocity defect-wake law for the present data compared with the empirical equation of Kirkgöz for flow over smooth beds.*

1) $\frac{\overline{u}_{max} - \overline{u}}{U_*} = -2.44 \ln\left(\frac{y}{\delta}\right)$ (Kirkgöz, 1989, smooth)

2) $\frac{\overline{u}_{max} - \overline{u}}{U_*} = -3.46 \ln\left(\frac{y}{\delta}\right) - 0.25$ (Present data)

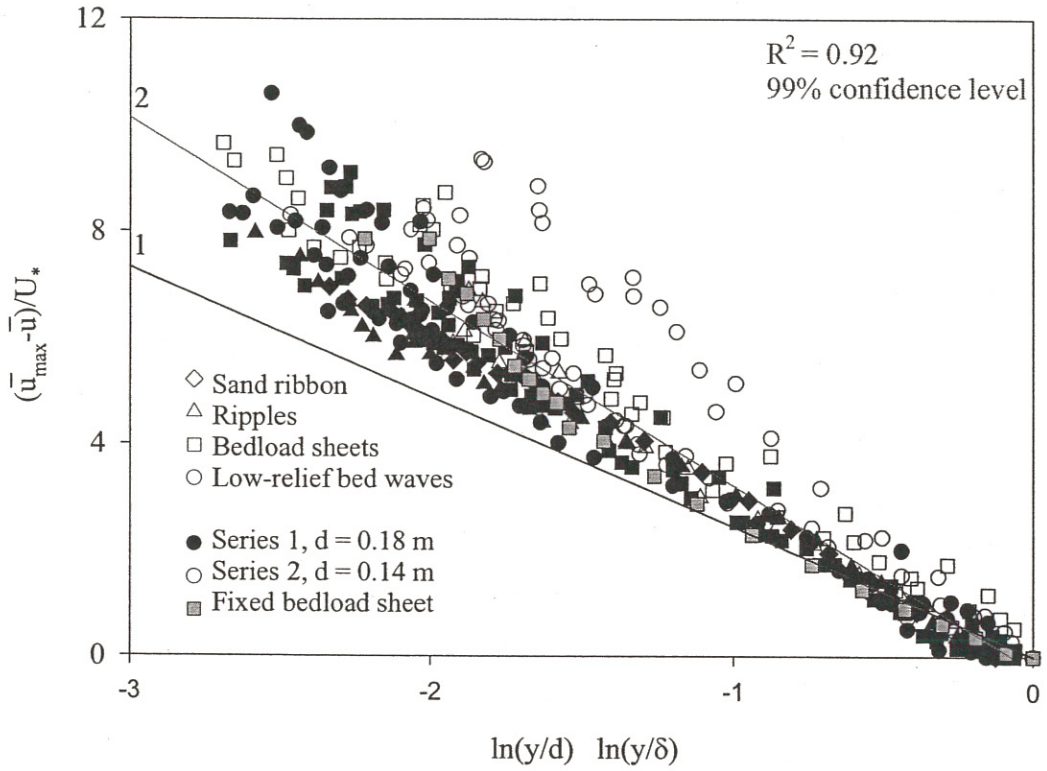

4.4.8 Comparison of time-averaged velocity with theoretical models

Wiberg and Smith (1991) derived a model for the spatially-averaged velocity field over a poorly sorted bed, which accounts for the shear stress attributable to coarse bed particles. Velocity profiles predicted by the model are valid for bed sediment distributions where $D_{84}>2D_{50}$, although mean velocity values can also be calculated for uniform sediment. The present experimental data was used in the model of Wiberg and Smith (1991; Equations 4.35 and 4.36), accounting for the bimodal nature of the sediment mixture. A first approximation of the spatially-averaged velocity profile is expressed by:

$$\tau_D(y) \approx \frac{3}{4}\rho \int_{y_0}^{y_i} u^2 dy (C_D) \sum_{m=i}^{M} \frac{c_m}{D_m} \tag{4.35}$$

$$\frac{\partial u}{\partial y} = \frac{U_*}{L}\left\{\left(1 - \frac{y}{d}\right) - \frac{\tau_D}{\tau_0}\right\}^{0.5} \tag{4.36}$$

Table 4.12: *The percentage difference between the depth-averaged velocity calculated from velocity measurements and the model of Wiberg and Smith (1991).*

Run	Depth-averaged velocity (Percentage difference)
A (Sand ribbon, lowest discharge, d = 0.18 m)	35 %
H (Low-relief bed wave, highest discharge, d = 0.18 m)	47 %
I (Ripples, lowest discharge, d = 0.14 m)	48 %
N (Low-relief bed wave, highest discharge, d = 0.14 m)	53 %

Figure 4.26: *Comparison of the measured and predicted spatially-averaged velocity profile for Run A.*

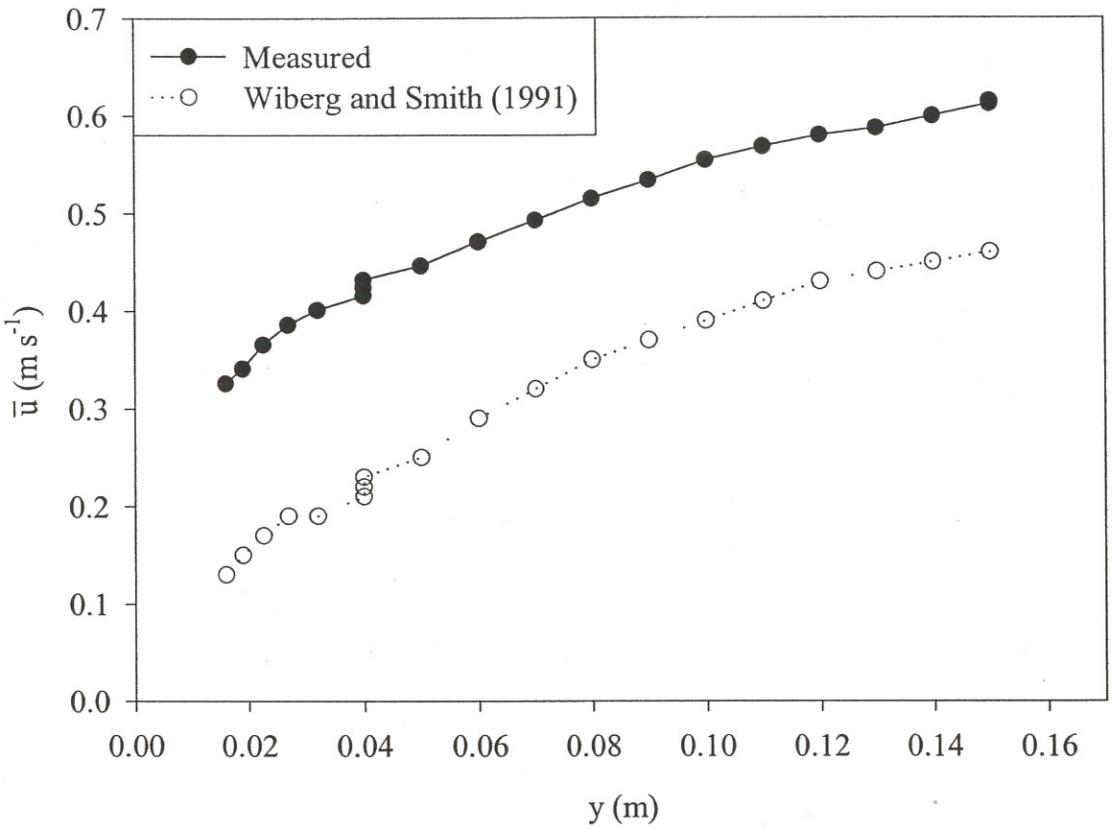

The overall trend of the measured and predicted spatially-averaged velocity profiles can be compared by plotting them non-dimensionally (Figure 4.27). The spatially-averaged velocity profiles predicted by the model of Wiberg and Smith (1991) display a lesser gradient than the experimental data, although the model predictions fall within the range of experimental measurements at a flow depth of 0.14 m when $y/d < 0.4$. The reduced slope of the model predictions indicate that the drag effect of the coarse particles on the flow is overestimated by the model, causing underestimation of the near-bed velocities ($y/d < 0.4$). Consequently, in the outer flow ($y/d > 0.4$) velocity estimates are too high since the model compensates for the erroneous low velocity estimates in the near-bed flow region ($y/d < 0.4$). The experimental values demonstrate greater variability in normalised velocity at a given height above the bed compared with the model predictions due to the range of boundary conditions experienced, whereas the model assumes that each grain size is randomly distributed on the bed (the concentration of the grains in the bulk mixture is used in the model), and does not account for sediment sorting and bedform development. At the lower flow depth the experimental data

developed, larger diameter clasts are present and sediment sorting does not occur in such a regular manner e.g. pebble clusters (Reid and Hassan, 1992) and patches (Laronne *et al.*, 2000).

Figure 4.27: *Comparison of the present data with the model of Wiberg and Smith (1991). Time-averaged velocity, normalised by depth averaged velocity, is plotted against normalised depth. The spatially-averaged velocity profiles of the experimental runs with the highest and lowest discharge at each flow depth are predicted by the model.*

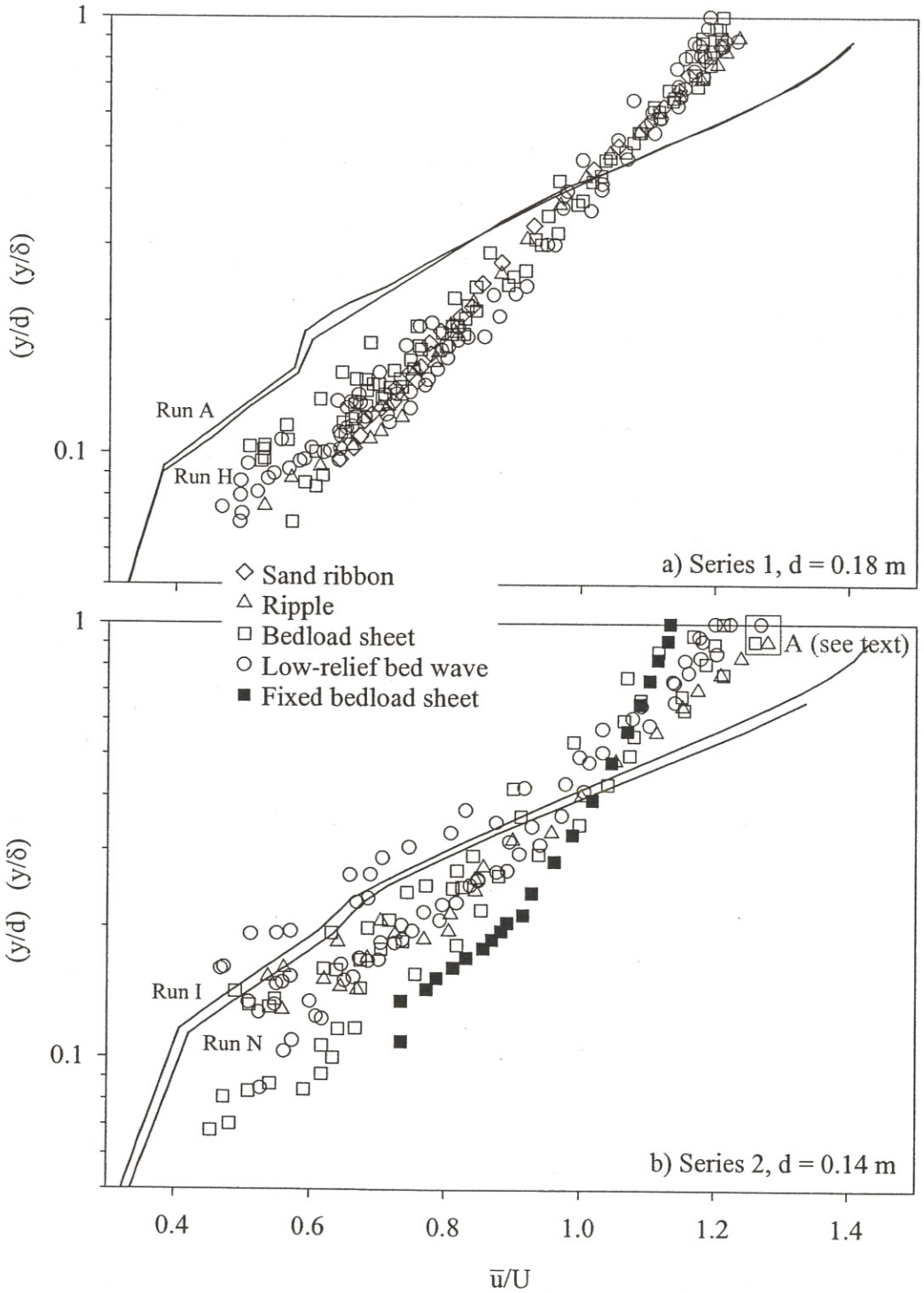

experiments, a linear least squares regression of measurements from the roughness layer ($y < 30$ mm) gives an average value of $C = 5.3$ for the mobile bed experiments, ranging from 4.0 to 9.5 (Table 4.13; red line in Figure 4.30).

Table 4.13: *Values of C derived in the present experiments form the linear flow layer. Modified from Nikora et al. (2001).*

Present experimental run or Reference	*C*
A	4.0
B	4.9
C	4.2
D	5.0
E	6.7
F	9.5
G	6.9
H	5.1
I	5.3
J	6.6
K	6.2
L	6.1
M	8.6
N	5.6
Present experimental average	5.3
Nikitin (1980); glued down gravel particles which had a similar size distribution to natural streams.	5.6
Dittrich and Koll (1997); flume experiments, gravel with narrow size distribution.	5.3
Shimizu *et al.* (1990); glass beads.	5.7-6.0
Nikora *et al.* (2001); fixed spherical segments (Figure 4.29).	7.1
Nikora *et al.* (2001); homogeneous sand roughness	8.5

Nikora *et al.* (2001) state that the outer flow region is described by the velocity defect-wake law (Equation 4.21), while the region $(2-5)\Delta < y < 0.2d$ is characterised by a logarithmic trend (Figure 4.29):

$$\frac{\overline{u}}{U_*} = \frac{1}{\kappa}\ln\left(\frac{y}{\delta}\right) + C \tag{4.39}$$

Figure 4.29: *Comparison of the measured and predicted downstream velocity distribution from Nikora et al. (2001). C is 7.1, κ is 0.4 and δ is 21 mm. Z equals the height above the bed.*

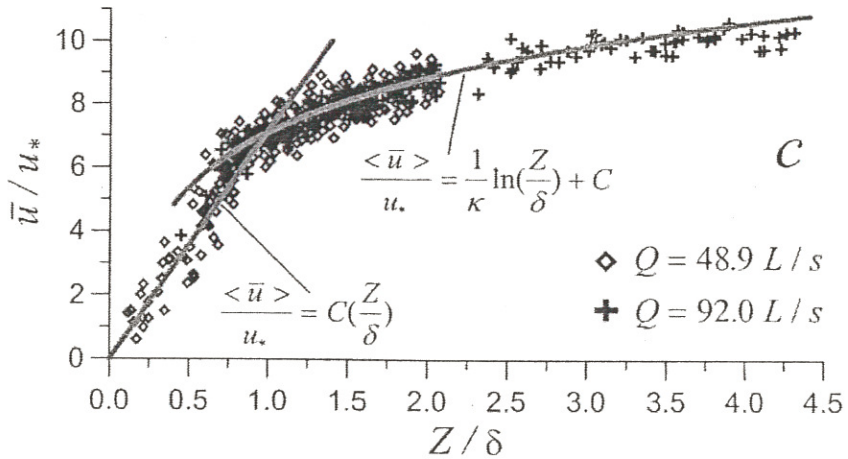

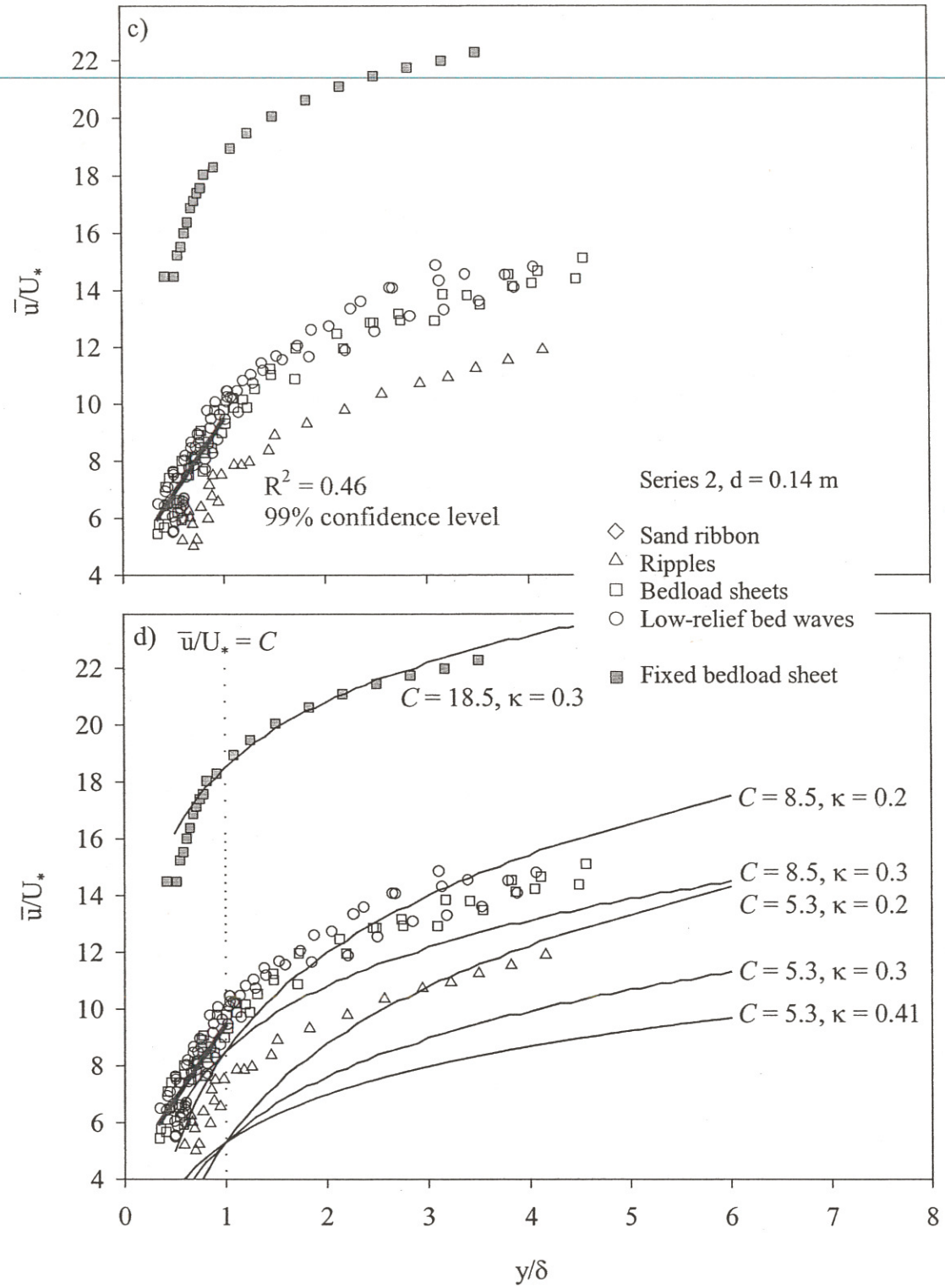

Since the roughness layer is approximately 30 mm and the maximum grain diameter is 32 mm, the bottom 20 % of the flow (approximately 30 mm) can easily be envisaged as being influenced by roughness elements, and therefore no logarithmic region would be expected in the current experimental data. However, Nikora *et al.* (2001) demonstrated that the logarithmic curve fitted their experimental data for y/δ values up to 4.5 (Figure 4.29). Consequently, the logarithmic curve is compared in Figure 4.30b and d with the present data

d) The law-of-the-wall was originally derived for flow over smooth beds, and was not explicitly formulated to describe the velocity distribution over a bed with any type of bed roughness (e.g. fixed or mobile sediment, uniform or mixed sized sediment and bedforms). However, the logarithmic law has been successfully applied in a variety of flow conditions. Kirkgöz (1989) applied the law-of-the-wall to measurements taken over fixed rough beds, forcing the gradient to equal that found over smooth beds in order for κ to equal 0.41, and imposing a linear fit to data displaying curvature.

2) When the law-of-the-wall is substituted by the velocity defect-wake law, κ values remain reduced from the clear water value of 0.41 (Nezu and Nakagawa (1993)), and Π coefficient results are predominately negative in contrast to previous studies. The empirical Π coefficient represents a variety of mechanisms which influence the entire velocity profile, and may amplify or negate each other. Over the fixed bedload sheet, κ exhibited a greater range, extending closer to the expected value of 0.41 compared with the mobile bed experiments, perhaps due to the lack of transported sediment which influences the fluid properties. This is supported by the fact that κ values are greater when determined from the whole flow profile, and not just the bottom 20 % where sediment concentration levels would be highest. Both κ and Π are elevated over the bedform crest. Once the flow is significantly modified by large clasts, the profile being integrated is no longer logarithmic near the bed, and consequently the value of κ may require adjustment, approaching 0.41 for low values of relative roughness. However, when reduced values for κ and Π are used, the velocity defect-wake law describes the experimental data reasonably well, with R^2 values greater than 0.93 at the 99% level of significance. Although, even when normalised, the velocity defect-wake distributions for all the experimental runs do not collapse to give a general trend due to the varying boundary conditions, in agreement with Kirkgöz (1989).

3) Time-averaged downstream velocity was found to be greatest over the bedform crest, where Reynolds stresses are at a minimum, reduced over the stoss, and lowest in the trough region where maximum values of Reynolds stress are located. Vertical profiles of downstream velocity in the separation and reattachment zones of the low-relief bed wave were observed to be slightly kinked, analogous to similarly located profiles over dunes which exhibited flow separation (Bennett and Best, 1995), suggesting the occurrence of flow separation downstream of the bed wave crest.

4) The average form related friction factor is 0.023, which is less than that attributed to the grain roughness (0.035), although estimates of form roughness using different methods exhibit great variability for the same experimental run (0.002-0.096). The average grain related equivalent sand roughness height (k_s') is approximated by 2-3D_{50}. The presence of a bimodal sand-gravel mixture complicates the prediction of flow

Chapter 5 : The turbulent flow structure over bimodal sand-gravel bedforms: implications for sediment transport and bedform development

5.1 Introduction

Flow turbulence exhibits a coherent structure, and is not random (Ashworth *et al*, 1996; Massey, 1998). However, turbulence is associated with great complexity, which accounts for its theoretical intractability (Tritton, 1988). Consequently, laboratory experiments present one viable method of increasing our understanding of turbulence, in this case with reference to water flow over a deformable bimodal sand-gravel mixture. Advances in measuring techniques and computer power facilitate the collection of large quantities of high quality turbulence data.

Much insight into the structure of turbulent flow has been achieved by employing flumes with smooth boundaries (Nezu and Rodi, 1986, Cardoso *et al.*, 1989, Steffler *et al.*, 1989). Even in this most basic configuration, experimental scatter and uncertainties remain due to complexity of the turbulent flow. For instance, it is still difficult to determine the velocity gradient used to calculate turbulence production, mixing length and eddy viscosity. A roughened bed surface is usually accomplished by gluing down uniform spheres (Grass, 1971; Kirkgoz, 1989), whilst non-uniform mixtures have received little attention (Wang and Dong, 1996). To date, limited velocity and turbulence measurements have been conducted over mixed sand and gravel beds at shear stresses where sediment transport (Song *et al.*, 1994; Nikora and Smart, 1997; Nikora and Goring, 2000) or bedforms occur (Pitlick, 1992; Livesey, 1995; Bennett and Bridge, 1995a, Bennett *et al.*, 1998). However, detailed velocity and turbulence measurements are available for fixed bedforms developed in sand sized sediment, which can be related back to measurements collected during equivalent mobile conditions (Nelson *et al.*, 1993; McLean *et al.*, 1994; Bennett and Best, 1995, 1996; Robert and Uhlman, 2001; Best and Kostaschuk, in press). The presence or absence of mobile sediment (bed and suspended load), bedforms, and in the case of mixed sediments, grain size sorting, fractional transport and roughness discontinuities, have a significant, but poorly understood, impact on the turbulent structure of the flow.

In this chapter, various turbulent flow parameters (e.g. Reynolds stress, turbulence intensity, correlation coefficient, turbulence production, eddy viscosity and mixing length), averaged over space and/or time, are presented for both mobile and fixed bimodal sediment beds. Comparisons are made between locations over the bedforms observed, varying shear stresses and flow depths, and mobile and fixed

surroundings (Massey, 1998). In reality, the loss of momemtum is gradual. The vertical variation in mixing length is described by Equation 5.5 (the dimensionless case is shown in Equation 4.18 and 5.6; the latter is based on Equations 4.11, 4.13, 4.14, 4.21 and 5.1 and includes a wake coefficient).

$$\ell = \kappa y\left(1-\frac{y}{d}\right)^{0.5} \tag{5.5}$$

$$\frac{\ell}{\delta} = \kappa\left(1-\frac{y}{\delta}\right)^{0.5}\left[\frac{\delta}{y}+\pi\Pi\sin\left(\frac{\pi y}{\delta}\right)\right]^{-1} \tag{5.6}$$

The production of turbulent energy extracts energy from the mean flow, due to the generation of turbulent fluctuations, which are typically associated with large scale coherent motions. The rate of turbulent generation, T, is expressed as:

$$T = -\overline{u'v'}\frac{\partial\overline{u}}{\partial y} \tag{5.7}$$

The correlation coefficient, R, of Reynolds stress (Equation 5.8), indicates the degree of similarity of turbulence, or in other words, the correlation between the Reynolds stress and the product of the rms values of both velocity components.

$$R = \frac{-\overline{u'v'}}{rmsu'.rmsv'} \tag{5.8}$$

5.2.2 Quadrant analysis

Conditional quadrant analysis of the instantaneous turbulent Reynolds stress ($u'v'$) allows quantitative understanding of the turbulence structure. The instantaneous downstream and vertical components of velocity are classified by this technique into four quadrants (Lu and Willmarth, 1973; Luchik and Tiederman, 1987). If the spanwise component of velocity (w) is also available, eight quadrants can be defined i.e. octant analysis. Quadrant analysis can be performed on the full instantaneous Reynolds stress signal, or just the values greater than a given threshold/hole size, H, which is expressed as:

$$H = \frac{|u'v'|}{rmsu'.rmsv'} \tag{5.9}$$

Thresholding enables the higher energy turbulent events to be selectively analysed, which contribute significantly to Reynolds stress and play an important role in the entrainment and transport of sediment. The threshold value is arbitrarily defined, since the number of turbulent events recorded diminishes as the threshold value increases. In both boundary layers and over bedforms, the detection of quadrant two events is typically associated with thresholds of 1-5, whereas for quadrant four events values of 2-3 have been employed (Lu and Willmarth, 1973; Luchik and Tiederman, 1987; Bennett and Best, 1995, 1996), although lower values down to zero have also been presented (Buffin-Bélanger and Roy, 1998; Buffin-Bélanger *et al.*, 2000).

5.2.3 *Time series analysis in the frequency domain: spectral analysis*

Spectral analysis decomposes a record of fluctuations in time (in this case temporal variations in velocity) into a suite of waveforms using Fourier methods (Newland, 1975; Swan, 1995). A time series can be represented by a combination of sinusoidal functions (sine and cosine waves) with a given amplitude, frequency and phase. For each wave frequency, the amplitude and phase are determined by Fourier analysis, transforming the time series into the frequency domain. Waves with a significantly high amplitude (peaks) are identified, and can be related to periods of cyclicity in the time series (Kostaschuk, 2000). The frequency strength can be expressed by amplitude and power (i.e. the variance at that frequency). The maximum resolvable frequency is known as the Nyquist frequency, which is equal to half the length of the time series. Consequently, when data is uniformly sampled, the minimum resolvable wavelength is equal to twice the sampling interval, since in order to define a waveform, at least two observations are required to represent the crest and associated trough. However, the uniform sampling of higher frequencies can mimic lower frequency waveforms (i.e. an aliasing effect, which increases the noise at higher frequencies). The present spectral analysis is performed on LDA velocity measurements, which are sampled discontinuously through time. A Fourier spectrum can be generated for unevenly sampled data using the Lomb-Scargle periodogram (Press and Rybicki, 1989). This technique does not require the generation of an evenly spaced data set by resampling, which can cause some of the information (signal) to be lost. Waveforms with frequencies higher than the Nyquist frequency are not automatically aliased to lower frequencies when the data is unevenly sampled with respect to time, since some observations are temporally closer than the average sample interval.

Spikes in the spectra can result from random effects (i.e. noise). In order to identify peaks resulting from the signal, peak-based critical limit significance levels are employed. When the power is uniformly spread across the spectrum it is described as 'white noise', which can be used as a null hypothesis of randomness. A 99.9% critical limit is where only 1 in 1000 separate random noise events would generate the amplitude of the largest peak by purely random chance. The LDA records of downstream and vertical velocity over time were analysed using the following procedure:

1) Apply a tapering function (cosine with alpha = 0.1) which smoothes the ends of the data record to zero. The series is assumed to be periodically continuous, and consequently any difference between the end points will cause a jump in the frequency spectrum. The time series is multiplied by the tapering function, which diminishes to zero at both ends, and causes the spectrum to be smoothed.
2) Remove the trend and mean of the time series by subtracting a linear least squares fit in order to spread energy to higher frequencies.

and d) illustrate that values of u_{skew} increase as the water surface is approached. Elongated zones of negative u_{skew} values (< 0.6) are highlighted in Figure 5.2c by the letter S, and are observed to extend downstream at approximately 0.04 m above the bed, coinciding with bands of maximum positive v_{skew} values (> 0.4, represented by the letter S in Figure 5.2d). The zones identified in Figures 5.2c and d represent turbulent shear layers generated from coarse, exposed grains (e.g. the clast 0.25 m along the flume in Plate 5.1 is associated with turbulence production at position A in Figure 5.2d), and the crests of bedload sheets. Under the downstream shear layer (0.02 m above the bed, and 0.00-0.25 m along the flume) reduced v_{skew} values and increased u_{skew} values are recorded (approximately 0.2 and –0.2 respectively), reflecting the encroachment of the turbulent wake on the developing boundary layer (McLean *et al.*, 1994). Values of v_{skew} tend to fall towards the water surface.

Figure 5.2: *Spatial distribution maps of time-averaged velocity moments. Flow is from right to left. The bedload sheets are shown in grey, and the white area indicates where measurements were not possible. Crests are located at 0.13 and 0.56 m along the flume. Shear layers are identified by the letter S. A shear layer is developed from a coarse grain at position A.*

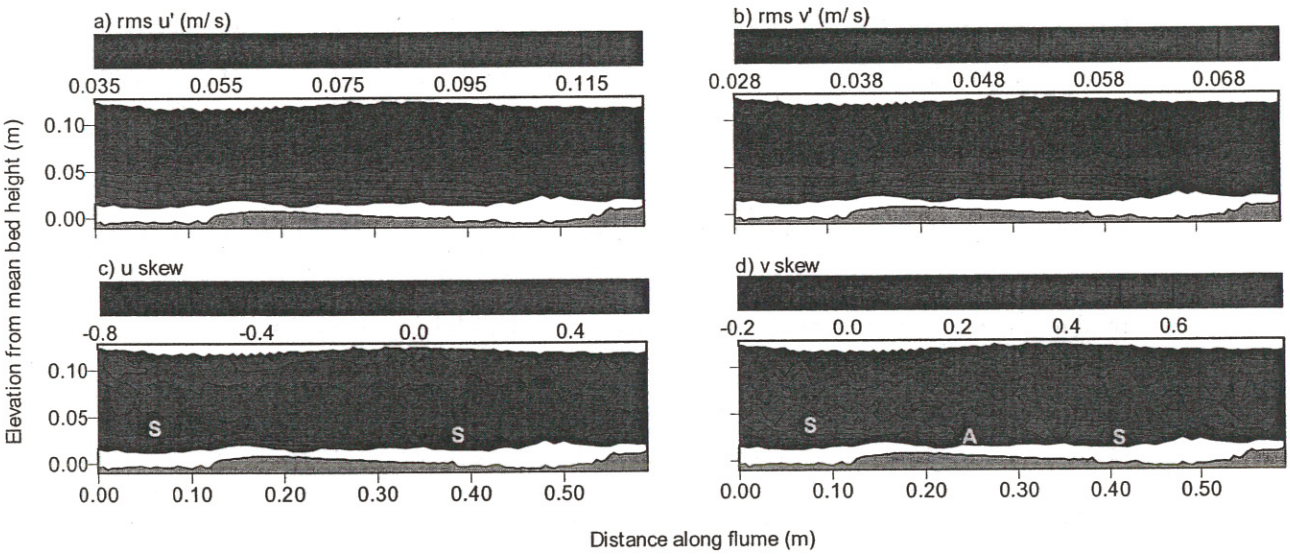

***Figure 5.3**: Spatial distribution maps of time-averaged velocity moments. Flow is from right to left. The low-relief bed waves are shown in grey, and the white area indicates where measurements were not possible. The crest is located at 0.3 m along the flume. The shear layer developed from the crest of the low-relief bed wave is visible from S' to S''.*

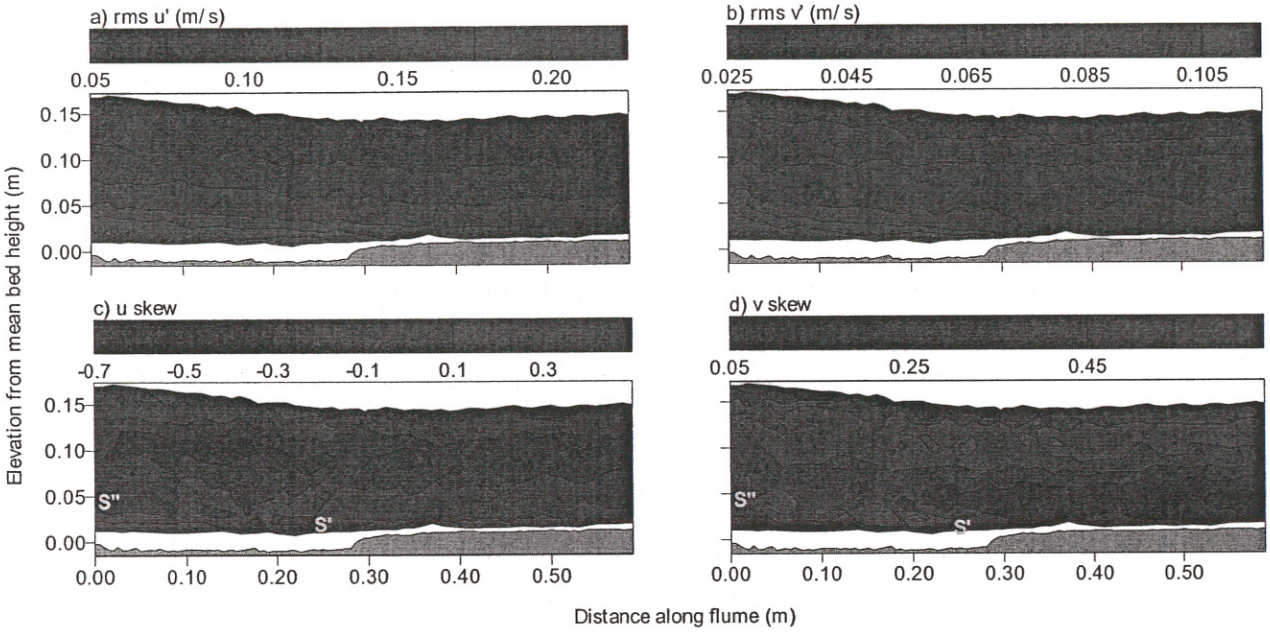

The distribution of low skewness values of the downstream component of velocity, and high values of skewness of the vertical component of velocity, are similar over all the bedform types, highlighting the presence of turbulent shear layers originating at bedform crests. In the case of dunes and low-relief bed waves, there is also a zone of low downstream skewness and elevated vertical skewness higher in the flow, which parallels the water surface. The same shear layers can also be identified from the distribution of quadrant 2 (i.e. ejection) events, which will be considered in Section 5.3.4. Shear layers are formed at both the bedload sheet crest and from coarse particles protruding above the surface of the sheet. The shear layer generated on the mid-back of the downstream bedload sheet (Figure 5.2d, highlighted by the letter A) is associated with a coarse clast (Plate 5.1, 0.25 m along the flume). Turbulence generation by the coarse clast can merge with, and distort any evidence of, the shear layer generated at the downstream crest. Furthermore, if the bed were mobile, this coarse clast would be expected to quickly overpass the fine bedform stoss and not present a long term obstruction to the flow at this location. The fixed dunes and ripples studied by Bennett and Best (1995,1996) were uniformly covered in 0.22 mm diameter glass spheres, and therefore were not subject to variations in surface roughness. Both the fixed low-relief bed waves and bedload sheets in the present study exhibit grain size sorting, with a distinct change between the crest and trough, and a gradual transition elsewhere. Over the fixed bedload sheet the roughness changes are less distinct as they occur over a much smaller

the flow discharge, depth, relative roughness or bed state (i.e. mobile or fixed) in the present experiments. However, the coefficients in the exponential turbulence intensity curves have been shown by Song and Graf (1994) to be influenced by the occurrence of flow acceleration and deceleration, although in the present experiments all the runs were conducted under uniform flow conditions and therefore would not be expected to vary.

5.3.1.4.1 Downstream turbulence intensity

Agreement with the exponential curve ($a_u = 2.3$, $b_u = 1$) was found in the intermediate flow region ($0.3 < y/d < 0.9$) of the alluvial Missouri River (McQuivey, 1973), and gravel-bed rivers in New Zealand (Nikora and Smart, 1997). However, Nikora and Smart (1997) observed that the values of downstream turbulence intensity in the intermediate flow region plotted above the exponential curve when relative roughness was reduced. In the intermediate flow region ($0.3 < y/d < 0.9$), when $d = 0.14$ m (Figure 5.4b), the normalised downstream turbulence intensities for the low-relief bed waves and bedload sheets (both mobile and fixed, high relative roughness) plot above the exponential curve, whereas the ripple run (low relative roughness) plots below the curve, in contrast to Nikora and Smart (1997). However, in both cases the dependency of downstream turbulence intensity on relative roughness is inferred from the divergence of only one data set from the others. No variation in downstream turbulence intensity due to relative roughness is apparent in the intermediate flow region at a flow depth of 0.18 m (Figure 5.4a).

5.3.1.4.2 Vertical turbulence intensity

In the present mobile experiments, the measured vertical turbulence intensities are greater than predicted by the exponential curve of Nezu and Nakagawa (1993, $a_v = 1.27$, $b = 1$) when $y/d > 0.3$. Krogstad *et al.* (1992) found that the vertical turbulence intensity was elevated over a rough bed compared with a smooth boundary, and concluded that the effects of the boundary roughness extend into the outer flow, which is at variance with the 'wall similarity hypothesis' of Townsend (1976). Steffler *et al.* (1989) also found high values of vertical turbulence intensities, although Nezu and Rodi (1986) claim their vertical measurements were not accurate. Normalised vertical turbulence intensities could be reduced in order to coincide with the exponent curve by increasing the shear velocity, however this would also reduce the downstream turbulence component, which for series 1 (Figure 5.4a) presently collapses around the exponential curve. The presence of bedforms in the current study encourages the flow to move vertically by the generation of shear layers from the elevated crest, which transfer turbulent energy throughout the flow depth in the case of dunes. Furthermore, coarse clasts also hinder downstream motion, and can deflect and generate turbulent fluid vertically.

5.3.1.4.3 Divergence from the exponential turbulence intensity curves

Figure 5.4: *Spatially-averaged downstream and vertical turbulence intensities, normalised with shear velocity. The semi-theoretical curves of Nezu and Nakagawa (1993, pg 53) are given for comparison.*

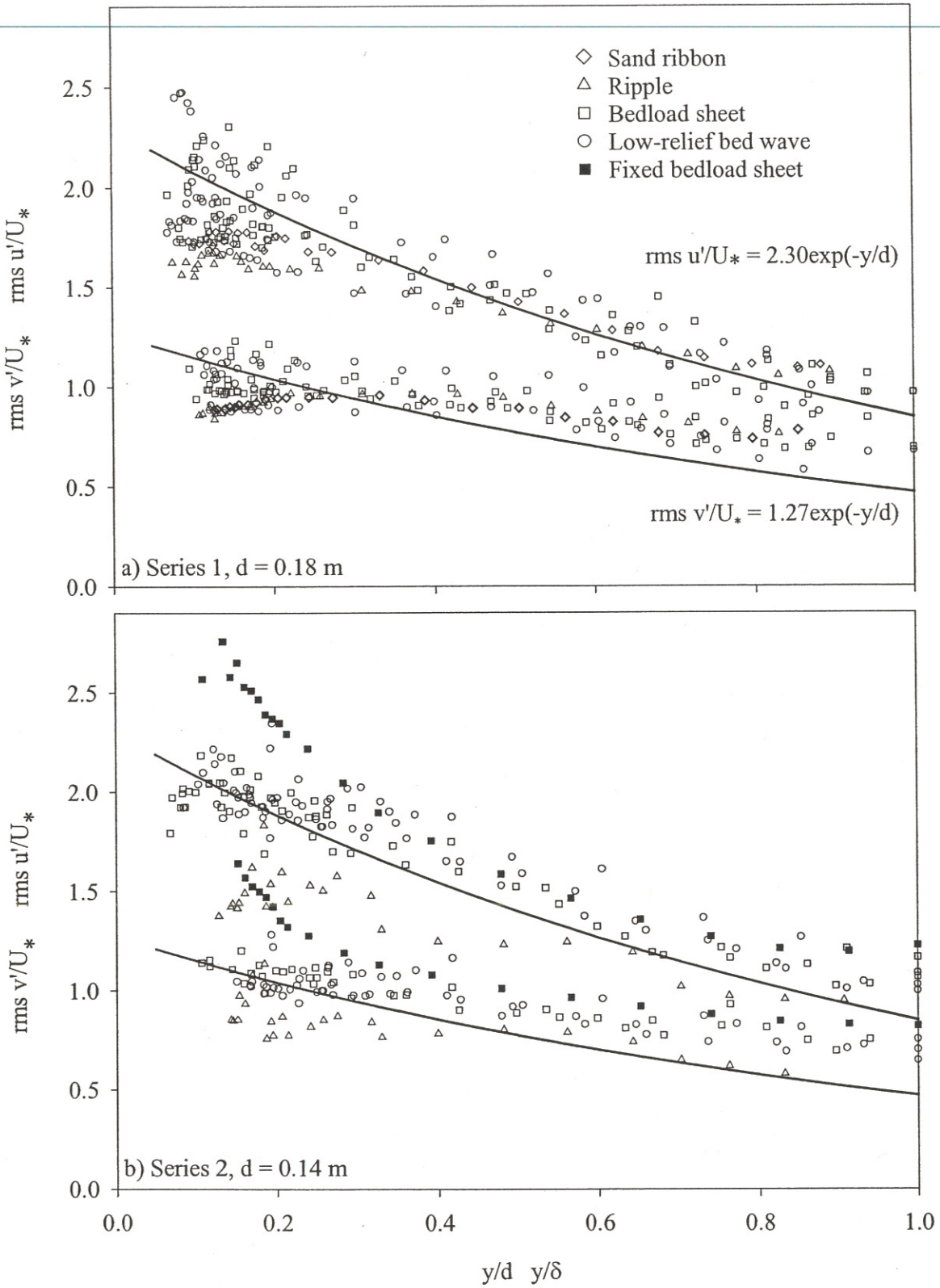

In the vicinity of the wall (i.e. $y/d < 0.3$) the influence of roughness is discernible i.e. the roughness layer. Various experimental research initiatives report that as relative roughness increases, the

Where just ripples are present, the sand fraction in gravel interstices is likely to be entrained, causing greater exposure of the large clasts constituting the extensive armour layer (up to 32 mm diameter), which may result in greater relative roughness than inferred from consideration of just the small (~ 5 mm high), spatially-limited ripples (about 120 mm wide and 700 mm long). However, entrainment of fine sediment from the gravel interstices also occurs when narrow (~ 60 mm wide) sand ribbons prevail (run A, $d = 0.18$ m). The sand ribbons, which have a lower relative roughness (~ 0.01), exhibit a higher downstream turbulence intensity near the bed ($y/d < 0.3$, Figure 5.4a) compared with the ripples. The sand ribbon and ripple bed configurations are most similar in nature to previous studies of turbulence intensity over flat smooth and rough beds (Grass, 1971, 1996; Wang and Dong, 1996), since the bedforms have minimal relief and spatial extent, and sorting of the original bimodal bulk mixture is limited. Consequently, a comparison of the sand ribbon and ripple runs supports the contention that relative roughness is inversely related to downstream turbulence intensity. However, if the ripple bed experimental run is compared with the bedload sheets and low-relief bed waves, relative roughness is found to be directly related to downstream turbulence intensity due to the presence of bedforms. Elevation changes over bedforms result in variations in flow velocity, for example in the lee of a bedform flow expands and decelerates, which increases the local velocity gradient, shearing and the production and intensity of turbulence. Previous experimental work concerning turbulence intensities has focused on smooth beds, and uniform or poorly sorted sediment with no bedforms being present. In these cases, the relative roughness term is applicable since the value for the equivalent sand roughness is fairly well defined. However, when the sediment has a bimodal distribution (size sorting effects), or bedforms are developed (form roughness), it is difficult to identify a single characteristic length scale.

The fixed bedload sheet exhibits greater turbulence intensity and relative roughness compared with the mobile bed equivalent (Figure 5.4b). The relative roughness is partly enhanced over the fixed bedforms due to the reduction in water depth (section 4.3.1). However, the value of relative roughness is also dependent on the method by which bed height is measured. Only two crests can be used to measure bedform height with a point gauge in the fixed bed run (average of 15 mm). In the equivalent mobile bed run (J), the height of 138 bedload sheets are measured (average of 12 mm) using an ultrasonic probe.

The decreased roughness (due to the absence of bedload, Nikora and Goring (2000)) and flow depth over the fixed bed compared with the mobile equivalent, cause higher flow velocities (i.e. $U = 0.77$ and 0.70 m s^{-1} over the fixed and mobile bedload sheet respectively), and larger velocity gradients at location of rapid change in bed geometry e.g. downstream of the bedform crest and large, protruding clasts. Where stronger velocity gradients exist, shearing occurs and turbulence intensity is increased. Since the fixed bedforms and sediment did not move relative to the fluid, the velocity gradient over any

the change in slope over the crestal platform and associated with the start of flow expansion), turbulence intensities plot on the semi-theoretical curves of Nezu and Nakagawa (1993).

Over a uniformly roughened dune (Bennett and Best, 1995), both components of turbulence intensity are greatest near the bed ($y/d < 0.3$) in the trough region, with downstream turbulence intensity gradually decreasing over the dune stoss. Carling *et al.* (2000b) and Kostaschuk (2000) also observed turbulence intensity to be elevated in the wake zone of dunes. Bennett *et al.* (1998) confirm that near bed ($y/d < 0.3$) turbulence intensities are increased relative to the spatial average in the trough, but reduced over the crest of low-relief bed waves associated with upper-stage plane beds.

5.3.1.4.7 Discussion of the spatial distribution of turbulence intensity

Downstream of the point of flow expansion, which occurs just upstream of the bedform crest, turbulent fluid from the free shear layer is transferred towards the bed by the advection of high turbulence intensity flow along the mean streamlines around the flow deceleration zone (Nelson *et al.*, 1993). In the trough of the low-relief bed wave, the elevated values of streamwise turbulence intensity that occur approximately 20-30 mm away from the bed coincide with the presence of a highly turbulent shear layer generated from the upstream crest. The shear layer is dissipated as it advects and disperses downstream from its crestal origin, and therefore its influence on near-bed flow gradually reduces over the length of the downstream bedform. Furthermore, flow is topographically accelerated over the bedform stoss side, damping turbulence, which produces reduced turbulence intensities at the crestal platform (regions C and E in Figure 5.5iib; Nelson and Smith, 1989; Nelson *et al.*, 1993). The presence of the shear layer also provides the main contribution to the elevated vertical turbulence intensities in the trough of the low-relief bed wave, in conjunction with the greater roughness associated with this region.

Over the bedload sheet, the morphological and textural changes are not as distinct as over the low-relief bed wave. Consequently, shear layer development is associated with both the crest of the bedload sheet and from protruding coarse clasts, which can occur in the trough and stoss, impacting any region immediately downstream. For example, in Plate 5.1 a coarse clast can be observed approximately 0.25 m along the flume, which coincides with the mid-back profile in Figure 5.5iia, which exhibits the highest turbulence intensity values (highlighted in red above the spatial average). The nearest upstream profile (lower back), demonstrates the lowest turbulence intensities observed (highlighted in red below the spatial average in Figure 5.5iia). Therefore, it can be concluded that the high turbulence intensities over the mid-back of the fixed bedload sheet result from a wake generated by the coarse clast rather than the upstream crest. Furthermore, due to the substantially shorter streamwise extent of the bedload

facing steps, due to the size of the separation zone being reduced by topographic acceleration (Nelson and Smith, 1989).

5.3.2 Reynolds stress

The determination of bed shear stress, which encompasses the horizontal and vertical variation of at-a-point Reynolds stress, is considered in Chapter 4 over both mobile and fixed beds. Reynolds stress decreases as the water surface is approached over fixed bedload sheets and low-relief bed waves (Figure 5.6), due to the influence of the free surface and the low velocity gradients in this area. Reynolds stress is at a maximum (> 7.5 Pa) in the trough of the low-relief bed wave (i.e. less than 0.02 m above the bed, and from 0.0 to 0.3 m along the flume), which is also true of the rms values of both the downstream and vertical velocity components (Figure 5.3). Reynolds stress is also maximised along the shear layer originating from the crests of fixed dunes and ripples (Bennett and Best, 1995, 1996). High stresses (> 1.4 Pa) are not confined to the trough region of bedload sheets, but occur along the entire bedform length within 40 mm of the bed. A minimal number (< 2 %) of negative Reynolds stress values were recorded near the water surface (minimum of -0.3), which indicates that precise equilibrium flow conditions were not attained over the fixed bedforms, as was also the case in the experiments of Nelson *et al.* (1993). Ideally Reynolds stress measurements (used in the calculation of quadrant analysis, turbulence production, eddy viscosity and mixing length) should be taken parallel to the streamlines. However, when bedforms are present, the streamlines diverge marginally from the bed morphology (Nelson *et al.*, 1993), which is used as a reference point. Negative values of Reynolds stress were omitted from any calculations.

Figure 5.7 and 5.8 illustrates the linear decrease in Reynolds stress in the outer flow region as the water surface is approached. The maximum Reynolds stress in each profile defines the top of the roughness layer ($y/d \approx$ 0.2-0.3, $y \approx$ 30-50 mm for the mobile experimental runs), in which Reynolds stresses are diminished due to drag and the interaction of mobile sediment with the fluid (Song *et al.*, 1994).

Near the bed ($y/d <$ 0.3), values of Reynolds stress are elevated at all locations over the fixed bedload sheet, and for the spatially-averaged case (Figure 5.8iia; region A in Figure 5.7b), but this was not true for the equivalent mobile bedload sheet (Figure 5.8ia). However, measurements taken over the lower back of the fixed bedload sheet are below the spatial average (region B in Figure 5.8iia), as was also observed for turbulence intensity. Over the fixed low-relief bed wave, elevated Reynolds stress (and turbulence intensity) values below $y/d =$ 0.3 were only apparent in the separation and reattachment zone (region C in Figure 5.8iib). Elevated Reynolds stresses (and turbulence intensities) were also noted in the trough region of the mobile low-relief bed wave at $y/d \approx$ 0.2 (region A in Figure 5.8ib). Furthermore, Reynolds stresses (and turbulence intensities) are diminished for the profile taken over the

Figure 5.6: *Maps of the spatial distribution of Reynolds stress over a) fixed bedload sheet, b) fixed low-relief bed wave. Flow is from right to left. Bedforms are highlighted in grey, while the white zone indicates no measurements were possible.*

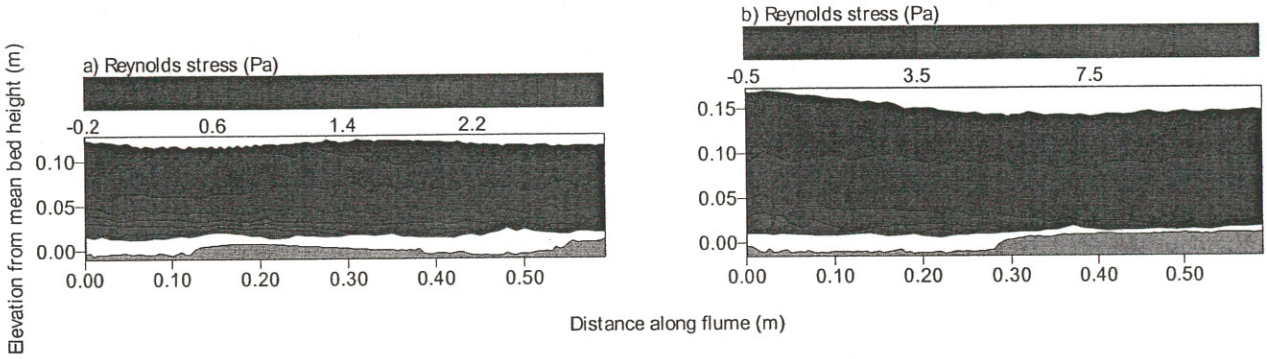

Figure 5.8: *Normalised Reynolds stress against dimensionless flow depth for specific bedform regions. Highlighted areas are discussed in the text.*

i) Mobile bed conditions

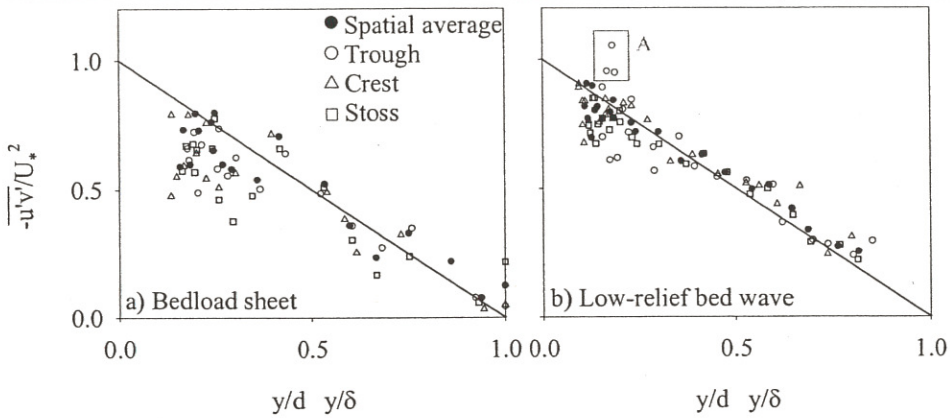

ii) Fixed bed conditions

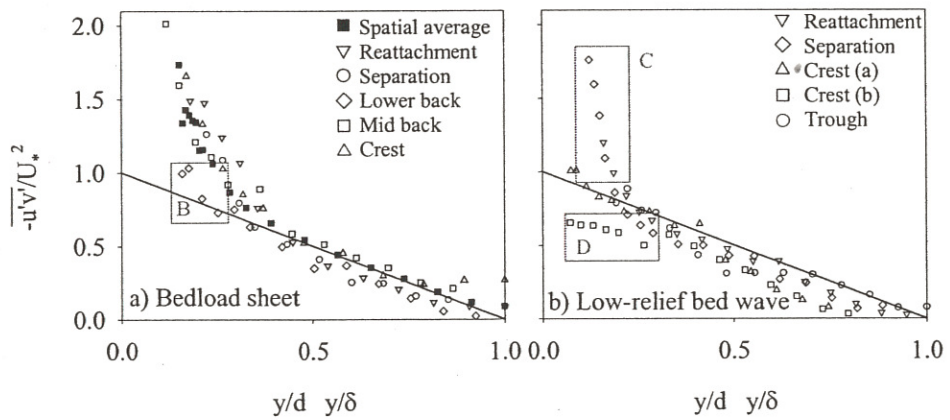

Figure 5.9*: Normalised Reynolds stress measurements plotted against dimensionless flow depth.*

i) Fixed low-relief bed wave (white symbols) and dune (black symbols, data from Bennett and Best (1995)).

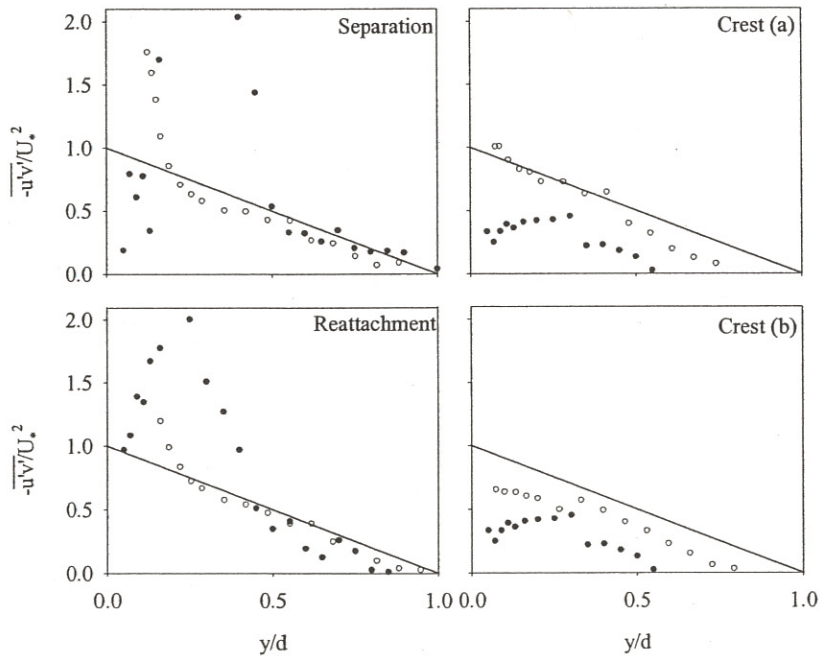

5.3.3 Correlation coefficient of Reynolds stress, R

The correlation coefficient, R, is defined as the ratio of the Reynolds stress to the product of the downstream and vertical turbulence intensities. If the production of turbulent energy equals its dissipation, R is constant in the intermediate flow region ($0.2 > y/d > 0.6$, Figure 5.10 and 5.11), illustrating a good correlation between the downstream and vertical turbulent fluctuations. However, R decreases near the bed ($y/d < 0.2$) and free surface ($y/d > 0.6$) where turbulent energy production and dissipation are greater respectively. The reduction in the correlation coefficient observed near the bed ($y/d < 0.2$, Figure 5.10), results from the interaction between the internal boundary layer and the overlying turbulent wake region (Nelson *et al.*, 1993). Nezu and Nakagawa (1993) compared data from boundary layers, pipe flows and open-channels, and found the distribution of R to be universal regardless of mean flow parameters and boundary roughness. Furthermore, the present data demonstrates no apparent distinction in the correlation coefficient of Reynolds stress between different runs, mobile or fixed bedload sheets (Figure 5.11) or specific regions of the bedforms (Figure 5.10). Nezu and Nakagawa's (1993) calculated curve (for a Reynolds number, $\mathrm{Re} = U_* d/\nu$, based on a shear velocity of 600) describes their compilation of data well, with the exception of the wall region ($y/d < 0.2$), and is plotted in Figure 5.10 and 5.11 for comparison with the present experimental results. The present data follows a similar trend to the curve proposed by Nezu and Nakagawa (1993), but plots below, with a roughly constant value of 0.35-0.4 in the intermediate region ($0.2 < y/d < 0.6$) rather than 0.4-0.5. The universality of R is therefore in question. The divergence from the curve of Nezu and Nakagawa (1993) could illustrate a dependency of R on Reynolds number, since the maximum Reynolds number of the data compiled by Nezu and Nakagawa is 90000, whereas for the present experiments the Reynolds number varied from 71421 to 147500. However, Reynolds number ranged from 350000 to 1300000 in the field measurements of Nikora and Goring (2000), and R varied from 0.3-0.5 in the intermediate flow region, with the lowest values being attributed to flows with weak sediment movement, but no bedforms, and the highest Reynolds numbers. Lower values of R can be attributed to sediment transport and the presence of bedforms, which were not considered in the data collated by Nezu and Nakagawa (1993). However, in the present data set, the fixed bedload sheet (no sediment transport) also has relatively low R values in comparison with the calculated curve in the intermediate flow region ($0.2 < y/d < 0.6$, Figure 5.11b).

Since sediment transport is absent over the fixed bed, the occurrence of bed features, which present topographic variations to the flow, must be influential in reducing the correlation coefficient, in addition to bedload movement (Nikora and Goring, 2000). Nelson *et al.* (1993) found that the correlation coefficient over the lower stoss of fixed dunes in the boundary layer and overlying wake were much lower (i.e. 0.1-0.2) and higher respectively than 0.4 (the value expected in a flat-bed boundary layer),

Figure 5.11: *The spatially-averaged correlation coefficient of Reynolds stress against dimensionless flow depth.*

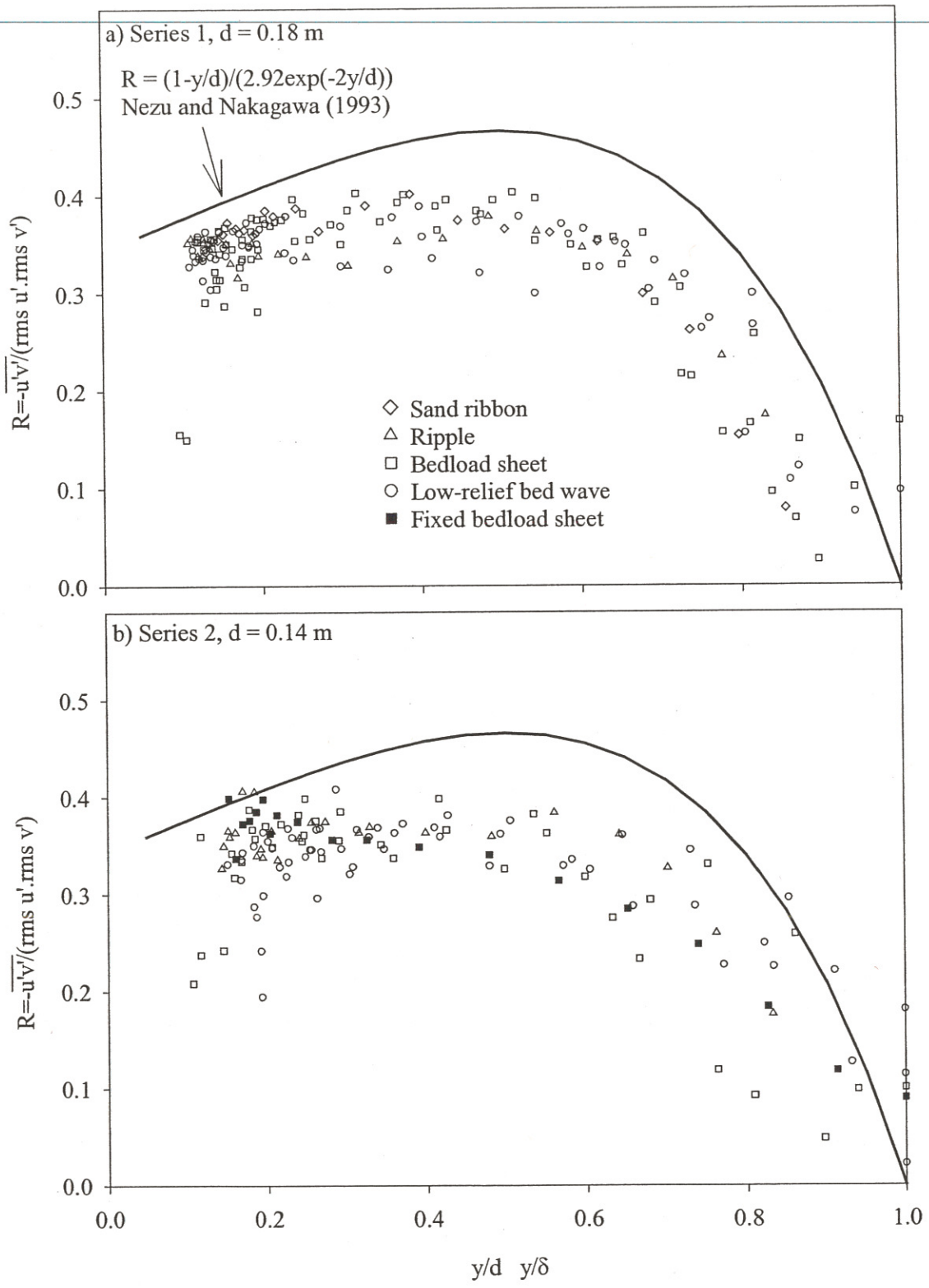

the bed where the turbulent shear layers are initiated. Furthermore, the bedload sheet in the test section was only ~ 0.4 m long, and the areal extent of the shear layer is dependent on the threshold and interpolation procedure employed. During the experimental program, flow separation was visually observed from the coarse gravel grains (up to 32 mm in diameter), which predominately rest in the trough region.

Figure 5.12: *Maps of the spatial distribution of the normalised number (%) of quadrant events over fixed bedload sheets. Flow is from right to left. Q and H respresent the quadrant and threshold respectively. The bedload sheets are shown in grey. No measurements were obtained in the white regions. Elevated values (highlighted by letters) are discussed in the text.*

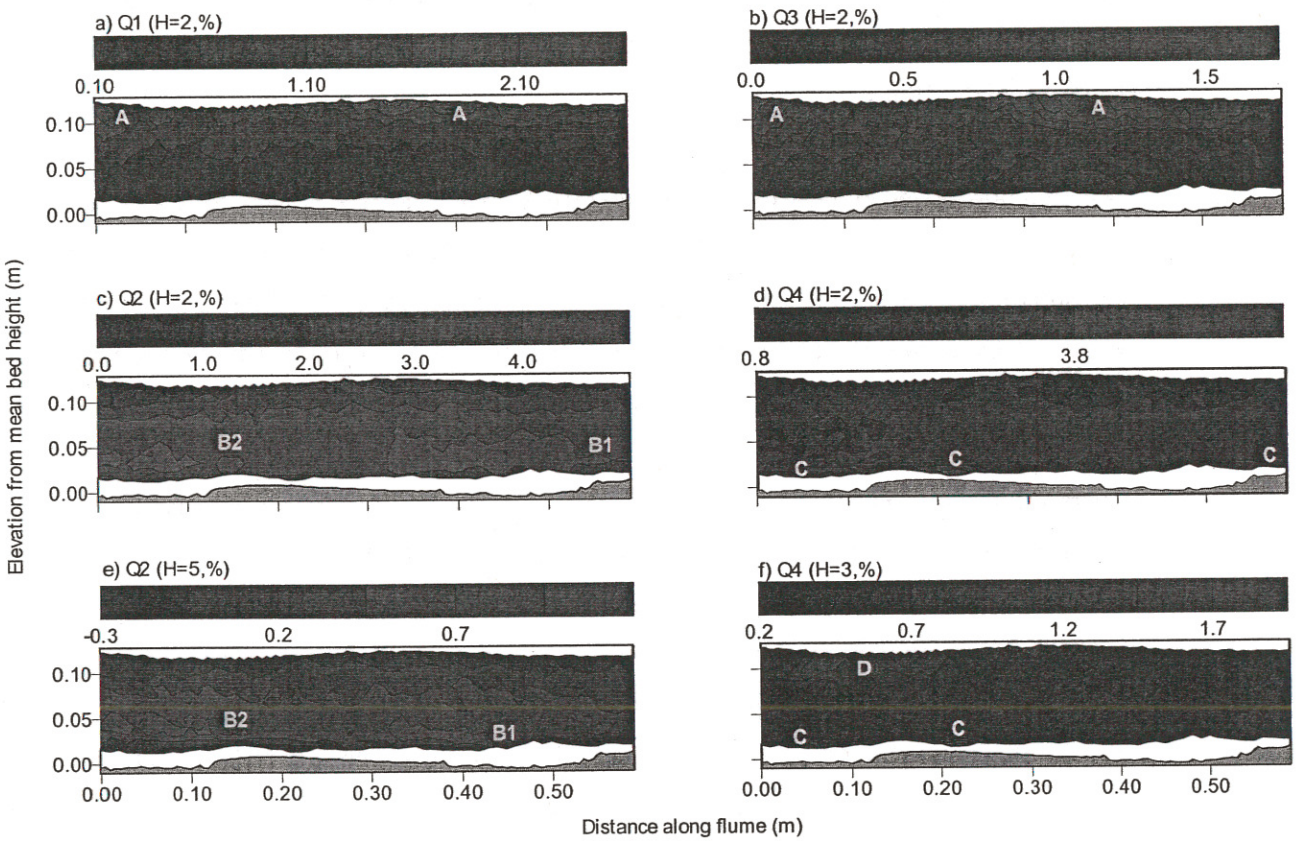

~ 10) compared with locations in the expansion/separation zone downstream of the bedform crest and coarse, isolated particles (Figure 5.13d-f, up to H ~ 7). Noise in the LDA signal may partially account for contributions to Reynolds stress at higher thresholds. However, Appendix I illustrates that the error is typically less than 1 % at a threshold of 2. The suspension of sediment and the production of Reynolds stress are thought to be significantly influenced by low frequency, high magnitude quadrant 2 events (i.e. H > 6). Lapointe (1996) notes that energetic quadrant 2 events occur for 1-5 % of the time, but account for 20-90 % of sand suspension episodes and exchange of turbulent momentum. Bennett and Best (1995) propose possible sources for these infrequent, energetic quadrant 2 events. Firstly, they may be produced by variations in the shear layer velocity gradient over time. Alternatively, their formation may relate to the interaction and pairing of vortices. Finally, 'flapping' of the shear layer at a reduced frequency was suggested as a possible origin for these rare, high energy quadrant 2 events. Furthermore, Lapointe (1996) determined that the greatest sand suspension events occurred more frequently under deeper flow conditions. The degree of flow separation, Reynolds stress and velocity differential across the shear layer, are influenced by bedform steepness and relative roughness (i.e. ratio of bedform height to flow depth), which in turn impacts on the intensity of shearing, and consequently both the intensity and frequency of vortex shedding (McLean *et al.,* 1994).

The fractional contribution to $-\overline{u'v'}$ from quadrant 4 events was most similar in magnitude to that from quadrant 2 events in the expansion/separation zones (located in the lee of bedform crests and isolated coarse particles; Figure 5.13d and f), due to the reduction in contributions from quadrant 2 events. The fractional contribution of quadrant 4 events is approximately 0.6 at H = 0 in the shear layer and expansion/separation zone, and rises to around 0.8 in the free stream. Similar contributions to $-\overline{u'v'}$ (> -0.2) are made by quadrant 1 and 3 events at all the 'characteristic' points shown in Figure 5.13, and above a threshold of 3 contributions are virtually zero.

5.3.4.2 Low-relief bed waves

The occurrence of quadrant 1 and 3 events rises towards the water surface, with peaks downstream of the bedform crest where the flow expands (Figure 5.14a and b, highlighted by the letter A). The same trend was found over fixed dunes in the experiments of Bennett and Best (1995). A band of high percentage occurrence of quadrant 2 events is apparent at both a threshold of 2 and 5 (Figure 5.14c and e, shown in red), which follows the curvature of the water surface, causing the values along the back of the bedform (0.4-0.6 m along the flume, > 2.8 % at H = 2) to be elevated compared with those in the trough region (0.0-0.3 m along the flume, < 2.8 % at H = 2). A similar mid-depth region dominated by high magnitude quadrant 2 events has been illustrated in flat bed flows (Willmarth and Lu, 1974). High magnitude quadrant 2 events can advect from the near-bed region into the outer flow, growing in

At a threshold of 5, a narrow zone of high occurrence can be identified (> 0.4 %, letter B in Figure 5.14e), which extends from the crest (0.3 m along the flume, B'), rising downstream and amalgamating with the main band of elevated values approximately 0.05 m along the flume and 0.05 m above the mean bed height i.e. B" in Figure 5.14e. This feature (B' to B" Figure 5.14e) confirms the development of a shear layer from the low-relief bed wave crest, which was earlier identified from the spatial distribution of skewness of the vertical velocity component (Figure 5.3d). Turbulent shear layers, identified by an elevated occurrence of quadrant 2 events, have also been observed to be developed from the crests of fixed ripples and dunes (Bennett and Best, 1995, 1996). A high normalised number of quadrant 4 events at a threshold of 2 and 3 (Figure 5.14d and f, > 3.5 at H = 2, > 1 at H =3, represented by the letter C) extends from the change in slope in the crestal platform, and occurs throughout the trough region (i.e. 0.00-0.35 m along the flume), underlying the shear layer which develops from the crestal region of the low-relief bed wave. Elevated values of the normalised number of quadrant 4 events were also observed in the flow separation region over fixed ripples and dunes (Bennett and Best, 1995, 1996). The increased occurrence of quadrant 4 events highlights the transfer of relatively high velocity fluid along the shear layer towards the bed, associated with bedload entrainment and transport (Drake *et al.,* 1988; Williams *et al.,* 1989b; Nelson *et al.,* 1995). Fluid and momentum must be transferred to the area of flow separation and reattachment in order to counteract the effects of flow separation in the bedform lee and the removal of fluid by quadrant 2 events, thereby maintaining continuity.

Fractional contributions to $-\overline{u'v'}$ from quadrant 1 and 3 events are similar at all points in the flow (approximately –0.2 at H = 0), with little being added over a threshold of 3 (Figure 5.15). Similar findings were reported in Section 5.3.4.1 for the turbulent flow field over the fixed bedload sheets. The only exception occurs for points located within the high shear zone previously identified in the free stream (quadrant 2 occurrence > 3.8 % at H = 2, Figure 5.14c), where fractional contributions from quadrant 1 and 3 are around –0.5 at H = 0 (Figure 5.15g and i).

At all locations and thresholds considered in the flow field over a low-relief bed wave, quadrant 2 events dominate the fractional contribution to $-\overline{u'v'}$ (Figure 5.15). However, quadrant 4 events almost equal quadrant 2 events with respect to fractional contributions to $-\overline{u'v'}$ (approximately 0.6 at H = 0) in the flow expansion zone downstream of the low-relief bed wave crest (Figure 5.15d and e). Quadrant 2 events contribute to $-\overline{u'v'}$ at higher threshold values in shear zones (H ~ 12, Figure 5.15a-c, g and i) compared with the expansion zone downstream of the bedform crest (H ~ 6, Figure 5.15d and e). In the free stream, points within the band of high percentage occurrence of quadrant 2 events (> 3.8 % at H = 2, Figure 5.14c) also exhibit high fractional contributions (approximately 1.2 at H = 0, Figure 5.15g and

Figure 5.15: *Fractional contribution of each quadrant to* $-\overline{u'v'}$ *over a range of thresholds. The location of each point over the low-relief bed wave is shown in Figure 4.6.*

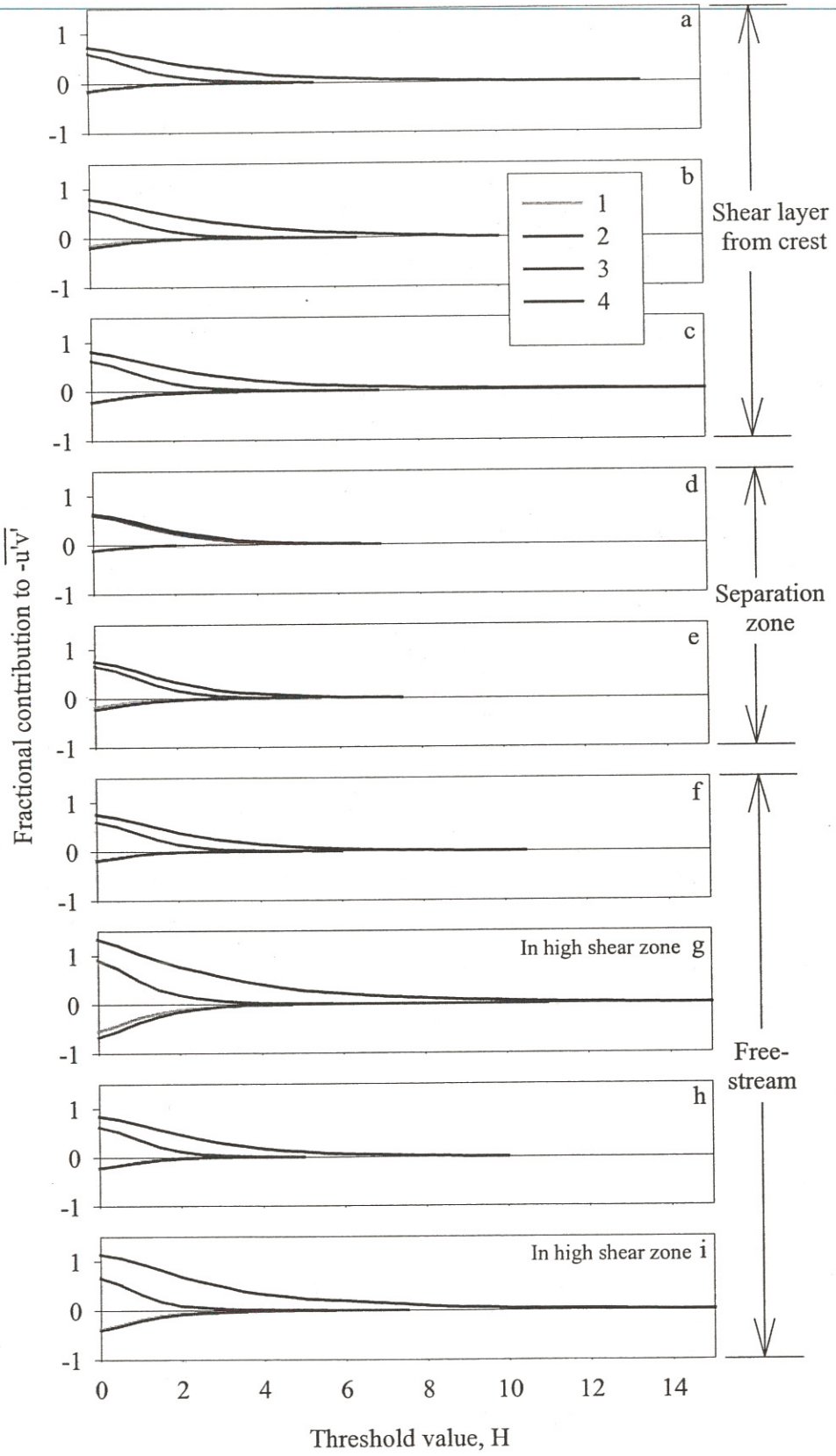

elements, a true inertial subrange is not present due to the systematic change in the shape of the energy spectrum over the flow profile. They also concluded that the rates of turbulent energy dissipation over roughness elements are very high in comparison with other common geophysical liquid flows, and yet correspond to the local rates of turbulent energy production in open channel flow. There is excess turbulent energy near the bed where production is concentrated, and a deficit near the free surface. However, with increasing distance from the boundary, turbulence becomes less anisotropic due to mixing (Roy *et al.*, 1996).

5.3.5.1 Classical boundary layer bursting (hydraulically smooth bed)

Over a smooth wall, turbulent energy and Reynolds stress are generated by the bursting cycle near the bed, consisting of multiple ejection and sweep events. The dynamic cycle of ejection and sweep events is directly associated with vortical structures which extend at 45° from the near-bed flow field, and are characterised by a horseshoe geometry, although this may be distorted and fragmented (Grass, 1971; Head and Bandyopadhyay, 1981; Falco, 1991; Grass *et al.*, 1991; Smith *et al.*, 1991). The footprints of these vortices are represented in the near-bed flow field by elongated, alternate high and low velocity streaks. These streaks reflect the scale of the vortices, and appear to have a universal spacing, λ^+, of approximately 100 ($\lambda^+ = \lambda U_* / \nu \approx 100$, where λ is actual streak spacing, U_* is shear velocity and ν is viscosity; Grass, 1971; Defina, 1996). The transverse spacing between turbulent structures increases in a linear manner away from the bed (Defina, 1996), indicating that the longitudinal structures generating the streaks coalesce away from the boundary. Turbulent vortices entrain and transport fluid, momentum and sediment from near the bed into the outer flow. Within a vortex exist strong internal shear layers which can generate larger coherent turbulent flow structures downstream (Defina, 1996; Smith, 1996). The shedding of eddies from any shear layer enables the vortices to extract large amounts of energy from the mean flow, which is therefore retarded. Intense rotation in the vortices leads to the generation of secondary and subsidiary vortices, and the formation of vortex groups (Robinson, 1990; Smith, 1996). Accumulations of vortices enables the return flow from the sweep event to increase its magnitude and area of influence, which has important implications for sediment entrainment (e.g. patchy bedload movement, Drake *et al.*, 1988). Our understanding of vortex development and growth is complicated by their small scale and wide spectrum of morphologies.

Grass (1971, 1996) observed bursting over both smooth and rough (a layer of touching particles, with a thickness of one grain diameter (up to 12 mm)) boundaries. Over a rough bed, the low-speed streaks scale directly with the roughness element size, rather than the viscous length scale in the case of a smooth boundary. Low speed streaks have reduced coherence in the downstream direction over coarser beds. The structure of the turbulent boundary layer is critically influenced by relative roughness, the

= 0.2 for ripples, bedload sheets and low-relief bed waves is approximately 0.015, 0.02-0.03 and 0.025-0.16 Pa s^{-1}. Under lower flow depth conditions, the mean velocity is increased for a given discharge, enhancing velocity gradients over obstacles to the flow (e.g. coarse grains and bedforms) and increasing the magnitude of Kelvin-Helmholtz instabilities, which are a dominant source of turbulence. The mobile and fixed bedload sheet exhibit a very similar distribution of turbulence production, both with a value of 0.02 Pa s^{-1} at $y/d = 0.2$ ($y \approx 30$ mm) in Figure 5.17 and 5.16b, resulting from wakes generated by grain and form roughness. However, higher in the flow column (i.e. $y/d = 0.3$ and 0.4, $y \approx 40$ and 55 mm; Figure 5.17) turbulence production is reduced over the fixed bedload sheet compared with the mobile example due to the lack of sediment in transport (e.g. overpassing coarse clasts), which generates additional turbulence at greater heights above the mobile bed (Wiberg and Rubin, 1989).

Figure 5.16: *Spatially-averaged turbulence generation, T, plotted against normalised flow depth.*

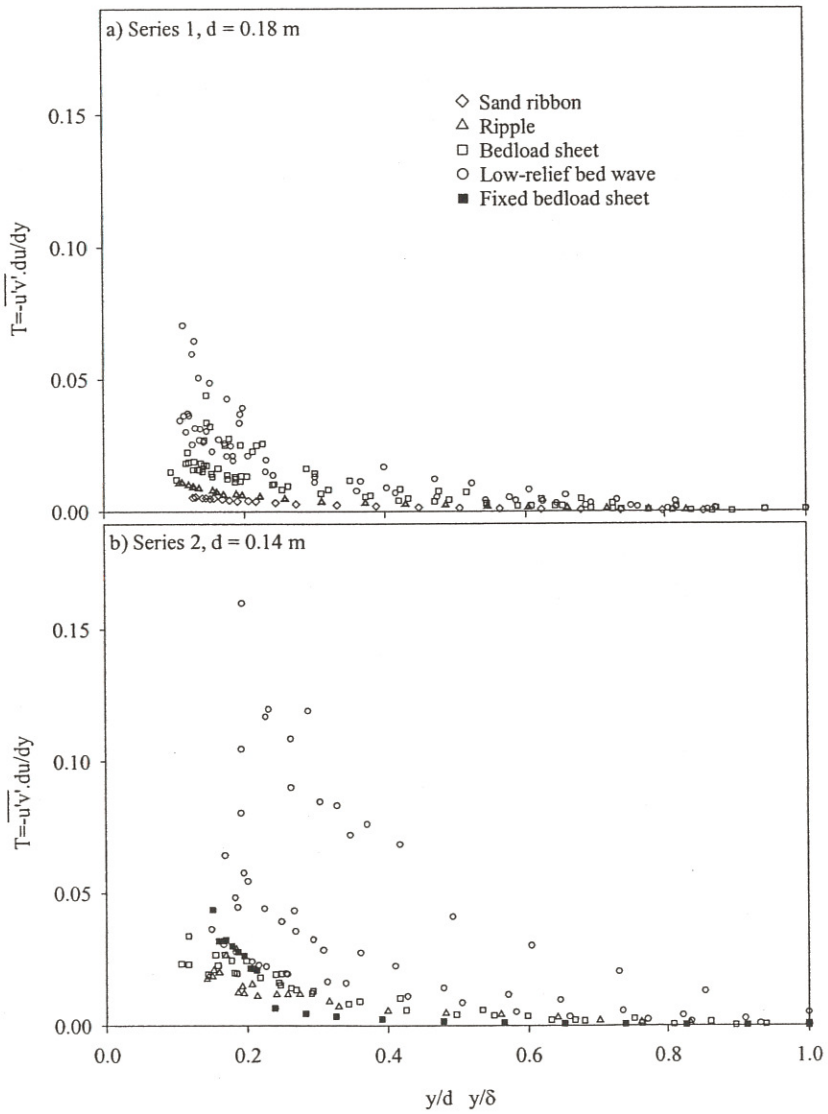

Above $y/d = 0.2$ it is impossible to distinguish between the amount of turbulence production at specific regions over an individual bedform (Figure 5.18), with the exception of the fixed low-relief bed wave (Figure 5.18iib). Turbulence measurements were possible closer to the sediment bed over the finer grained crest and upper stoss; consequently, values are available for these regions at lower y/d values than for measurements over the coarser tough area, thus hindering any comparison of turbulence generation when $y/d < 0.2$. Furthermore, below $y/d = 0.2$ values of turbulence intensity increase rapidly towards the bed, impeding accurate comparisons. Moreover, in the calculation of y/d for the mobile bed runs, a spatially-averaged flow depth was employed. In the fixed low-relief bed wave example (Figure 5.18iib, $0.2 < y/d < 0.5$), the greatest turbulence production is evident in the trough (~0.07 Pa s^{-1} at $y/d = 2$), reduced at separation and reattachment (~0.03 Pa s^{-1}), and the lowest over the crest (~0.01 Pa s^{-1}).

Turbulence production is greatest in the trough region due to the presence of coarse clasts capable of shedding eddies, and the dominant occurrence of a shear layer initiated from the upstream crest, which was previously identified from contour maps of the skewness of the velocity components and quadrant analysis (Figure 5.3 and 5.14). Since the magnitude of the wake is related to the size of the grain it is generated from (Nowell and Church, 1979), the tendency for the grain diameter to be greater in the trough will result in more turbulent energy being produced in this zone, although large grains may be temporarily be located elsewhere. The shear layer generated from the low-relief bed wave crest is damped in the streamwise direction due to topographic acceleration and turbulence dissipation. Furthermore, a boundary layer develops downstream of the reattachment point, causing turbulence production to be less effective over the stoss and crestal platform. The turbulence production measured by Carling *et al.*, (2000b) in the wake flow over sand dunes in the River Rhine, was one order of magnitude greater than over the stoss. Since the majority of turbulence is generated in the shear layer formed at the crest i.e. it is spatially specific, flow over bedforms cannot be considered to be identical to boundary layer flow (Nelson *et al.*, 1993).

5.3.6 Kinematic eddy viscosity

In more basic models of turbulence, eddy viscosity is an important quantity used to determine the distribution of Reynolds stress (Nezu and Rodi, 1986). It is apparent from Figure 5.19 that dimensionless eddy viscosity increases away from the bed, reaching a maximum at $y/d \sim 0.55$ ($\varepsilon/(U_* d) = 0.06$-$0.085$ and 0.06-0.075 when $d = 0.18$ and 0.14 m respectively) when the bed is mobile, and then diminishing towards the free surface which has a dampening effect on turbulent eddies. Large-scale turbulent structures are also damped (lower eddy viscosity) by the stretching of vortices resulting from topographic accelerations (Nelson *et al*, 1993). Indeed, Song and Graf (1994), observed

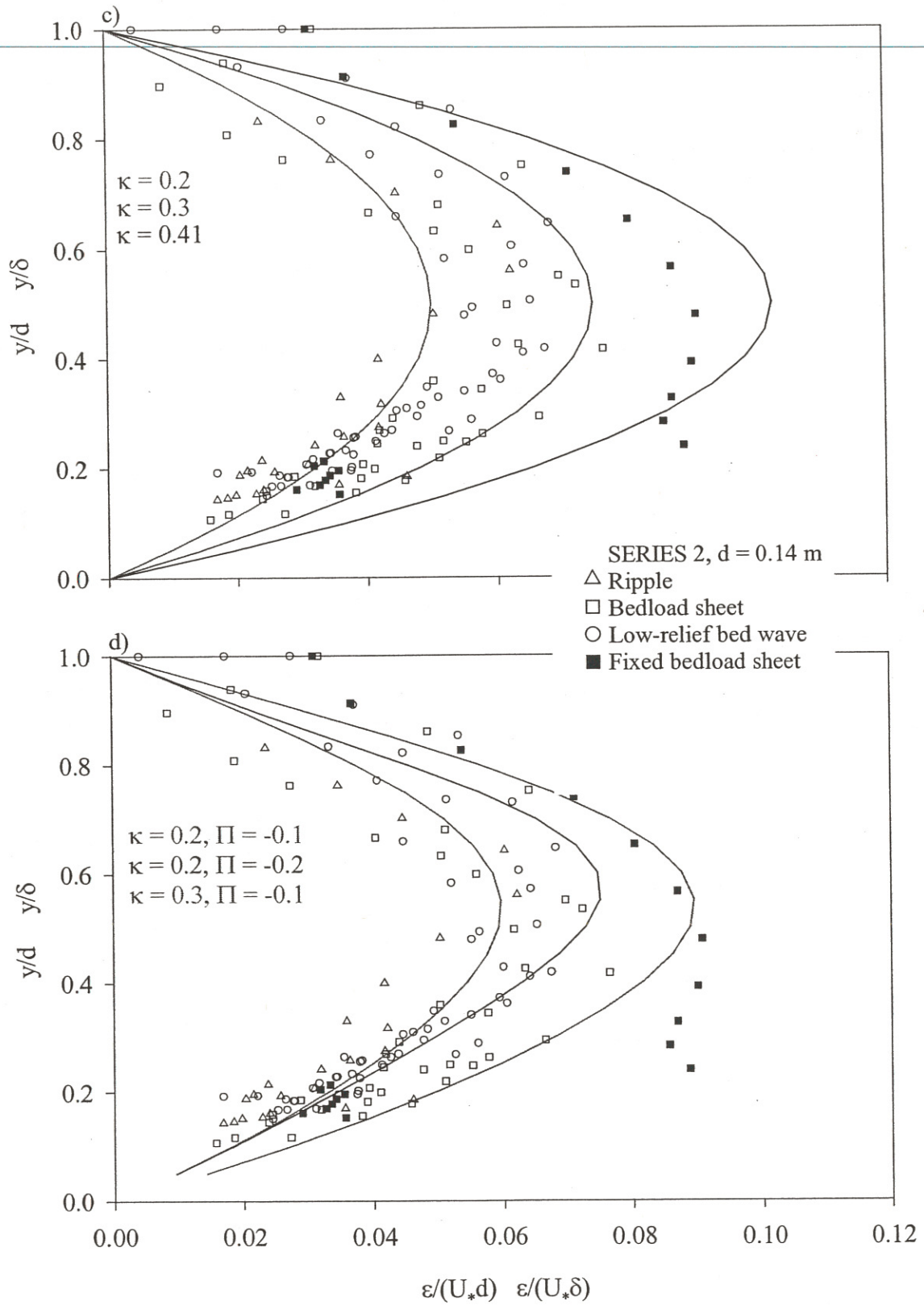

There is considerable scatter in the values of dimensionless eddy viscosity (Figure 5.19), which increases with distance from the boundary. Near the water surface it is difficult to accurately determine

It is difficult to accurately discern the changes in eddy viscosity between different locations over the bedforms due to experimental scatter, which results from the uncertainty in estimating the velocity gradient. However, in the case of the mobile and fixed low-relief bed waves, eddy viscosity is greatest over the crest (up to 0.14 and 0.085 for the fixed and mobile case respectively, as highlighted by the red symbols on Figure 5.21ib and iib (box B)). Furthermore, eddy viscosity at reattachment over the fixed bedload sheet (Figure 5.21iia, box A) falls below the spatial average. Carling *et al.* (2000b), observed eddy viscosity to be greatest in the turbulent wake over the trough of sand dunes in the River Rhine.

Figure 5.21: *Normalised eddy viscosity plotted against dimensionless flow depth for specific bedform regions. The areas highlighted in red are discussed in the text.*

i) Mobile bed conditions

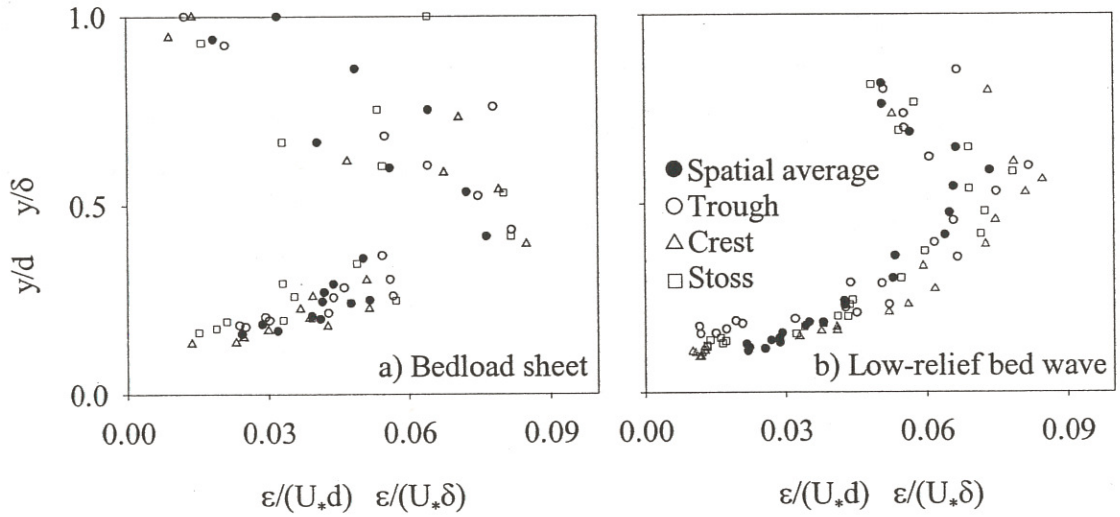

ii)

Fixed bed conditions

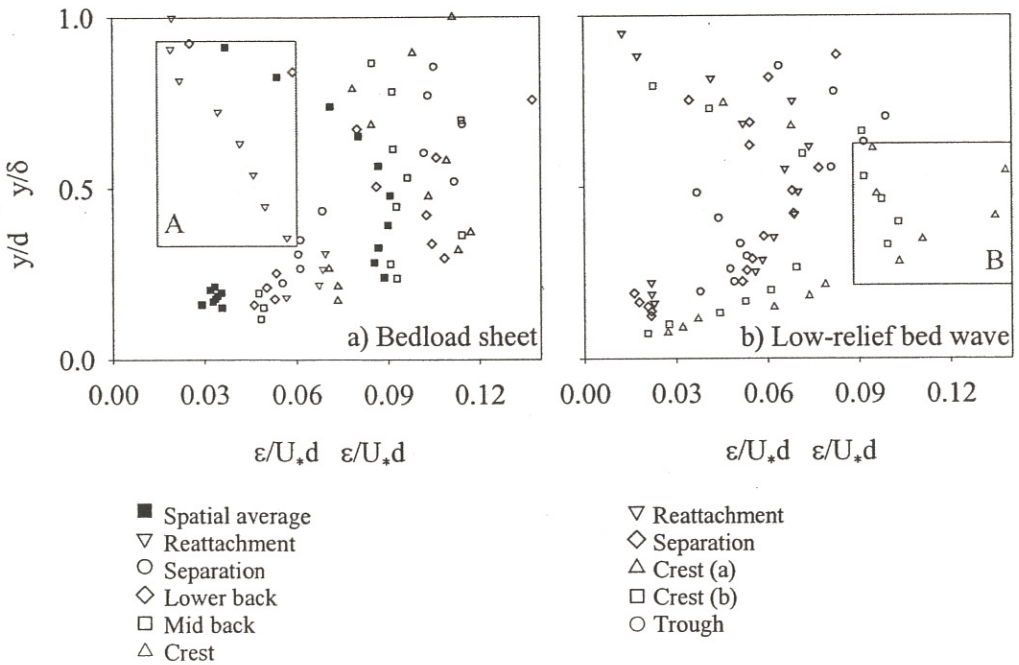

5.3.7 Mixing length

The vertical distribution of spatially-averaged mixing length, normalised by flow depth (Figure 5.23) exhibits an increase away from the boundary, reaching a maximum at approximately $y/d = 0.7$ (l/d = 0.095-0.13 and 0.08-0.11 at $d = 0.18$ and 0.14 m). Mixing lengths are reduced when the flow depth is lowered since topographic acceleration is enhanced (assuming bedform steepness remains similar), accentuating vortex stretching which therefore dampens turbulent eddies (Tritton, 1988; Nelson *et al.*, 1993). In the vicinity of the free surface, mixing length is reduced since the vertical dimension of the eddies, and therefore turbulence scale, is restricted. The mixing lengths derived from the present data are of similar magnitude to past studies at $y/d = 0.7$ e.g. Kironoto and Graf (1994) l/d = 0.1-0.2 over a rough bed; Nezu and Rodi (1986) l/d = 0.12-0.15 over a smooth bed. Nowell and Church (1979) conclude that a simple characteristic length scale for turbulence, such as mixing length, is not possible in depth-limited flows over roughness elements. They state that the length scale of turbulence varies with flow depth (as demonstrated in Figure 5.23) and the density of roughness elements. Song *et al.* (1994) noted no distinct difference in the distribution of mixing length between gravel beds with and without bedload movement. However, the fixed bedload sheet exhibits the greatest value for dimensionless mixing length (~ 0.14 at $y/d \sim 0.7$) in the present experiments. When sediment is transported within turbulent eddies, the inertia of the grains causes a decline in eddy scale and therefore mixing length (Best *et al.*, 1997; Bennett *et al.*, 1998). However, the impact of sediment movement on turbulence (e.g. attenuation or enhancement) is complex and subject to continuing debate (Vanoni, 1975; Best *et al.*, 1997). A ramp function is shown in Figure 5.23, and provides a simple approximation in the lower part of the flow. The ramp function fits the data best when a κ value of 0.2 is employed, much less than the value of 0.41 normally stated (Nezu and Nakagawa, 1993). Nelson *et al.*, (1993) observed that the mixing length in the boundary layer was smaller than predicted by the ramp function, indicating a reduced value for κ. They noted that the greatest divergence from the linear trend coincided with the largest topographic acceleration at the mid-point of the bedform stoss. Large-scale turbulent structures are damped due to vortex stretching which result from topographic acceleration. Furthermore, Nelson *et al.* (1993) concluded that the boundary layer developed over the back of the bedform reduces mixing length in the lower section of the overlying wake flow, i.e. a transitional zone between the boundary layer and wake region.

Experimental data scatter is considerable, and increases away from the bed, resulting from the difficulties in obtaining accurate velocity gradients and retardation effects (Cardoso *et al.*, 1989; Kironoto and Graf, 1994). Furthermore, mixing length is influenced in the intermediate region by the wake coefficient when a wake defect is present, which is Reynolds number dependent. The smoothed profiles (curve 1) of normalised mixing length, when plotted separately for each spatially-averaged run

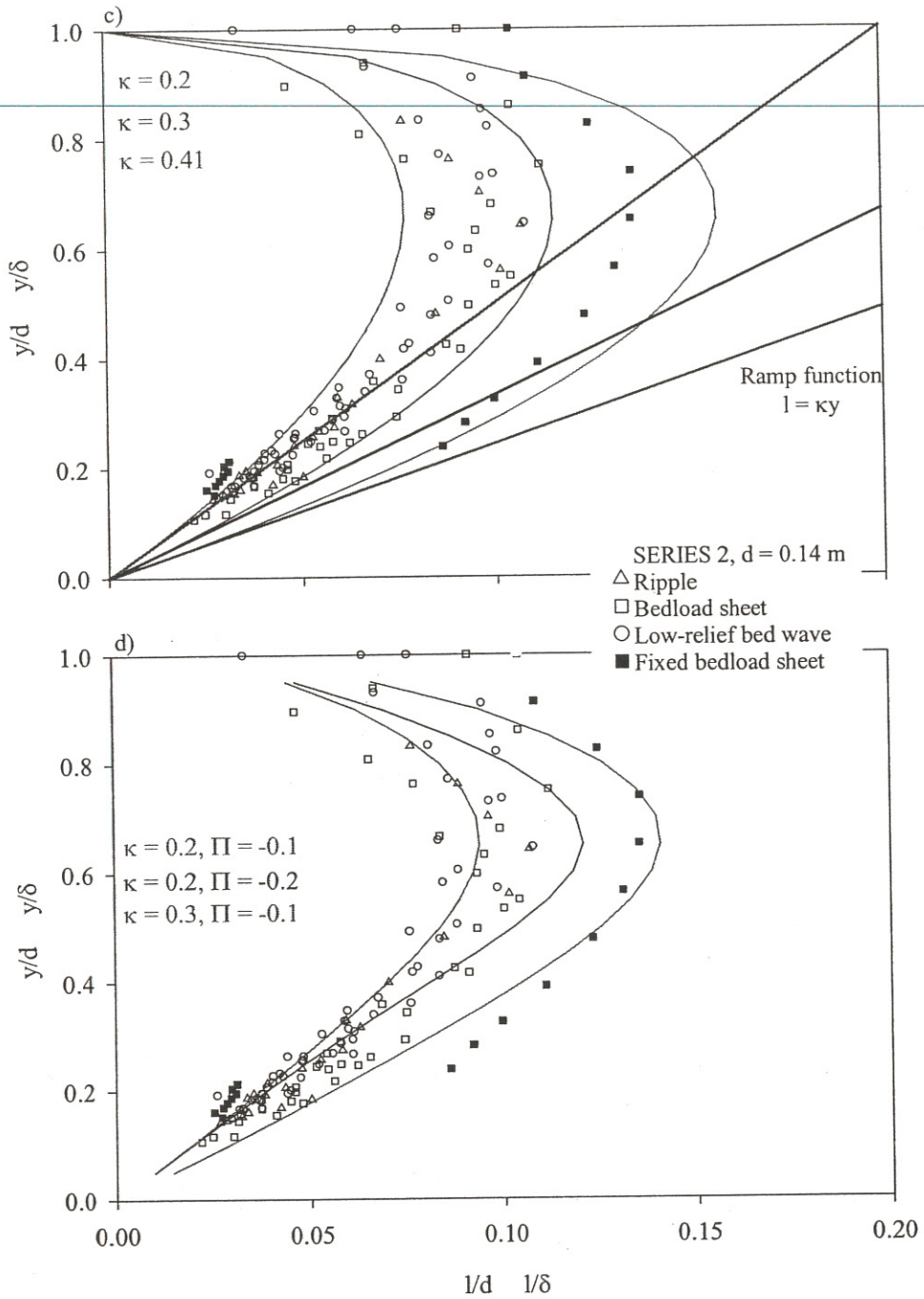

Mixing length is noted to be greatest over the crest of the fixed (up to l/d = 0.25) and mobile (up to l/d = 0.14) low-relief bed when $y/d < 0.8$ (red symbols on Figure 5.24ib and iib), as was also the case for eddy viscosity. In the case of the fixed bedload sheet, the values of mixing length in the separation and reattachment zone are demonstrated to be below the spatial average (red symbols in Figure 5.24iia), while the values recorded over the bedform stoss and crest were elevated above the spatial average. Carling *et al.* (2000b) noted the maximum mixing lengths occurred in the turbulent shear layer originating from the crest of sand dunes. Nelson *et al.* (1993) observed that the maximum value of mixing length increased over the lower bedform stoss side (i.e. –0.7 and –0.4 m downstream of the crest

5.3.8 Time series analysis in the frequency domain

Periodic variations in the downstream and vertical velocity time series at various locations in the flow over a fixed low-relief bed wave are identified in this section, and compared with predictions from theoretical and empirical equations. Furthermore, dominant statistically significant frequencies caused by eddy shedding and shear layer flapping will be distinguished and discussed.

Figure 5.26: *Locations of selected LDA velocity time series (red circles). White and black circles represent two and one component velocity measurements respectively.*

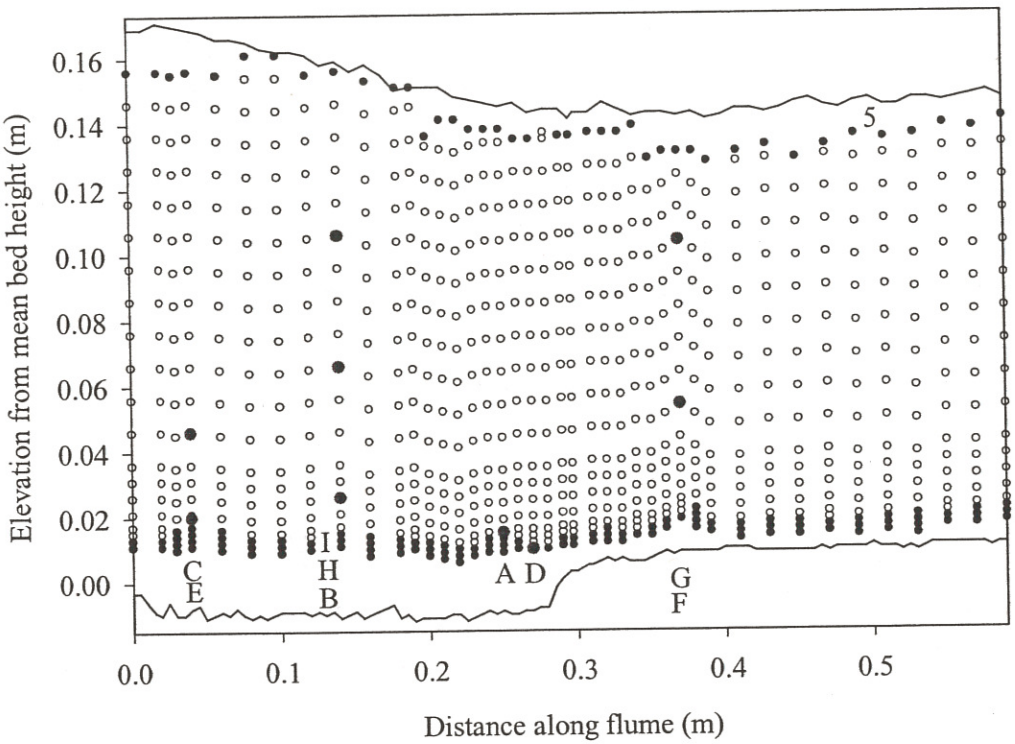

The resulting spectra taken at various locations over the fixed low-relief bed wave (Figure 5.26) are shown in Figure 5.27. Statistically significant peak frequencies which are dominant for both components of velocity are listed in Table 5.2. Simpson (1989) obtained frequency spectra downstream of a backward facing step, and observed two dominant frequencies in the separation zone. 1) A high frequency peak associated with the shedding of vortices from the separation point of the step and 2) a lower frequency is predominant outside the separation zone, which is attributed to flapping of the shear layer (Roden, 1998). Wake flapping is thought to result from the periodic transfer of the surrounding fluid into the separation region (Nezu and Nakagawa, 1993). Scale relations for the frequency of the vortex shedding (f_v) and wake flapping (f_w) have been proposed by Simpson (1989),

$$f_v \approx 0.8U_0 / x_r \tag{5.10}$$

$$f_w < 0.1U_0 / x_r \tag{5.11}$$

***Table 5.3**: Predicted frequencies (Hz) for the recurrence of turbulence structures over a fixed low-relief bed wave, using a depth averaged velocity (U) of 0.87 m/s, flow depth (d) of 0.151 m and bedform height (h) of 0.02 m.*

Predictive equation	Predicted frequencies (Hz)
Strouhal Law, Levi (1983b), depth-scale turbulent structures.	0.9
Itakura and Kishi (1980)	6.1
Simpson (1989):	
Vortex shedding	5.8-17.4
Wake flapping	0.7-2.2

***Figure 5.27:** Spectra of the time averaged a) downstream and b) vertical velocity at various locations over a low-relief bed wave. The 99.9 % significance level is shown.*

a)

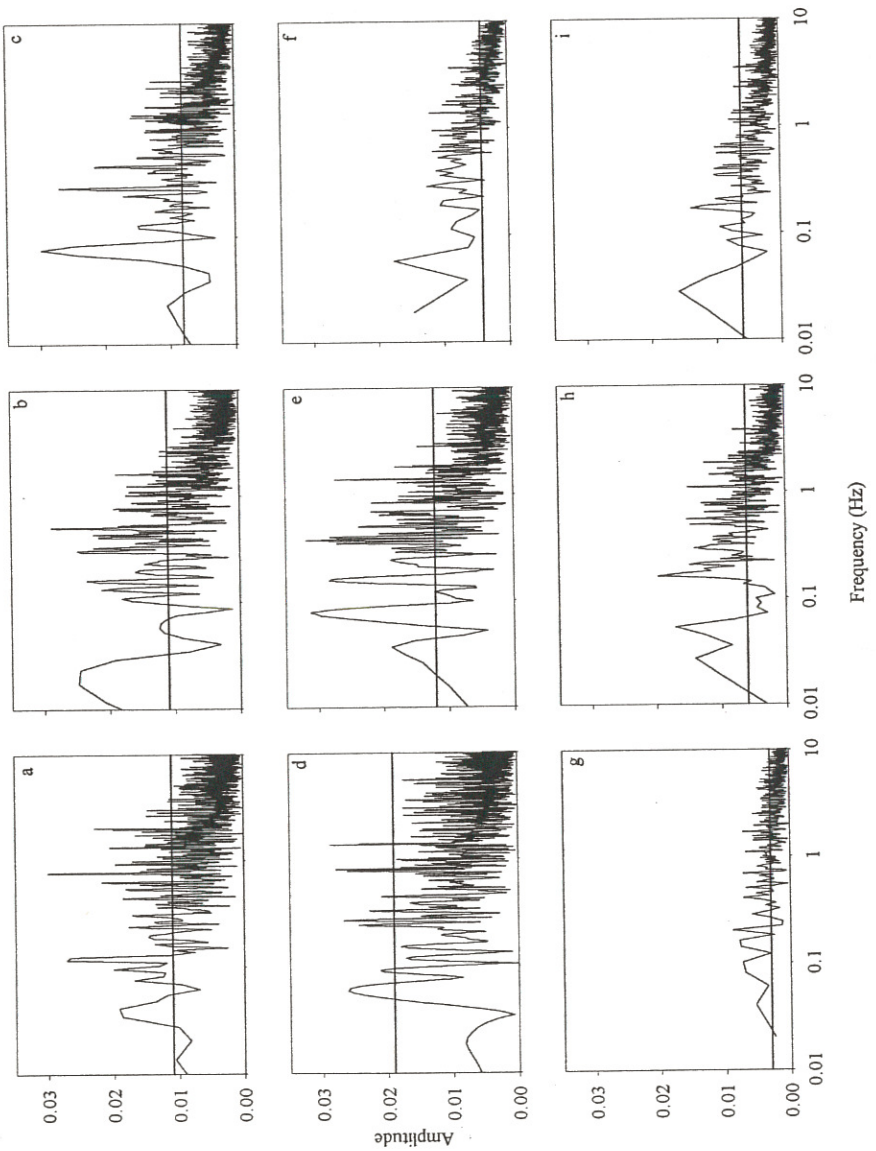

The dominant frequencies associated with turbulent structures scaled on the entire flow depth can be predicted by the Strouhal law (Levi, 1983b, 1991) for both microturbulent and macroturbulent frequencies, f_s,

$$f_s = U_s / 2\pi\delta \tag{5.12}$$

where U_s is the freestream velocity and δ is the boundary layer thickness (i.e. flow depth, d, where there is no velocity defect). Under comparable conditions, Jackson (1976) noted that the frequency of occurrence of boils was increased over a dune bed configuration compared with a flat bed. The frequency of turbulence structures produced by dunes, f_d, is predicted by the experimental and empirical equation of Itakura and Kishi (1980),

$$f_d = 0.14U / h \tag{5.13}$$

where U is the mean velocity over the bedform (dune), and h is bedform height. The predicted dominant frequency from the Strouhal law (0.9 Hz, Table 5.3) falls within the range of experimental values obtained (0.03-2.02 Hz, Table 5.2), whereas the empirical relation of Itakura and Kishi (1980) is at least 300 % greater (6.1 Hz, Table 5.3) than the statistically significant frequencies obtained from the frequency spectrums. The Strouhal law value (0.9 Hz) is within the range of frequencies associated with wake flapping by Simpson's (1989) relation (0.7-2.2 Hz), whereas the value predicted by the equation of Itakura and Kishi (6.1 Hz) falls within the range of frequencies linked to vortex shedding (5.8-17.4 Hz). Furthermore, Kostaschuk (2000) found that the equation of Itakura and Kishi (1980), despite being formulated specifically for dunes, did not agree as well as the Strouhal Law with his measurements taken over dunes in the Fraser River system, Canada. The greater frequencies predicted by the relation of Itakura and Kishi (1980) is attributed by Kostaschuk (2000) to the counting of shedded vortices in addition to eddies at the point of reattachment (associated with wake flapping) during flow visualisation experiments. However, at-a-point measurements are influenced by a variety of eddy sizes, vortex coalescence and wake effects, which tend to diminish the average eddy frequency. Clifford (1996) found a positive relationship between mean velocity and the period of turbulent structures, whereas the Strouhal law implies an inverse relationship exists (Equation 5.12). The Strouhal law is also problematic where eddy frequency varies with Reynolds number and particle size. Furthermore, one obstacle may shed eddies with a range of sizes, and therefore periods. At a particular point, the magnitude and frequency of eddies may be influenced by vortex pairing, shearing and coalescence. Indeed, Nowell and Church (1979) indicate that if a range of particles are present, the shedding of eddies and subsequent interactions will generate a complex distribution of frequencies. Therefore, despite successful applications (e.g. Clifford *et al*, 1992; Robert *et al.*, 1993), the utility of the Strouhal law is subject to debate. In a depth-limited flow over coarse grains, Robert *et al.* (1993) observed dominant periods of 1-2 s, which decreased away from the bed.

the mechanisms responsible are unclear. The relative motion between the sediment (extracts momentum from the flow, reducing near bed velocity) and fluid phases generally causes the roughness length of the mobile beds to be greater than that of the fixed beds (Smith and McLean, 1977; Wiberg and Rubin, 1989; Best *et al.,* 1997; Bennett *et al.*, 1998), resulting in increased flow resistance (Song *et al.*, 1994). However, Heathershaw and Langhorne (1988), noted that during intense bedload transport over the sea floor, the roughness length fell, and was insensitive to lower rates of transport. Mobile sediment can cause the roughness of the bed to increase by 1-3 orders of magnitude compared with the roughness of a stationary bed (Wiberg and Rubin, 1989). The thickness of the bedload layer is thought to be directly proportional to the magnitude of the roughness. Resistance to the flow results from the generation of wakes from the sediment grains, which are accelerated by the flow as both bedload and suspended load (Carbonneau and Bergeron, 2000). The magnitude of the roughness depends on the concentration of bedload and the vertical height over which a grain is accelerated before obtaining the same velocity as the surrounding fluid, which is approximately equal to the height of the bedload layer. In the experiments of Carbonneau and Bergeron (2000), bedload transport was shown to both increase and decrease flow velocity over a rough bed. Turbulence modulation is influenced by the bed roughness, eddy shedding, grain inertial effects and interactions between grains, coherent flow structures and flow boundaries (Best *et al.*, 1997).

The non-permeable nature of the fixed bed causes reduced drag since there is no flow and dilation within the sediment bed (Zippe and Graf, 1983). Turbulent motions are not confined to the region above the porous bed, but instead extend into the particle interstices. Therefore, Mendoza and Zhou (1992) note that over a porous bed, the no-slip boundary condition is no longer strictly applicable, and an additional Reynolds stress exists. The decrease in drag due to the non-permeable bed further increases the difference in flow resistance between the fixed and mobile beds. Over rough permeable surfaces, the coefficient of resistance is influenced by Reynolds number (Mendoza and Zhou, 1992) and the relative thickness of the permeable layer. However, no difference between turbulent fluctuations over a permeable and non-permeable bed were distinguishable in the experiments of Zippe and Graf (1983).

The constantly changing bed morphology in the mobile bed runs adds to the complexity of the situation. When a mobile bed is fixed, it is not physically possible to maintain exactly the same hydraulic conditions. In the present experiments, when the bed was fixed the slope of the flume and the water discharge were maintained, while the water surface slope and flow depth altered marginally (Table 4.1). The reasons for the difference in water depth are explained in Section 4.3.1. The lower flow depths associated with the fixed experiments will increase their relative roughness.

transition in bed roughness, being elevated (i.e. overshooting) and reduced (i.e. undershooting) immediately downstream of a smooth to rough and rough to smooth transition respectively (Nezu *et al.*, 1993). Downstream of a smooth to rough discontinuity, Nezu *et al.* (1993) observed that the contribution of quadrant 2 events to Reynolds stress fell and the ratio of quadrant 4 to quadrant 2 events increased. The same trends are illustrated in the zone of flow separation/retardance immediately downstream of the change in roughness from smooth (crest) to rough (trough) over a bedload sheet (Figure 5.13) low-relief bed wave (Figure 5.15).

The structure of the inner layer over a smooth and rough wall differ, and is dependent in the latter case on the roughness geometry. Over a smooth to rough discontinuity, the turbulence intensity within the internal boundary layer drives its development (flow is fully adjusted over a distance of less than 20 boundary layer thicknesses). However, downstream of a rough to smooth transition, the growth of the internal layer is relatively slow compared with a smooth to rough discontinuity since it is influenced by both the inner and outer layers, and the response of the turbulence parameters are less marked. In the present experiments, the variations in bed roughness and elevation occur frequently, hindering the full development of an internal boundary layer before another is initiated at a downstream transition in the wall conditions. Consequently, the multiple boundary layers interact (Livesey, 1995), resulting in a complex turbulent flow field.

5.4.3 Influence of turbulence on sediment transport

The movement of sediment is discontinuous (Raudkivi, 1966), with the largest grains being moved only sporadically at bed shear stresses greater than 7 Pa. Bedload transport is very sensitive to surface structures, grain size, relative roughness and small changes in flow conditions (Hassan and Church, 2000; Shvidchenko and Pender, 2000). The mean flow and sediment transport can be linked in steady, uniform flow, but accuracy decreases when applied to non-uniform conditions e.g. over bedforms (McLean *et al.*, 1994; Nelson *et al.*, 1995). The reduction in the correlation coefficient near the bed ($y/d < 0.3$; Figure 5.10), resulting from the interaction between the internal boundary layer and the overlying turbulent wake region, confirms the poor correlation between sediment transport and the local boundary shear stress (McLean *et al.*, 1996). Furthermore, greater sediment transport can be associated with increased turbulence intensity when bed shear stress remains constant (Nelson *et al.*, 1993). Higher turbulence intensity does not necessarily increase Reynolds stress since there is a poor correlation between the horizontal and vertical velocity fluctuations. The transport of sediment downstream can occur as a result of turbulence (e.g. quadrant 1 and 4 events) even where mean velocity, or bed shear stress, is zero (Thorne *et al.*, 1989; McLean *et al.*, 1996). The majority of bedload is moved by quadrant 4 events, although quadrant 1 events of comparable magnitude and duration move an equal quantity of sediment, but are less frequent (Thorne *et al.*, 1989; Nelson *et al.*, 1995). Both Drake *et al.*

Figure 5.28: *Comparison of the predicted (MPM) and measured values of bedload transport rate. The best agreement is for the low-relief bed waves highlighted in Box A.*

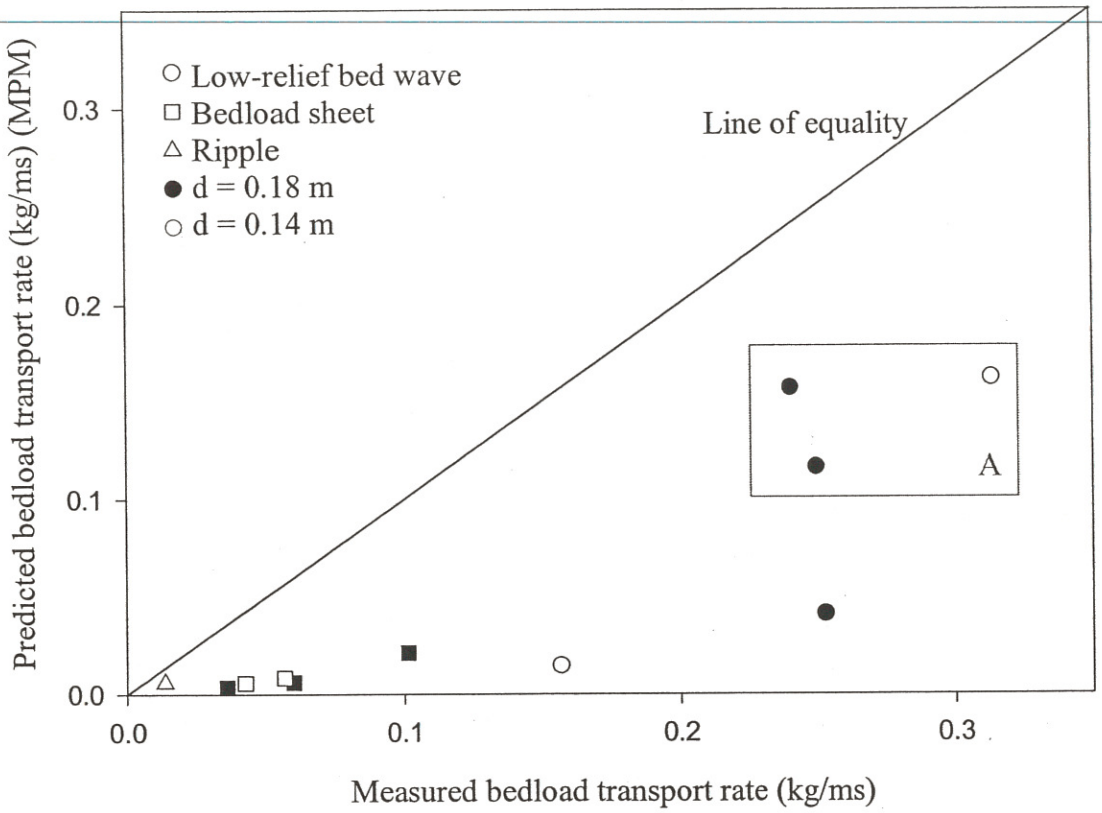

In all experimental runs the measured bedload transport rates are under-predicted (typically by 90-80 %) by the formula of MPM. The best percentage agreement (~ 50 %) is found for the low-relief bed waves highlighted in box A in Figure 5.28. Vertical and horizontal sorting of sediment, and the bimodal nature of the present experimental mixture, may partly contribute to the disagreement between measured and predicted bedload transport rates. In a sediment mixture, under conditions of selective entrainment a range of critical thresholds exist (Robert, 1993) due to the effects of relative protrusion, grain exposure, imbrication, clustering, and pivot and friction angle (Komar, 1987a, b). The bedload transport measurements made in the flume may be dependent on the width-depth ratio, flume system (feed or recirculating), and the number of bedforms included in each sample.

McLean *et al.* (1994) attributed the poor agreement of measured and predicted transport rates over a fixed dune to the occurrence of flow separation, and the inaccuracy in estimates of shear stress due to the thin boundary layer at reattachment. However, Nelson *et al.* (1995) stress that variations in the structure of turbulence not registered by bed shear stress should be expected in any developing boundary layer, even if flow separation is absent or intermittent e.g. the roughness transitions over bedload sheets (Antonia and Luxton, 1971, 1972), low-angle dunes (Best and Kostaschuk, in press). The higher than predicted rates of sediment transport downstream of reattachment over a fixed dune in

of Nelson *et al.* (1993) and Bennett and Best (1995, 1996)) reduces the contrast between the spatially-averaged Reynolds stress and its value at reattachment downstream of the crest. The relatively low elevation of the bedload sheets and low-relief bed waves (~10 mm) also helps explain the reduced variation in Reynolds stress from the spatial average compared with larger dune bedforms (40 mm).

***Table 5.4**: Variations in flow parameters between different regions over the bedforms. Modified from Bennett and Best (1996).*

Flow parameter	**Bedload sheets**	**Low-relief bed waves**	**Ripples[1]**	**Dunes[2]**
Uniformity	Non-uniform	Strongly non-uniform	Weakly uniform	Strongly non-uniform
Shear layer: Attitude	Parallel to stoss	Parallel to stoss	Parallel to bed	Parallel to stoss
Vertical extent	Extends to $0.5d$	Extends to $0.7d$	Limited to $0.2d$	Extends to water surface
Quadrant 2 events	Moderate vertical restriction and magnitude	Unrestricted vertically, high magnitude	Vertically restricted, low magnitude	Unrestricted vertically, very high magnitude
Velocity gradient	Moderate	Large	Small	Very large
Quadrant 4 events from outer region	Yes	Not detected in Figure 5.14	No	Yes
Reattachment: Quadrant 4 events	High percentage occurrence	High percentage occurrence	Infrequent, low magnitude	Frequent, high magnitude
Reynolds stress	$\sim\overline{\tau}_{R0}$	2-3 $\overline{\tau}_{R0}$	2-3 $\overline{\tau}_0$	6-9 $\overline{\tau}_0$
Turbulence intensity	Lowest over crest	Greatest in shear layer over trough	Greatest in shear layer over trough	Greatest in shear layer over trough
Correlation coefficient	Reduced over stoss, average over the crest and elevated in the deceleration zone	Spatial average is reduced from that expected in a uniform boundary layer		Over the stoss, increases and decreases in the developing boundary layer and wake respectively, towards a value similar to that expected in a uniform boundary layer at the crest
Turbulence production	Not possible to distinguish spatial variations	Greatest in shear layer over trough, lowest over crest		Greatest in shear layer
Mixing length and kinematic eddy viscosity	Below the spatial average at reattachment	Greatest over crest		Greatest in shear layer

[1] Wiberg and Nelson (1992); Bennett and Best (1996).

[2] Nelson *et al.* (1993); McLean *et al.* (1994); Bennett and Best (1995); Carling *et al.* (2000b).

Table 5.5: *Contrasts and similarities between dunes, bedload sheets and low-relief bed waves.*

Similarities	Contrasts
All experimental data plots in the dune stability field in Southard and Boguchwal's figures 2N, 2O and 2P (1990), which do not consider bedload sheets or low-relief bed waves. In Figure 3.17 (Best, 1996), the present data plots in the dune and bedload sheet regions. Most of the data for constructing stability diagrams is collected over fine, uniform sediment. The low-angle dunes recorded by Kostaschuk and Villard (1996) plotted in the stability fields for upper-stage plane beds or antidunes, highlighting the need to consider a range of factors when classifying bedforms.	Ashley (1990) defines dunes as having a wavelength of greater than 0.6 m, and a height over 0.075 m. The height of the bedload sheets and low-relief bed waves scale with the coarsest particles in transport (D_{90}), whereas dunes exhibit no scaling with grain size (Carling, 1999). The height of bedforms tends to decrease as the sediment becomes more poorly sorted and the D_{50} increases (Snishchenko *et al.*, 1989).
Permanent flow separation is not a prerequisite for dunes. Intermittent or no flow separation can occur over low-angled dunes (Best and Kostaschuk, in press). Shear layers are generated from the crest of dunes, bedload sheets and low-relief bed waves, as well as from coarse, protruding grains.	A poorly sorted sediment mixture is required for the formation of bedload sheets and low-relief bedwaves, which allows grain sorting by selective entrainment. Iseya and Ikeda (1987) and Dietrich *et al.* (1989) observed no bedload sheets when the sediment mixture contained gravel and no sand. Dunes can form in uniform sediment.
Low-relief bed waves and dunes scale with flow depth (Allen, 1984).	The velocity gradient is greater over dunes, increasing the magnitude, frequency and vertical extent of turbulence.
Coarse armour layers occur in the troughs of bedload sheets and low-relief bed waves. Immobile large grains are also present in the troughs of dunes when sediment transport rates are low.	The ratio of length to flow depth is approximately 5 for dunes (Allen, 1982), but $\leq$ 4 for bedload sheets and $\geq$ 18 for low-relief bed waves. The steepness (height/length) of equilibrium dunes is much greater (0.08; Carling, 1999) compared with bedload sheets (0.017) and low-relief bed waves (0.004).

5.4.5 Bedform development

5.4.5.1 Sand ribbons

At the lowest discharges, the sand fractions were selectively entrained in the present experiments, forming sand ribbons, which are narrow, elongated, flow-parallel features previously recorded by Iseya and Ikeda (1987), Ferguson *et al.* (1989) and Tsujimoto (1991, 1999). The development of these longitudinal forms is closely coupled to the development of secondary currents (Parker, 1992; Nezu and Nakagawa, 1993; Tsujimoto and Kitamura, 1996), which promote lateral bedload transport and sorting, and are facilitated by transverse variations in bed shear stress resulting from the alternate coarse and fine sediment stripes. However, secondary currents can develop in a sediment-free channel when the width-depth ratio is below five (Nezu and Nakagawa, 1985). Before conducting the present experiments, measurements of the lateral and downstream velocity components were taken using an ADV when the flume was filled with water and no sediment. The maximum lateral velocities were observed to be approximately 5 % of the downstream values, which occurred near the sidewall away from the bed. Downstream velocities and bed shear stresses have been found to be higher over the

***Table 5.6**: Summary of the changing morphology, sediment transport, flow and turbulent structure between characteristic bed states in the present experiments. Arrows indicate the direction of increase for each parameter.*

Bed state	Morphology			
	Height	Length	Topographic forcing	Sediment transport: quantity and size
Flat bed/ sand ribbon	↓		↓	↓
Ripple		↓		
Bedload sheet				
Low-relief bed wave				

Bed state	Turbulent flow structure			
	Spatially-averaged (y/d < 0.3)			
	Turbulence production	Normalised turbulence intensity	Normalised Reynolds stress	Spatial variability (horizontal and vertical)
Flat bed/ sand ribbon	↓	↓	↓	↓
Ripple				
Bedload sheet				
Low-relief bed wave				

Bed state	Turbulent flow structure			
	Velocity gradient	Flow uniformity	Water surface interactions	Vertical extent and magnitude of quadrant 2 events
Flat bed/ sand ribbon	↓	↑	↓	↓
Ripple				
Bedload sheet				
Low-relief bed wave				

5.4.5.3 Bedload sheets

With increasing flow strength, ripples develop into bedload sheets ($\tau_{R0} > 3$), which are morphologically distinguished by their greater height (7-12 mm) compared with ripples (3-5 mm). Bedload sheets also transport a greater quantity and calibre of sediment, which increases grain roughness, turbulence production, turbulence intensity and Reynolds stress (Figure 5.29 and Table 5.6). The total sediment transport rate has been demonstrated to be directly related to the increase in bedform height using a modified version of Simons *et al.'s* (1965) formula (Equation 3.5, Figure 3.16), which was not originally derived for bedload sheets. The height of an individual ripple may become abnormally high (i.e. rogue ripple, Leeder, 1983) due to bedform amalgamations facilitated by the range of ripple migration rates (4-34 mm/s; Raudkivi and Witte, 1990; Ditchfield and Best, 1992; Coleman and Melville, 1994). Other suggestions for the production of a rogue ripple include small scale fluctuations in sediment transport e.g. the three-dimensionality of the ripple may cause transient increases in local bed shear stress. Furthermore, the shear layer originating at the ripple crest may 'flap' (Simpson, 1989), causing the point of reattachment, associated with high instantaneous Reynolds stresses, to vary and encompass a greater area, resulting in increased sediment erosion and transport. The greater height of the rogue ripple is associated with critical changes in the turbulent flow structure (e.g. magnitude of the velocity gradient, degree of flow separation/deceleration, intensity of shearing and magnitude and frequency of eddy shedding; McLean *et al.,* 1994), the influence of which propagates downstream. The turbulence intensity over bedload sheets is greater than that over the smaller ripple forms (Figure 5.29), which causes Reynolds stress, and therefore sediment entrainment, to increase at reattachment (Muller and Gyr, 1996). The greater erosion of sediment at the reattachment point is associated with increased deposition at the downstream bedform crest. The magnitude and frequency of quadrant 2 events caused by eddy shedding increases with the transition to bedload sheets. Quadrant 2 events originating from ripples are limited to the lowest 20 percent of the flow depth (Bennett and Best, 1996), whereas over bedload sheets quadrant 2 events are able to penetrate further into the outer flow, and are replaced by quadrant 4 events originating higher in the profile in order to maintain continuity.

5.4.5.4 Low-relief bed waves

Further increases in the amount and size of mobile sediment (due to increasing bed shear stress) are accommodated by the evolution of low-relief bed waves, which are associated with a substantial increase in wavelength (i.e. bedload sheets are up to 1 m long while low-relief bed waves range from 2.3-4.9 m long, Table 5.6; Wilcock and McArdell, 1993; Coleman and Melville, 1994). The low-relief bed waves developed in Series 1 (d = 0.18 m) are greater in height (13-15 mm) compared with the bedload sheets (7-12 mm), and therefore have reduced migration rates (up to 14 and 27 mm/s